UNIVERSITY OF CALIFORNIA, SAN DIEGO

The Detection of Electrical Anisotropy in 35 Ma Pacific Lithosphere: Results from a Marine Controlled-Source Electromagnetic Survey and Implications for Hydration of the Upper Mantle

A dissertation submitted in partial satisfaction of the requirements

for the degree Doctor of Philosophy in Earth Sciences

by

James Philip Behrens

Committee in charge:

Steven Constable, Chair
Donna Blackman
Steven Cande
Charles Cox
John Goodkind

2005

The dissertation of James Philip Behrens is approved, and it is acceptable in quality and form for publication on microfilm:

John M. Fordham

Charles S. Cox

Steven C. Cande

Chair

University of California, San Diego

2005

For my parents Martha and Jim, and my sisters Julie and Michelle

Thirty spokes share the wheel's hub,

but it is the hole in the center that makes it useful.

-Tao Te Ching, Chapter 11

TABLE OF CONTENTS

LIST OF SYMBOLS

σ	electrical conductivity, S/m $(=1/\rho)$
ρ	electrical resistivity, Ωm $(=1/\sigma)$
E, **J**	vector electric and current density fields
B, **H**	vector magnetic flux density and magnetic fields
μ	magnetic permeability
f, ω	frequency, Hz and angular frequency, rad/s
λ	wavelength; unrelated use as ridge regression bias in section 2.5.1
k, β	complex wave number and components
E_ρ, E_ϕ	radial and azimuthal components of the electric field
$\hat{E}$	electric field component in the horizontal wavenumber domain
ϕ	azimuth from transmitter axis to the line joining the transmitter and receiver
φ	phase of electric field
$\|\|$	indicates component of **E**, $\boldsymbol{\sigma}$, or $\boldsymbol{\rho}$ parallel to anisotropic strike (i.e. $\rho_\|$)
$\perp$	indicates component of **E**, $\boldsymbol{\sigma}$, or $\boldsymbol{\rho}$ perpendicular to anisotropic strike (i.e. $\rho_\perp$)
f_a	anisotropic ratio $\left(f_a = \rho_\|/\rho_\perp = \sigma_\perp/\sigma_\|\right)$
d	data vector
p	vector of variable model parameters
A	Jacobian matrix
P_{MAX}	large axis of horizontal electric field polarization ellipse
P_{MIN}	small axis of horizontal electric field polarization ellipse
α_N	orientation of P_{MAX} relative to geodetic north
R_1, R_2	norms of first- and second-derivative model "roughness"
$\varnothing$	porosity

LIST OF FIGURES

LIST OF TABLES

ACKNOWLEDGEMENTS

First and foremost, I would like to thank my family. They have been a source of strength and unconditional support all these years. Mom stocked my room with encyclopedias and science books from the beginning and encouraged my musical pursuits; Dad taught me an appreciation for the natural world and a sense of logical skepticism; my sisters have done their best to keep me humble. Grandparents, aunts, uncles, cousins, and neighbors have all been important people in my life; every kid should be so lucky.

I am grateful to my advisor, Steve Constable, for allowing me the opportunity to work with him at the vanguard of marine electromagnetic geophysics. He's taught me the ways of EM while funding my research, introducing me to a network of colleagues, and providing me with opportunities to consult on industry projects. I showed up at Scripps looking to travel the world collecting EM data, and thanks to Steve, that wish came true. Steve and Cathy also kindly invited me to their home for many tasty dinners (and bottles of wine). I would also like to thank the other members of my committee: Donna Blackman, Steve Cande, Chip Cox, and John Goodkind, all of whom have contributed to my knowledge and understanding of the subject matter presented in this dissertation.

Kerry Key is a good friend, travel companion, and colleague; the knowledge I gained during our technical discussions and field work together has been invaluable. Thank you, Kerry, for taking a green Midwesterner under your wing. My office mate Adrian Borsa has been like an older brother; a friend and confidant through many adventures.

I would like to thank Mark Everett for the use of his anisotropy code, his hospitality during my visit to TAMU, his encouraging demeanor, and many stimulating discussions regarding both electromagnetic geophysics and 70s rock. Lucy MacGregor provided the transmitter for APPLE and took the time to explain many of the finer points of CSEM. Chet

Weiss made me feel welcome in Albuquerque, and I left with a much greater conceptual understanding of EM field modeling. I have benefited from several conversations with Graham Heinson during this research, as well.

An ongoing partnership with AOA Geophysics added adventure and profit to my graduate school life, and helped me develop and build confidence in my abilities. I've been fortunate to spend time at sea (and in port) with Arnie Orange, Lisl and Rhodri Lewis, Cristiano Signorini, Adam Agundes, Hiatt Sheller, Ransom Reddig, and Tom Garcia, and had the good fortune to work with Len Srnka of ExxonMobil. Xinyou Lu of ExxonMobil found some of the bugs in SFT6. Leon Thomsen made sure my internship at BP was educational and productive.

I have met many good people during my time at Scripps: my Keller-mates Bridget Smith, Christine Reif, and Scott Nooner; Dave McMillan, Vera Schulte-Pelkum, Dave Drazen, Steph Mumma, Liz Gil, Carolyn Keen, Karen Weitemeyer, Drew Lucas, Fiona Sutherland, Courtney Schatzman, Jacques Lemire, Allan Sauter, Catherine Johnson, Glenn Ierley, Alison Shaw, Bonnie Becker, Yuguo Li, Garth Engelhorn, Patricia Cheng, Chris Armerding, and Lucrezia Terzi, to name just a few. The arrival of Thorsten Becker was a pleasant surprise – the T-Geld abides. I spent many weekends enjoying a musical collaboration with Steve Branson. Life at Casa Azul has been idyllic thanks to my fellow Azulians: Justin Kulongoski, Susan Quintal, Liz Zambricki, Pete Podein, Scott Rapoport, and Christina Wedell.

The captain and crew of the R/V Thompson, cruise TN-121, worked hard to help us collect this CSEM data set. With me in the science party: Steve Constable, Kerry Key, Lisl Lewis, Lucy MacGregor, Monika Korte, Neville Barker, Dhananjai Pandey, and Adrian Costar. Jennifer Rust, Gary Austin, and Jacques Lemire provided engineering support.

Finally, I would like to express gratitude to George Jiracek, Ian Shipsey, Robert Nowack, and Laura Pyrak-Nolte for helping me find this path, and to Wayne Miller and Joe Bosoty for teaching me the language of music.

Three years of funding for this project was provided by the NSF. I received a year of funding from the Seafloor Electromagnetic Methods Consortium, and support from BP during the writing of this dissertation.

Section 2.4.2, in part, contains material from the manuscript "The detection of an anisotropic layer in oceanic lithosphere by the seafloor controlled-source electromagnetic method" by Everett, M. E., Constable, S. C., and Behrens, J., prepared for submission to Geophysical Journal International. The dissertation author was a co-author of this manuscript.

VITA

1977	Born March 31 in Cleveland, Ohio
1997-1999	Teaching Assistant, Astronomy Labs, Physics Department, Purdue University
1998	Research Assistant, Rock Physics Lab, Purdue University
1998	Summer of Applied Geophysical Experience
1999	B.S., Honors Applied Physics; Purdue University
1999	Intern, Wireline and Testing, Schlumberger Oilfield Services
1999-2005	Graduate Student Researcher, University of California, San Diego
2001-2004	Consulting Geophysicist, AOA Geophysics / AOA Geomarine Operations
2004	Intern, Exploration and Production Technology, BP America
2005	Ph.D., Earth Sciences; Institute of Geophysics and Planetary Physics, Scripps Institution of Oceanography, University of California, San Diego

SELECTED CONFERENCE PRESENTATIONS

Behrens, J., S. Constable, M. Everett, and L. MacGregor (2003), Electrical Conductivity and Anisotropy in Pacific Lithosphere, paper presented at AGU Fall Meeting, San Francisco.

Behrens, J., S. Constable, G. Heinson, M. Everett, C. Weiss, K. Key, and D. Rippe (2004), Estimating Mantle Hydration from In-Situ Electrical Conductivity, paper presented at AGU Fall Meeting, San Francisco.

Behrens, J., L. MacGregor, S. Constable, and M. Everett (2002), Electrical Anisotropy in the Seafloor: CSEM Results from APPLE, paper presented at 16th Workshop on Electromagnetic Induction in the Earth, Santa Fe, New Mexico.

Constable, S., K. Key, J. Behrens, and C. Weiss (2004), Hydrocarbon Exploration Using Marine Controlled-Source EM, paper presented at AGU Fall Meeting, San Francisco.

Key, K., S. Constable, J. Behrens, G. Heinson, and C. Weiss (2004), A look at the data from "Constraining the Magmatic Budget of the EPR at 9 N Using Broadband Marine MT", paper presented at American Geophysical Union Fall Meeting, San Francisco.

Sauter, A., L. Dorman, and J. Behrens (2000), Development of a Seismo-Implosive Acoustic Device, paper presented at AGU Spring Meeting, Washington, D.C.

Weitemeyer, K., S. Constable, K. Key, and J. Behrens (2004), A Pilot Marine EM Study of Hydrate Ridge, Oregon, paper presented at American Geophysical Union Fall Meeting, San Francisco.

ABSTRACT OF THE DISSERTATION

The Detection of Electrical Anisotropy in 35 Ma Pacific Lithosphere:
Results from a Marine Controlled-Source Electromagnetic Survey
and Implications for Hydration of the Upper Mantle

by

James Philip Behrens

Doctor of Philosophy in Earth Sciences

University of California, San Diego, 2005

Steven Constable, Chair

Tectonic processes associated with seafloor spreading are known to generate anisotropic fabric in oceanic lithosphere. Anisotropy in seismic refraction data has long been attributed to preferred orientation of the olivine crystal lattice, caused by ductile deformation of the warm uppermost mantle near spreading ridges, which is frozen into place upon cooling. The lithosphere in bulk, however, is several orders of magnitude more electrically conductive than the silicates that dominate its constitution; anisotropic conductivity is therefore indicative of the distribution of electrically conductive minor mineral and fluid phases.

Marine Controlled-Source Electromagnetic (CSEM) sounding data from the Anisotropy and Physics of the Pacific Lithosphere Experiment (APPLE) indicate anisotropic electrical conductivity in 35 Ma lithosphere that had been generated at the fast-spreading East Pacific Rise. 1-D modeling and inversion show that the data require some amount of anisotropy in the uppermost mantle. The preferred model simulates vertical "sheets" of increased conductivity, aligned normal to the fossil spreading direction, more conductive by a factor of at least 2-3. This anisotropic layer begins at the Moho and continues for at least 10 km into the upper mantle – a conclusion supported through the use of two different modeling codes

and two different inversion methods applied to independent subsets of the data. Models in which the crust is the only anisotropic layer are fundamentally incompatible with the observed data.

Hydrothermal circulation of seawater into the lithosphere begins at the ridge and may continue for tens of millions of years; ridge-parallel vertical cracks and faults provide conduits through the entire crust and into the upper mantle. Mantle peridotites are serpentinized when hydrated at temperatures below ~500°C; associated magnetite formation increases bulk electrical conductivity. A mixing law relationship indicates that at least ~0.1% serpentinization by volume is required to match the preferred conductivity model, with 1% a reasonable estimate. Applied to the vertical sheets model, that corresponds to a 100 m wide zone of serpentinization every 10 km.

Chapter 1

Introduction

1.1 Motivation

Lithospheric genesis at seafloor spreading centers occurs in conjunction with a number of extensional tectonic processes. These include: emplacement of the sheeted dikes, orientation *en masse* of the a-axis of upper mantle olivine, and thermal contraction and subsequent gravitationally driven normal faulting of the lithosphere as it cools off-axis. Hydrothermal circulation of seawater through the fractured, porous crust is common, perhaps ubiquitous, and results in heterogeneous deposition of secondary minerals. These processes affect electrical conductivity at various depths in the lithosphere, and may leave anisotropic fabric frozen in

place. Thus, by measuring lithospheric electrical conductivity through inductive electromagnetic sounding and determining the degree of anisotropy therein, new insights may be gained regarding the formation and evolution of the seafloor.

Various experiments have been conducted over the years to measure the electrical properties of the Northeast Pacific Plate and its underlying aesthenosphere (sections 1.3.2, 2.2). One result of the PEGASUS Controlled-Source ElectroMagnetic (CSEM) sounding experiment was tantalizing evidence of anisotropic bulk electrical conductivity in 40 Ma Pacific lithosphere [Everett and Constable, 1999], interpreted to be ridge-perpendicular dipping lineaments of enhanced conductivity within the lithosphere. The limited source-receiver geometries available in that experiment, however, were insufficient to constrain the depth, ratio, or orientation of the anisotropy very well. This state of affairs motivated a follow-up experiment, with the primary goal of characterizing any electrical anisotropy present in either the lithosphere or aesthenosphere near the PEGASUS survey area.

In February-March 2001, CSEM data were acquired as part of the Anisotropy and Physics of the Pacific Lithosphere Experiment (APPLE). This was a collaborative effort between scientists from Scripps Institution of Oceanography (SIO), Southampton Oceanography Centre (SOC), Flinders/Adelaide Universities, and Texas A&M University; funding for the project was provided by the National Science Foundation (NSF). All CSEM data were collected during 17 days at sea aboard the R/V Thompson (cruise TN-121), operated by the University of Washington. Broadband and long-period MagnetoTelluric (MT) data were also collected, but discussion in this dissertation is mainly restricted to the CSEM data.

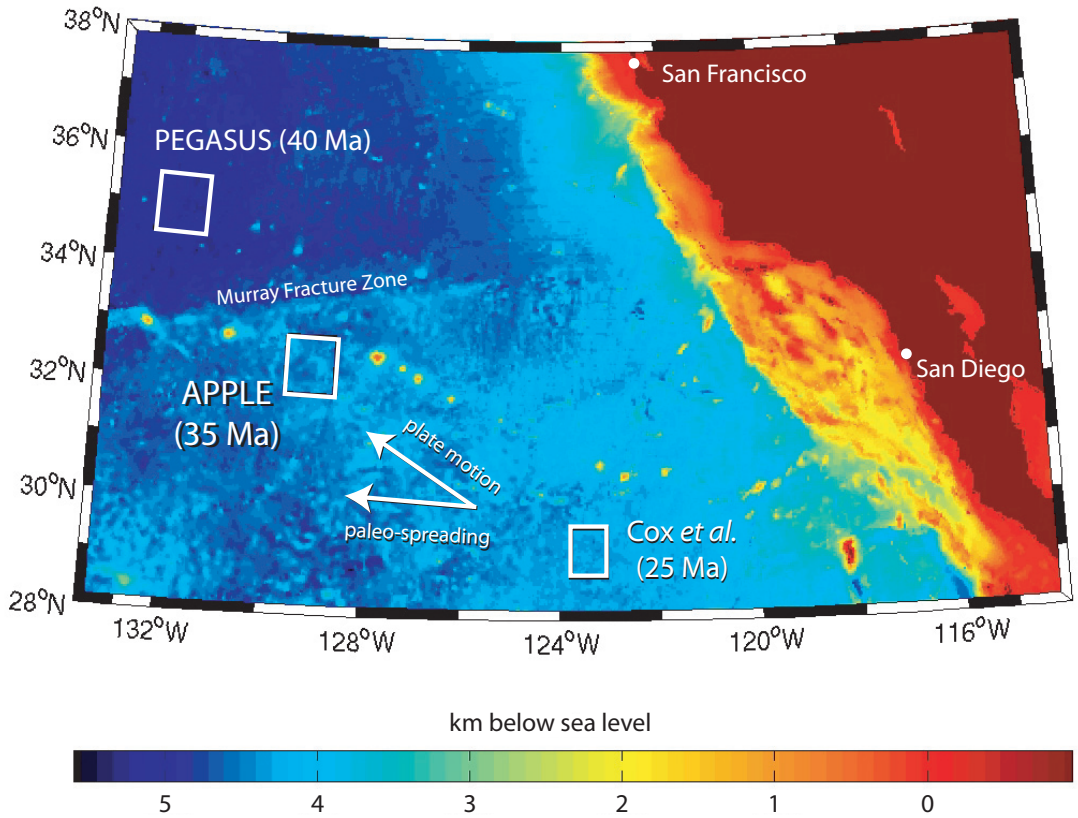

Figure 1.1 Transverse Mercator projection of Smith and Sandwell bathymetric map (v. 8.2). The rectangle at APPLE is ~100 km from north to south.

1.2 Experiment Location and Tectonic Context

The APPLE CSEM survey site (Figure 1.1) was over 35 Ma seafloor [Atwater and Severinghaus, 1989] centered at 32.25° N, 129° W, ~1000 km due west of San Diego, California. It is 300 km south-southeast of the PEGASUS survey area (40 Ma), on the south side of the Murray Fracture Zone. This site was chosen because the orientations of fossil spreading, present plate motion, and MT coast effect [Heinson and Constable, 1992] are

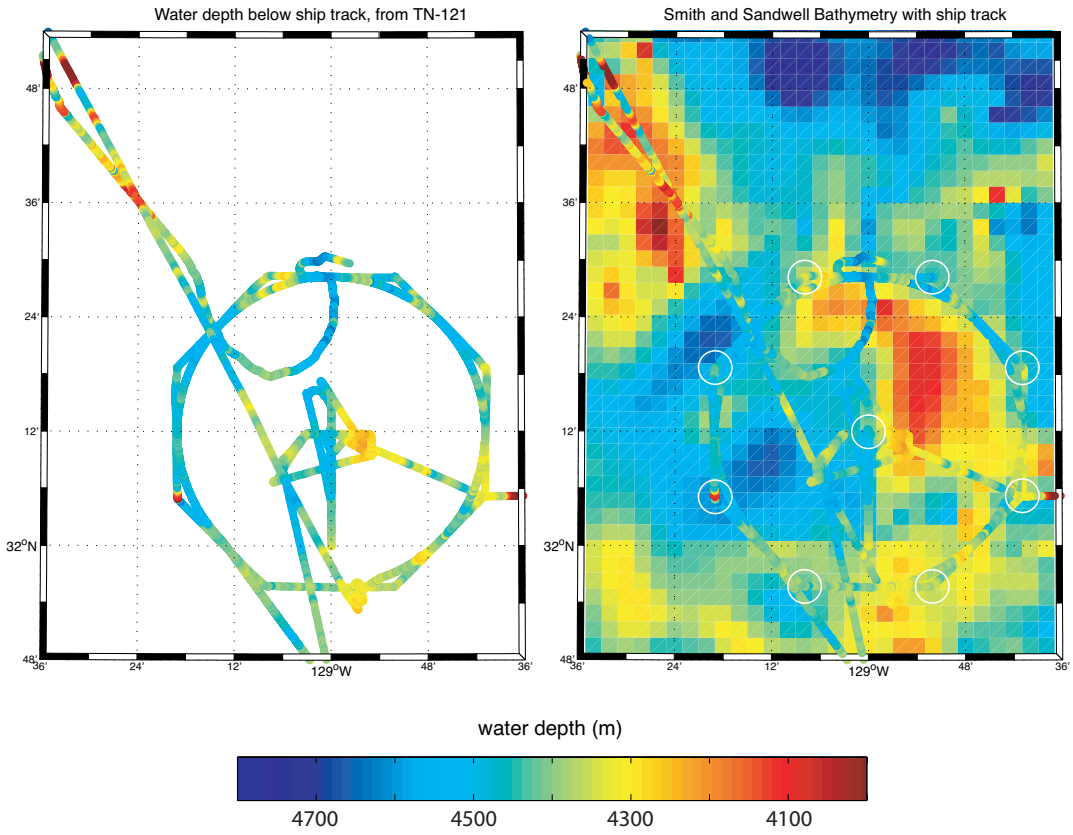

Figure 1.2 Ship track bathymetric data collected during APPLE (circle diameter 60 km) may indicate north/south trending escarpments at ~12 km spacing, and is in general agreement with Smith and Sandwell bathymetry (2' grid). Circles indicate seafloor receiver locations.

distinct from each other. Additionally, the site was logistically convenient to San Diego. Mean water depth is approximately 4400 m in the survey zone, with ~500 m of total bathymetric relief (Figure 1.2). Sediment cover is less than 100 m [Winterer, 1989]. Unfortunately, time constraints and the size of the survey site did not allow for the collection of high-resolution bathymetric data.

The lithosphere beneath the Northeast Pacific Ocean was formed by seafloor spreading between the Pacific and Farallon plates. Based on the author's interpretation of paleomagnetic

anomaly studies summarized by Atwater and Severinghaus [1989], the full spreading rate at the APPLE site was ~140 mm/yr (equivalent to the present-day spreading rate at the ultra-fast equatorial East Pacific Rise (EPR) divergent plate margin [Macdonald, 1989]). The fossil spreading direction is presently aligned nearly due east-west, perhaps rotated counterclockwise by up to 5°. The APPLE site lies within 100 km of the Murray Fracture Zone (MFZ). The site is free of any observed propagating rifts or pseudofaults, although the trace of a dying rift runs north-northwest nearby to the east [Atwater and Severinghaus, 1989]. "Disturbed zones" (in terms of the magnetic anomalies) occupy large areas of the seafloor nearby to the south and west, interpreted to be pieces of the Farallon plate emplaced during ridge jumps and ridge propagation in the time interval 45-33 Ma, the start of which is roughly coincident with the bend in the Hawaiian-Emperor chain. These ridge jumps served to reduce the offset of the spreading center across the MFZ.

The EPR segment that formed the APPLE lithosphere began interacting with the North American plate around 10 Ma, and is now responsible for rifting in the northern Gulf of California and Salton Trough, and strike-slip motion along the San Andreas, San Jacinto, and Elsinore fault systems.

Hummocky abyssal hill terrain covers the region around the APPLE site. Escarpments trending generally north-south, perpendicular to the fossil spreading direction, are evident and repeat with a wavelength on the order of 10 km. These indicate the presence of major high-angle normal faults that differentiate large blocks in the horst-and-graben structure typical of oceanic crust.

A number of northwesterly trending features are evident in the region, oriented at approximately 45° from the fossil spreading direction: the Fieberling-Guadalupe linear seamount chain just east of the APPLE site, and, progressively westward: secondary transform

offsets cutting obliquely across the MFZ, a pair of diffuse seamount chains, and the Hawaiian Islands. Long-wavelength (~100 km) bathymetric undulations underlie the region, also oriented northwesterly. Linearly progressive ages of the Hawaiian and Fieberling/Guadalupe chains [Jarrard and Clague, 1977; Pringle*, et al.*, 1991] support direct correlation with plate motion relative to long-lived, stationary hotspots in the underlying mantle. The other features mentioned have not been correlated to plate motion relative to the mantle – long-wavelength bathymetry and diffuse seamount chains could perhaps be the result of warping and cracking of the plate due to stresses applied during subduction of the ridge below North America.

1.3 Structure and Composition of Pacific Lithosphere

Seismic, borehole [*e.g.*, Becker*, et al.*, 1989], and ophiolite [*e.g.*, Bosch*, et al.*, 2004; Salisbury and Christensen, 1978] studies have established typical layer thicknesses and petrologic profiles for oceanic lithosphere [Blatt and Tracy, 1996]. In the absence of direct ground-truth measurements at the APPLE site, these must be relied upon to provide a structural and compositional reference model (Figure 2.4).

Beneath the sediments lie several hundred meters of pillow basalts, the result of extrusive lava flows at the ridge axis. These tend to be highly fractured and permeable, pore spaces saturated with seawater and fractures lined with hydrothermal alteration minerals.

Beneath the pillow basalts lie the sheeted dikes, former conduits between the axial magma chamber and seafloor lava flows. Ophiolite and borehole studies indicate that the sheets are approximately vertical, aligned normal to the spreading direction, and are ~ 1 m thick with fine-grained glassy chilled margins. The entire sheeted dike complex is typically 1.5 – 2 km from top to bottom. A textural transition from fine-grained basalt to coarser

dolerite occurs with increasing depth. Mafic (literally, "magnesio-ferric") silicates are the dominant rock-forming minerals in oceanic crust.

Beneath the sheeted dikes are the gabbros, the denser, phaneritic remnant of the axial magma chamber. Gabbros are composed mainly of pyroxene and plagioclase, with increasing amounts of olivine in cumulate lenses at greater depths.

The base of the gabbros coincides with the Moho, a discontinuity in seismic velocity at the crust-mantle boundary that corresponds to a change in composition to progressively denser ultramafic (less than 45% silica) peridotites: Lherzolite, a mix of olivine, clinopyroxene, and orthopyroxene with varying amounts of garnet, is considered the undepleted source of the axial magma chamber. During depletion, olivine/orthopyroxene harzburgite and olivine-dominated dunite are deposited in the uppermost mantle.

A regional seismic refraction study [Shor*, et al.*, 1969] found the mean thickness of the northeast Pacific crust to be 6.7 km; at the station (32°50'N 127°04'W) closest to APPLE, the Moho was estimated to be 6.51 km below the seafloor.

1.3.1 Temperature and pressure

The halfspace cooling model of Parsons and Sclater [1977], parameterized for the Northeast Pacific plate (Figure 1.3.a), provides a reference lithospheric thermal gradient at APPLE. By the time the lithosphere has reached 35 million years, the Moho has cooled to 150-200°C, and the brittle-ductile transition (~700°C [Nicolas*, et al.*, 2003]) occurs at least 30 km below the seafloor. Pressure increases with depth, and is straightforward to estimate using PREM as a guide: at seafloor of water depth 4400 m, ambient pressure is 44 MPa; at the Moho it has increased to 230 MPa; by 20 km below the seafloor, it has reached ~600 MPa.

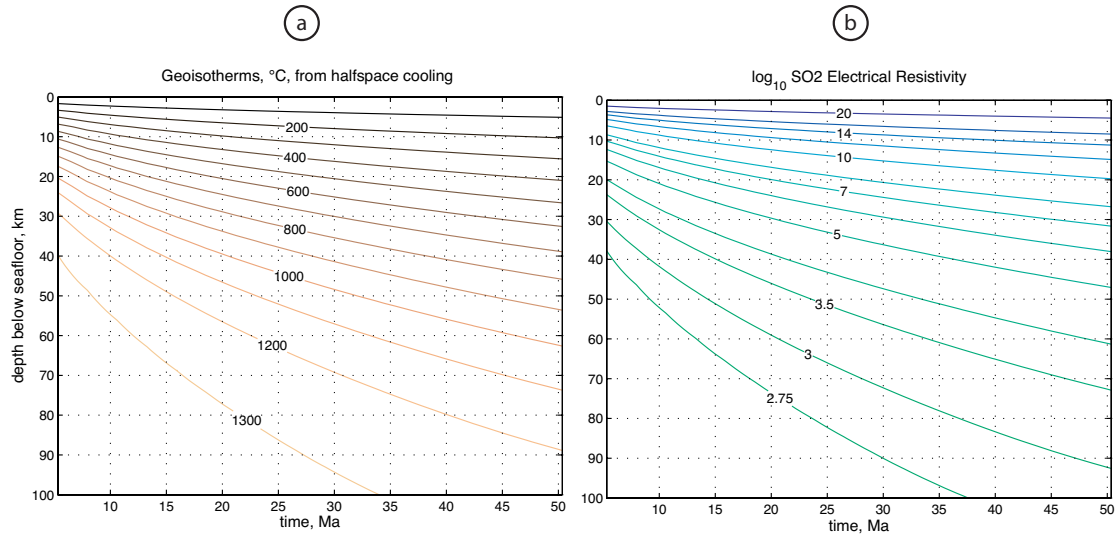

Figure 1.3 (a) Lithospheric temperatures in the northeast Pacific plate, as predicted by parameterized halfspace cooling [Parsons and Sclater, 1977]. (b) This temperature profile applied to the SO2 thermally-activated olivine conductivity model [Constable, *et al.*, 1992].

1.3.2 Electrical conductivity

Electrical conductivity σ in Siemens per meter (S/m, occasionally mho/m) and its reciprocal, electrical resistivity $\rho = \sigma^{-1}$ in Ohm-meters $(\text{Ohm} \cdot \text{m, or } \Omega\text{m})$ are both used to describe the same quantity, depending on the context. Electrical resistivity is a general property of a material, and is defined as the resistance of a sample of that material, multiplied by cross-sectional area and normalized by length – a 1 m^3 cube of 1 Ωm material behaves as a 1 Ω resistor.

Prior to APPLE, the most extensive CSEM experiment over mature Pacific lithosphere was PEGASUS. The preferred resistivity model from data inversion [Constable and Cox, 1996] (Figure 5.1) indicates 10 Ωm in the extrusives, increasing steadily through the sheeted

dikes and gabbros to resistivities of 10^4-10^5 Ωm in the uppermost mantle. Data from a CSEM experiment over freshly formed EPR crust [Evans, 1991] re-interpreted by Constable and Cox [1996] indicated the same resistivity in the top 1 km, with sheeted dikes of around 100 Ωm. Data from a CSEM experiment over 25 Ma Northeast Pacific lithosphere [Cox*, et al.*, 1986] was compatible with crust of 10^3 Ωm over a mantle of at least 5×10^4 Ωm (Figure 5.1).

The most thoroughly analyzed borehole to date that has penetrated intermediate-fast spreading crust through the sheeted dikes into the gabbros was 504B, into 5.9 Ma Nazca Plate near the Costa Rica Rift. Borehole laterolog resistivity measurements [Pezard, 1990] (Figure 5.1) indicated 10 Ωm in the extrusives, increasing to 250 Ωm in the sheeted dikes. Collection of cores, laboratory analysis of sample resistivities and pore fluids, and permeability estimates based on heat flow measurements provided ground truth, resulting in a significant advance in the parameterization and utility of mixing law relationships for seawater-infiltrated fractured crystalline mafic rocks.

Archie's Law is the starting point for mixing laws that predict bulk rock conductivity σ as a function of the pore fluid conductivity σ_w and porosity $\varnothing$:

$$\sigma = a\,\sigma_w \varnothing^{-m} \tag{1.3.1}$$

where *a* and *m* are empirically determined parameters; Pezard [1990] indicates *a* = 9.1 and *m* = 1.05 were initially used to interpret the Hole 504B data. More generally, Hashin and Shtrikman [1962] presented a method of determining the bounds of bulk conductivity of any two-phase system: the lower bound σ_{HS^-} when the more conductive phase is in isolated spheres (*i.e.* porous, but not permeable), and the upper bound σ_{HS^+} when it forms a

completely interconnected network. For a conductive phase of σ_C within a more resistive material of σ_0,

$$\begin{aligned} \sigma_{HS^-} &= \sigma_0 + \varnothing\left(\frac{1}{\sigma_C - \sigma_0} + \frac{1-\varnothing}{3\sigma_0}\right)^{-1} < \sigma \\ \sigma_{HS^+} &= \sigma_C + (1-\varnothing)\left(\frac{1}{\sigma_0 - \sigma_C} + \frac{\varnothing}{3\sigma_C}\right)^{-1} > \sigma. \end{aligned} \tag{1.3.2}$$

Geometric distribution of the conductive phase within the host rock has a profound effect on bulk resistivity (Figure 5.2). These and several other mixing laws are reviewed by Schmeling [1986].

A substantial number of laboratory experiments have been carried out to determine electrical properties of mafic and ultramafic rocks and minerals [see reviews by Parkhomenko, 1982; Tyburczy and Fisler, 1995]. In general, mafic silicate minerals in pure anhydrous form are orders of magnitude more resistive than bulk oceanic crust and lithospheric upper mantle. The SO2 (Standard Olivine 2) model of anhydrous olivine conductivity [Constable*, et al.*, 1992] (Figure 1.3.b), for instance, predicts $\rho \approx 10^{14}$ Ωm in the uppermost mantle at an age of 35 Ma. (SO2 represents thermally activated conduction through olivine crystals at temperatures of several hundred °C and up, and is in agreement with magnetotelluric measurements of aesthenospheric conductivity [Heinson, 1999]. Extrapolation to lower temperatures is not geologically applicable, which indicates that olivine crystals in cool lithosphere are not important conductors of electricity.)

To explain the lower resistivities encountered throughout the crust and upper mantle, the presence of more conductive minor phases, both fluid and mineralogical, must be invoked:

Pore spaces containing seawater and/or electrically conductive hydrothermal alteration minerals (such as zeolites, sulfides, etc.) greatly reduce rock resistivity. Small volumes are

sufficient – porosities of 1-10% reduce crustal resistivities to 10 Ωm at Hole 504B [Pezard, 1990]. Data from a saturated gabbro with only 0.024% moisture content indicates $\rho \simeq 10^4$ Ωm at 1 Hz [Katsube and Collett, 1976], while a dry pyroxene sample was $\rho \simeq 10^9$ Ωm [Olhoeft, 1976].

Ore minerals also make rocks more conductive: 10-14% "ore mineral" content reduced anhydrous basalts from 10^8 Ωm (0-2% ore minerals) to ~10^4 Ωm at 200 °C [Parkhomenko, 1982]. Fe_2O_3, FeO, and CaO were seen to have the greatest effect, but only at concentrations > 8%. Hydrothermal vents along the EPR discharge sulfides and iron oxides [Haymon, 1989], which are, in general, electrically conductive [Keller, 1988]. It is likely that oxides and sulfides precipitate along seawater pathways in the crust [Bonatti, 1983].

Pressure has an effect on conductivity. Cracks close by 100 MPa, inhibiting conduction through interconnected pore fluid, but pores stay open to pressures > 1 GPa [Brace and Orange, 1968]. Borehole heat flow permeability estimates [Fisher, 1998] indicate the closure of cracks by 500 m into seafloor basalts.

High temperature, and especially partial melting, increases conductivity. This is the motivation behind all the CSEM experiments at seafloor spreading centers (section 2.2) and the use of MT to study aesthenospheric conductivity [Heinson, 1999]. Lithosphere at APPLE, however, has cooled to the point where temperature will have little effect on crustal and upper mantle conductivities (section 1.3.1).

1.3.3 Serpentinization

Free water will not exist in the deepest crust and upper mantle; instead, it reacts with olivine and creates serpentine, a family of hydrous magnesium/iron sheet silicate minerals [Fryer, 2002; O'Hanley, 1996]. Forsterite (magnesium olivine) and fayalite (iron olivine)

form a solid solution; mantle xenoliths indicate that Fo_{90} is typical [Tyburczy and Fisler, 1995]. The end-member reactions follow: In the case of pure forsterite alteration,

$$\underset{\text{forsterite}}{2\ Mg_2[SiO_4]} + \underset{\text{water}}{3\ H_2O} = \underset{\text{serpentine}}{Mg_3[Si_2O_5](OH)_4} + \underset{\text{brucite}}{Mg(OH)_2}.$$

Serpentine itself is not particularly conductive [D. Bruhn, personal communication], but serpentinized peridotites often are [Lebedev and Shepel, 1981; Parkhomenko, 1982; Stesky and Brace, 1973]. This is attributed to the formation of magnetite when some amount of iron was present in the host rock:

$$\underset{\text{fayalite}}{2\ Fe_2[SiO_4]} + \underset{\text{water}}{2.33\ H_2O} = \underset{\text{serpentine}}{Fe_3[Si_2O_5](OH)_4} + \underset{\text{magnetite}}{0.33\ Fe_3O_4} + 1.33\ H_2.$$

Iron brucite may also result. In olivine, serpentine, or brucite, iron is Fe^{2+}; to form magnetite, it must be oxidized to Fe^{3+}. H_2 is formed as a byproduct of this oxidation; if enough becomes concentrated, reducing conditions occur and FeNi alloys precipitate [O'Hanley, 1996].

While serpentine + magnetite replaces olivine, serpentine + talc replaces pyroxene [Fryer, 2002]. Secondary oxidation of iron brucite also produces magnetite [O'Hanley, 1996]. Progressive serpentinization is often observed to occur around unaltered olivine grain kernels, concentrating alteration minerals at grain boundaries, where they form interconnected networks.

Magnetite is an excellent conductor of electricity. Keller [1988] reports a DC resistivity of 5.2×10^{-5} Ωm for pure magnetite. Lebedev and Shepel [1981] report an average of 10 Ωm for their serpentinized ultramafic samples, which contained 10-22% ore minerals that cut the rock in thin veins. Parkhomenko [1982] describes an increase of 3 orders of magnitude in conductivity for altered vs. unaltered gabbros, and states that the presence of magnetite at the grain boundaries was responsible. Stesky and Brace [1973] examined several serpentinized

peridotite, lherzolite, gabbro, dunite, and basalt specimens; they observed an increase in conductivity of 3-4 orders of magnitude over that of unserpentinized rocks of similar composition for samples with > 5% magnetite.

1.4 Possible Causes of Lithospheric Electrical Anisotropy

Hydrothermal circulation of seawater into the crust is required to reduce rock resistivities to values observed in samples and inferred from induction sounding. At the EPR, hydrothermal vents are found grouped in linear fields extending 5 to 20 km along the ridge crest; on the flank of the intermediate-rate Galapagos rift, warm fluids emanate from ridge-parallel faults [Haymon, 1989]. Studies of the Oman ophiolite, formed at a fast-spreading ridge, find microcracks and hydrothermal alteration minerals aligned parallel to the sheeted dike complex [Bosch*, et al.*, 2004]. It is therefore likely that electrical conductivity in mature lithosphere will be enhanced in the vertical and paleo-ridge-parallel directions, relative to the paleo-spreading direction – north-south trending vertical "sheets" of increased conductivity at the APPLE site. Whether this effect is confined to the sheeted dikes, or whether it continues deeper into the crust and perhaps upper mantle is a function of the thermal and hydrothermal evolution of the plate, its initial composition, and post-formation accumulation of strain.

P-wave lithospheric travel time anisotropy studies at several sites in the northeast Pacific [Raitt*, et al.*, 1971] found lithospheric upper mantle velocity anisotropy of 3-8%, with the fast direction parallel to the fossil spreading direction. Shearer and Orcutt [1985] used this result to deduce the fossil spreading direction at a location where the magnetic anomaly data was ambiguous.

The physical origin of this seismic anisotropy is anisotropic mineral texture in the upper mantle [*e.g.*, Blackman*, et al.*, 1996]. The seismically fast a-axis of olivine is preferentially

oriented in the direction of ductile flow in the upper mantle; away from the spreading ridge this fabric is frozen into place, with lattice-preferred orientation of the a-axis generally horizontal and normal to the spreading ridge.

While laboratory measurements of olivine crystal conductivity indicate a small degree of anisotropy [Constable*, et al.*, 1992], the a-axis is intermediate. Karato [1990] suggested that anisotropic hydrogen diffusivity in olivine, greatest along the a-axis, could affect mantle conductivity. The strain required to orient the crystallographic axes may also form linear deposits of secondary minerals in lineations perpendicular to the ridge. A chromite lineation of this kind has been observed in the Oman ophiolite [Shackleton and Ries, 1984]. A literature search was unable to turn up laboratory measurements of pure chromite conductivity; transition metal oxides, however, are generally conductive.

Any electrical anisotropy related to strain accumulation in the uppermost mantle will likely have enhanced conductivity in the paleo-spreading direction – horizontal conductive "rods" in the east/west direction at APPLE. If present, this could serve to reduce or negate the observable effects of any paleo-ridge-parallel "sheets" anisotropy hypothesized above. An added complication is the northwesterly motion of the plate relative to the hotspot reference frame; upper mantle strain may be rotated away from the spreading direction, even at the active ridge.

1.5 Goals of the Dissertation

Now that the tectonic setting has been presented and the relevant properties of lithospheric materials summarized, the dissertation will proceed as follows: In Chapter 2, implementation of the CSEM method is described, along with an historical overview of the method and details about the forward modeling and inversion methods employed in this study. Data acquisition and processing is the subject of Chapter 3, and the modeling and inversion studies are presented in Chapter 4. In Chapter 5, results are interpreted and discussed.

It is hoped that this study will add to the overall understanding of oceanic plate formation and evolution, especially the nature, timing, and extent of hydrothermal alteration of the lithospheric upper mantle. It is also hoped that this document will be of use, more generally, to people interested in the collection, processing, modeling, and interpretation of marine CSEM data for any given application.

1.6 References

Atwater, T., and J. Severinghaus (1989), Tectonic maps of the northeast Pacific, in The Eastern Pacific Ocean and Hawaii, edited by E. L. Winterer, et al., pp. 15-20, Geological Society of North America, Boulder, Colorado.

Becker, K., H. Sakai, A. C. Adamson, J. Alexandrovich, J. C. Alt, R. N. Anderson, D. Bideau, R. Gable, P. M. Herzig, S. Houghton, H. Ishizuka, H. Kawata, H. Kinoshita, M. G. Langseth, M. A. Lovell, J. Malpas, H. Masuda, R. B. Merrill, R. H. Morin, M. J. Mottl, J. E. Pariso, P. Pezard, J. Phillips, J. Sparks, and S. Uhlig (1989), Drilling deep into young oceanic crust at Hole 504B, Costa Rica rift, Reviews of Geophysics, 27, 79-102.

Blackman, D. K., J. M. Kendall, P. R. Dawson, H. R. Wenk, D. Boyce, and J. P. Morgan (1996), Teleseismic imaging of subaxial flow at mid-ocean ridges; traveltime effects of anisotropic mineral texture in the mantle, Geophysical Journal International, 127, 415-426.

Blatt, H., and R. Tracy (1996), Petrology: igneous, sedimentary, and metamorphic, 2nd ed., W. H. Freeman, New York.

Bonatti, E. (1983), Hydrothermal metal deposits from the oceanic rifts: A classification, in Hydrothermal Processes at Seafloor Spreading Centers, edited by P. A. Rona, et al., pp. 491-502, Plenum Press, New York and London.

Bosch, D., M. Jamais, F. Boudier, A. Nicolas, J.-M. Dautria, and P. Agrinier (2004), Deep and high-temperature hydrothermal circulation in the Oman ophiolite - petrological and isotopic evidence, Journal of Petrology, 45, 1181-1208.

Brace, W. F., and A. S. Orange (1968), Further studies on the effects of pressure on electrical resistivity of rocks, Journal of Geophysical Research, 73, 5407-5420.

Constable, S., and C. S. Cox (1996), Marine controlled-source electromagnetic sounding 2. The PEGASUS experiment, Journal of Geophysical Research, 101, 5519-5530.

Constable, S., T. J. Shankland, and A. Duba (1992), The electrical conductivity of an isotropic olivine mantle, Journal of Geophysical Research, 97, 3397-3404.

Cox, C. S., S. C. Constable, A. D. Chave, and S. C. Webb (1986), Controlled-source electromagnetic sounding of the oceanic lithosphere, Nature, 320, 52-54.

Evans, R. L. (1991), Electrical Resistivity Structure of the East Pacific Rise Near 13° N, Ph.D. thesis, 229 pp, University of Cambridge.

Everett, M. E., and S. Constable (1999), Electric dipole fields over an anisotropic seafloor: theory and application to the structure of 40 Ma Pacific Ocean lithosphere, Geophysical Journal International, 136, 41-56.

Fisher, A. T. (1998), Permeability within basaltic oceanic crust, Reviews of Geophysics, 36, 143-182.

Fryer, P. (2002), Recent studies of serpentinite occurrences in the oceans: mantle-ocean interactions in the plate tectonic cycle, Chemie der Erde/Geochemistry, 62, 257-302.

Hashin, Z., and S. Shtrikman (1962), A variational approach to the theory of the effective magnetic permeability of mulitphase materials, Journal of Applied Physics, 33, 3125-3131.

Haymon, R. M. (1989), Hydrothermal processes and products on the Galapagos Rift and East Pacific Rise, in The Eastern Pacific Ocean and Hawaii, edited by E. L. Winterer, et al., Geological Society of North America, Boulder, Colorado.

Heinson, G. (1999), Electromagnetic studies of the lithosphere and asthenosphere, Surveys in Geophysics, 20, 229-255.

Heinson, G., and S. Constable (1992), The electrical conductivity of the oceanic upper mantle, Geophysical Journal International, 110, 159-179.

Jarrard, J. D., and D. A. Clague (1977), Implications of Pacific Island and seamount ages for the origin of volcanic chains, Reviews of Geophysics and Space Physics, 15, 57-76.

Karato, S. (1990), The role of hydrogen in the electrical conductivity of the upper mantle, Nature, 347, 272-273.

Katsube, T. J., and L. S. Collett (1976), Electromagnetic Propagation Characteristics of Rocks, in The Physics and Chemistry of Minerals and Rocks: Proceedings of the NATO Advanced Study Institute on Petrophysics, held at the University of Newcastle upon Tyne, 22-26 April 1974, edited by R. G. J. Strens, John Wiley & Sons.

Keller, G. V. (1988), Rock and Mineral Properties, in Electromagnetic Methods in Applied Geophysics: Volume 1, Theory, edited by M. N. Nabighian, pp. 13-51, Society of Exploration Geophysicists, Tulsa, OK.

Lebedev, T. S., and S. I. Shepel (1981), On the nature of increased electrical conductivity of some rocks, Geophysical Journal, 3, 835-852.

Macdonald, K. C. (1989), Tectonic and magmatic processes on the East Pacific Rise, in The Eastern Pacific Ocean and Hawaii, edited by E. L. Winterer, et al., Geological Society of North America, Boulder, Colorado.

Nicolas, A., D. Mainprice, and F. Boudier (2003), High-temperature seawater circulation throughout crust of oceanic ridges: A model derived from the Oman ophiolites, Journal of Geophysical Research, 108, 2371.

O'Hanley, D. S. (1996), Serpentinites: records of tectonic and petrological history, 277 pp., Oxford University Press, Oxford.

Olhoeft, G. R. (1976), Electrical properties of rocks, in The Physics and Chemistry of Minerals and Rocks: Proceedings of the NATO Advanced Study Institute on Petrophysics, held at the University of Newcastle upon Tyne, 22-26 April 1974, edited by R. G. J. Strens, pp. 261-278, John Wiley & Sons.

Parkhomenko, E. I. (1982), Electrical resistivity of minerals and rocks at high temperature and pressure, Reviews of Geophysics and Space Physics, 20, 193-218.

Parsons, B., and J. G. Sclater (1977), An analysis of the variation of ocean floor bathymetry and heat flow with age, Journal of Geophysical Research, 82, 803-827.

Pezard, P. (1990), Electrical properties of mid-ocean ridge basalt and implications for the structure of the upper oceanic crust in hole 504B, Journal of Geophysical Research, 95, 9237-9264.

Pringle, M. S., H. Staudigel, and J. Gee (1991), Jasper Seamount: Seven million years of volcanism, Geology, 19, 364-368.

Raitt, R. W., G. G. Shor, G. B. Morris, and H. K. Kirk (1971), Mantle anisotropy in the Pacific Ocean, Tectonophysics, 12, 173-186.

Salisbury, M., and N. Christensen (1978), The seismic velocity structure of a traverse through the Bay of Island ophiolite complex, Newfoundland, an exposure of oceanic crust and upper mantle, Journal of Geophysical Research, 83, 805-817.

Schmeling, H. (1986), Numerical models on the influence of partial melt on elastic, anelastic and electrical properties of rocks. Part II: electrical conductivity, Physics of the Earth and Planetary Interiors, 43, 123-136.

Shackleton, R. M., and A. C. Ries (1984), The relation between regionally consistent stretching lineations and plate motions, Journal of Structural Geology, 6, 111-117.

Shearer, P., and J. Orcutt (1985), Anisotropy in the oceanic lithosphere: Theory and observations from the Ngendie seismic refraction experiment in the southwest Pacific, Geophysical Journal of the Royal Astronomical Society, 80, 493-526.

Shor, G. G., H. W. Menard, and R. W. Raitt (1969), Structure of the pacific basin, in The Sea v. 4 pt. II, edited by A. E. Maxwell, pp. 3-27, Wiley, New York.

Stesky, R. M., and W. F. Brace (1973), Electrical conductivity of serpentinized rocks to 6 kilobars, Journal of Geophysical Research, 78, 7614-7621.

Tyburczy, J. A., and D. K. Fisler (1995), Electrical Properties of Minerals and Melts, in Mineral Physics and Crystallography: A Handbook of Physical Constants, edited by T. Ahrens, pp. 185-208, American Geophysical Union, Washington, DC.

Winterer, E. L. (1989), Sediment thickness map of the northeast Pacific, in The Eastern Pacific Ocean and Hawaii, edited by E. L. Winterer, et al., pp. 307-310, Geological Society of America, Boulder, Colorado.

Chapter 2

The Marine Controlled-Source Electromagnetic Sounding Method

2.1 Introduction

The Marine Controlled-Source Electromagnetic (CSEM) sounding method is a frequency-domain geophysical technique sensitive to the electrical conductivity of the sub-seafloor. Developed to bridge the gap between borehole resistivity measurements and deep Marine Magnetotelluric (Marine MT, or MMT) resistivity soundings, CSEM can provide information about tectonic structure, temperature at depth, rock porosity, mineral composition, and pore fluid properties.

The CSEM method referred to and described herein involves transmitting energy at approximately 1 Hz from an artificial Horizontal Electric Dipole (HED) source deeptowed at or near the seafloor to an array of horizontal electric dipole receivers deployed at the seafloor (Figure 2.4). Vertical dipoles have recently been added to the receivers, as well. This incarnation of CSEM is also known as active-source EM sounding, MCSEM (Marine CSEM), and as the proprietary terms Sea Bed Logging (Statoil) and R3M (ExxonMobil).

2.2 A Brief History

2.2.1 Naval research

U.S. Naval researchers began investigating ways to determine seafloor electrical resistivity as early as the 1960s; a practical motivation was to determine whether the seafloor could be used as a waveguide for VLF (very low frequency) communications. Both HED and Horizontal Magnetic Dipole (HMD) active source sounding methods were considered; basic modeling theory was developed, as were some early seafloor electric and magnetic field sensors [Bannister, 1968]. Land-based electromagnetic geophysical sounding dates back to the early 20th century, however, and so practical methods and modeling theory were well established for land studies [*i.e.*Vanyan, 1967] by the time they were being adapted for use at the seafloor.

2.2.2 Academic experiments

Researchers at the Scripps Institution of Oceanography (SIO) pioneered the use of MMT and HED Marine CSEM to study tectonic processes. MMT sensors were deployed in both the North Pacific and North Atlantic; these data indicated an electrically conductive aesthenosphere [Filloux, 1977]. The first CSEM measurement was made near the East Pacific Rise at 21°N [Spiess*, et al.*, 1980; Young and Cox, 1981] using a nearly stationary transmitter

and data from one receiver; data were consistent with seawater-infiltrated basalt conductivity and suggestive of anisotropy related to spreading ridge hydrothermal processes. Motivated by the success of this experiment, the ELectromagnetic Field (ELF) receiver [Webb, *et al.*, 1985] was developed and several were manufactured. A 1-D, isotropic forward modeling code was also developed [Chave and Cox, 1982] (section 2.4.1). A survey carried out over 25 Ma northeastern Pacific lithosphere [Cox, *et al.*, 1986] was the first to employ a towed transmitter, dragged across the seafloor, that provided dynamic source-receiver geometries; the data were compatible with a crust $\rho = 10^3$ Ωm over a more resistive upper mantle $\rho > 5\text{x}10^4$ Ωm. A review by Constable [1990] summarizes early CSEM work alongside other marine electromagnetic induction studies, with a focus on mantle conductivity.

A group at the University of Toronto postulated and developed the Modified Magnetometric Resistivity (MMR) method, a galvanic technique that utilizes measurements of the magnetic field at the seafloor, with a vertical electric bipole source in the seawater [Edwards, *et al.*, 1981] – bipole referring to a transmitter that is too long, relative to the source-receiver offsets, to be considered infinitesimal. Time-domain dipole-source electromagnetic sounding has been developed in theory [Cheesman, *et al.*, 1987; Everett and Edwards, 1992; Yu, *et al.*, 1997] and implemented in practice [Cairns, *et al.*, 1996] by the Toronto group.

A review by Chave, *et al.* [1991] details the various marine EM methods and equipment in use at the time.

The PEGASUS CSEM data set [Constable and Cox, 1996] was collected over 40 Ma northeastern Pacific lithosphere in 1988 (section 1.3.2). For the analysis, 1-D isotropic forward modeling capability was improved [Flosadóttir and Constable, 1996] and integrated with the Occam smooth inversion algorithm [Constable, *et al.*, 1987] (section 2.5.2).

Anisotropic halfspace modeling capabilities were developed and used to analyze the PEGASUS data [Everett and Constable, 1999].

A group at Cambridge University (which later moved to Southampton Oceanography Centre) began collaborating with the SIO group in the late 1980s. The Cambridge group developed the Deeptowed Active Source Instrument (DASI) [Sinha*, et al.*, 1990], a transmitter designed to be towed tens of meters above the seafloor at the end of the ship's winch line (section 3.2), allowing CSEM soundings over areas not covered in abyssal mud – active divergent plate margins in particular. Several experiments were conducted as a combined effort of both groups:

A survey over the fast-spreading East Pacific Rise at 13°N [Evans*, et al.*, 1994] found no conductive anomaly below the ridge axis, indicating relative magmatic quiescence.

A survey over the slow-spreading Reykjanes Ridge at 57°45'N [MacGregor*, et al.*, 1998] did find strong evidence of a low-resistivity anomaly 2 km below the ridge axis, coincident with a seismically imaged low-velocity zone, and interpreted to be a cyclically-recharged crustal magma chamber.

A survey over the Valu Fa Ridge, a back-arc intermediate-rate spreading center in the Lau Basin [MacGregor*, et al.*, 2001] indicated an anomalously conductive crust, interpreted to be the result of vigorous hydrothermal circulation. This data set was analyzed using a 2.5-D forward algorithm (3-D point source dipole field over a 2-D earth resistivity model) [Unsworth*, et al.*, 1993] in conjunction with a 2-D Occam inversion routine [deGroot-Hedlin and Constable, 1990].

2.2.3 Industry involvement

Industry funding via the Seafloor Electromagnetic Methods Consortium (SEMC) supported the development of a new generation seafloor MMT data logger and sensor system [Constable, *et al.*, 1998]. The Ocean Bottom ElectroMagnetic reciever (OBEM Mk II) featured a lower noise floor, a 16-bit A/D converter (now 24-bit with the Mk III), and orthogonal induction coil magnetometers (formerly, fluxgate magnetometers had been used), while continuing the use of silver-silver chloride electrodes. The pass band was extended to higher frequencies, making broadband seafloor MMT possible, indicated by successful MMT imaging of the Gemini salt body in the Gulf of Mexico and the magma chamber below the East Pacific Rise at 9°N [Key, 2003]. The OBEM Mk II and III were well suited for use in joint MMT/CSEM surveys.

Joint MMT/CSEM surveys have proven to be a useful supplement to seismic methods in offshore hydrocarbon exploration. Statoil commissioned the first CSEM survey for direct detection of hydrocarbons in late 2000 [Eidesmo, *et al.*, 2002; Ellingsrud, *et al.*, 2002]; the data were acquired, processed, and initially analyzed in conjunction with the combined SIO and Southampton academic groups. It was confirmed that a CSEM sounding could indeed detect the presence of oil in the subsurface, and demarcate the reservoir edge by comparison with a relatively simple 2-D block modeling study based on *a priori* seismic imaging. MMT data were inverted to generate a background sediment resistivity model.

In the wake of this success, three new companies were formed to provide industrial marine EM surveys: Offshore Hydrocarbon Mapping (OHM) was spun off from the Southampton group, AOA Geomarine Operations (AGO) was spun off from AOA Geophysics and licensed the SIO receivers for commercial use, and ElectroMagnetic GeoServices (EMGS) was spun off from Statoil. AGO and OHM were contracted by ExxonMobil to

acquire a series of surveys together; the author of this work was an at-sea consultant during the first two data acquisition cruises. ExxonMobil's use of marine CSEM was eventually publicized in the popular press [Warren, 2004]. EMGS, using a transmitter built by Siemens and clones of the SIO receiver built by ElectroMagnetic Instruments (EMI), acquired data for various oil companies.

2.2.4 Recent surveys

Industry involvement has funded the development of a new deeptowed transmitter by the SIO EM Lab, the Scripps Underwater EM Source Instrument (SUESI). The fleet of academic OBEM Mk III receivers has been greatly expanded, as well. This equipment has been used to acquire new academic data sets over the Gemini salt body, Hydrate Ridge [Weitemeyer*, et al.*, 2004], and, with funding from the NSF, a wide-aperture survey over the East Pacific Rise at 9°N [Key*, et al.*, 2004]. The Toronto group has also been furthering the use of CSEM for gas hydrate detection [Schwalenberg*, et al.*, 2005].

2.3 Principles of CSEM

2.3.1 Governing equations

This section follows the example of MacGregor [1997], Evans [1991], Keller [1988], and Ward and Hohmann [1988].

The concurrent electric field **E,** magnetic field **H**, magnetic flux density **B**, and electric displacement **D** in a medium are related through Maxwell's equations of electromagnetic induction, represented here in differential form for magnetic and/or polarizable material:

$$\nabla \cdot \mathbf{E} = \frac{q}{\varepsilon} \tag{2.3.1}$$

$$\nabla \cdot \mathbf{B} = 0 \tag{2.3.2}$$

$$\nabla \times \mathbf{E} = -\frac{\partial \mathbf{B}}{\partial t} \tag{2.3.3}$$

$$\nabla \times \mathbf{H} = \frac{\partial \mathbf{D}}{\partial t} + \mathbf{J} \tag{2.3.4}$$

where q is charge density and ε is the dielectric permittivity of the medium. Pertinent constitutive relationships are:

$$\mathbf{J} = \sigma \mathbf{E} + \mathbf{J}_S \tag{2.3.5}$$

$$\mathbf{D} = \varepsilon \mathbf{E} \tag{2.3.6}$$

$$\mathbf{B} = \mu \mathbf{H}\,. \tag{2.3.7}$$

Current density **J** is proportional to the inducted electric field **E** in a source-current-free region of electrical conductivity σ (via Ohm's law); the source current density $\mathbf{J}_S$ may be considered separately (section 2.4). **D** is related to **E** through the dielectric permittivity, and **B** and **H** through magnetic permeability μ (the free-space value μ_0 is often used; this approximation is valid in non-ferromagnetic materials). Equation (2.3.4) can thus be re-written as

$$\nabla \times \frac{\mathbf{B}}{\mu} = \varepsilon \frac{\partial \mathbf{E}}{\partial t} + \sigma \mathbf{E} + \mathbf{J}_S\,. \tag{2.3.8}$$

The damped vector wave equations for **E** and **B** are derived by re-arranging Maxwell's equations and applying a double-curl vector identitiy:

$$\nabla^2 \mathbf{E} = \mu\varepsilon \frac{\partial^2 \mathbf{E}}{\partial t^2} + \mu\sigma \frac{\partial \mathbf{E}}{\partial t} + \mu\, \mathbf{J}_S \tag{2.3.9}$$

$$\nabla^2 \mathbf{B} = \mu\varepsilon \frac{\partial^2 \mathbf{B}}{\partial t^2} + \mu\sigma \frac{\partial \mathbf{B}}{\partial t} + \mu\, \nabla \times \mathbf{J}_S\,. \tag{2.3.10}$$

Electromagnetic geophysical soundings are often analyzed in the frequency domain, as is the case with CSEM and MMT. At distance from source currents that oscillate with time dependence $e^{i\omega t}$, the wave equations can be written:

$$\nabla^2 \mathbf{E} = \mu\omega(\varepsilon\omega + i\sigma)\mathbf{E} = -k^2\,\mathbf{E} \tag{2.3.11}$$

$$\nabla^2 \mathbf{B} = \mu\omega(\varepsilon\omega + i\sigma)\mathbf{B} = -k^2\,\mathbf{B} \tag{2.3.12}$$

where k is the complex wave number.

The second temporal derivative term is known as the *displacement* or *radiative* term; in classical theory, it represents polarization of local charge distributions (*i.e.* atomic polarization, re-orientation of polar molecules) in response to an applied field. The displacement term is scaled by the dielectric permittivity ε, which is the capacity of the material to store charge when an electric field is applied. The free space value is ε_0 = 8.854 x 10^{-12} F/m. The dielectric constant $\kappa = \varepsilon/\varepsilon_0$ of a given medium varies with temperature and frequency; the low-frequency limit $\kappa_0 = \lim_{\omega \to 0} \kappa$, however, is generally applicable to seawater and rocks at frequencies below 1 kHz.

The first temporal derivative term is known as the *diffusion* or *induction* term; it represents larger-scale currents of charge carriers that flow through the medium. These fields decay exponentially with increasing distance from the source current. The diffusion term is scaled by the electrical conductivity σ of the medium. At 0°C, seawater σ_w = 3.2 S/m; rock-forming minerals are more resistive (section 1.3.2).

The diffusive/inductive term is many orders of magnitude stronger than the displacement/radiative term for the frequencies and materials encountered in MMT/CSEM, as indicated by values of the "loss tangent" (Table 2.1). As a result, the displacement term is dropped and EM induction is treated as a purely diffusive phenomenon:

	σ	$\kappa = \varepsilon/\varepsilon_0$	$\frac{\sigma}{\omega\varepsilon} = \tan\delta$	
			$f = 10^{-2}$ Hz	$f = 10^{0}$ Hz
Seawater (0°C, 35 ppt)	3.2 S/m (a)	80 (b)	4.5×10^{11}	4.5×10^{9}
Gabbro (wet)	10^{-4} (c)	10^{3} (c)	1.1×10^{6}	1.1×10^{4}
Pyroxene (300°C, dry)	10^{-5} (d)	90 (d)	1.3×10^{6}	1.3×10^{4}
Olivine (600°C, 1 GPa, dry)	2.5×10^{-5} (e)	< 10 (f)	2.8×10^{7}	2.8×10^{5}

Table 2.1 Electrical conductivity, low frequency dielectric constant, and the associated "loss tangent" at 0.01 Hz (typical for MMT) and 1 Hz (CSEM). For materials and frequencies encountered in Marine EM, the displacement term can be neglected. Sources: (a) [Keller, 1988]; (b) [Daout, *et al.*, 1994]; (c) [Katsube and Collett, 1976]; (d) [Olhoeft, 1976]; (e) [Tyburczy and Fisler, 1995]; (f) [Shannon, *et al.*, 1991].

$$\nabla^2 \mathbf{E} = i\mu\omega\sigma\,\mathbf{E} \tag{2.3.13}$$

$$\nabla^2 \mathbf{B} = i\mu\omega\sigma\,\mathbf{B} \tag{2.3.14}$$

and

$$k = (-i\mu\omega\sigma)^{1/2}\,. \tag{2.3.15}$$

k is complex, so it can be written

$$k = \beta_{\mathrm{Re}} - i\beta_{\mathrm{Im}}\,. \tag{2.3.16}$$

In this low-frequency diffusion approximation,

$$\beta_{\mathrm{Re}} = \beta_{\mathrm{Im}} = \left(\frac{\mu\omega\sigma}{2}\right)^{1/2}\,. \tag{2.3.17}$$

For some land- and borehole-based EM sounding methods, such as ground-penetrating radar and some time-domain methods, the displacement is a key component of the measured

field and cannot be neglected. This is also generally true in seismology. For the frequency-domain CSEM analysis presented in this dissertation, however, the diffusive term is dominant.

The simplest solution to equations (2.3.13) - (2.3.14) is a plane wave of angular frequency ω propagating through a homogeneous source-free medium, traveling parallel to the positive z-axis while oscillating in the x - y plane:

$$\mathbf{E} = \mathbf{E}_0 \, e^{-i(kz-\omega t)} \tag{2.3.18}$$

where $\mathbf{E}_0$ is the field at $z = 0$. Applying equations (2.3.16) - (2.3.17),

$$\mathbf{E} = \mathbf{E}_0 \, e^{-i\beta_{\mathrm{Re}} z} e^{-\beta_{\mathrm{Im}} z} e^{i\omega t} \, . \tag{2.3.19}$$

Equation (2.3.19) describes a plane wave that oscillates harmonically with distance traveled due to the β_{Re} term while attenuating exponentially in amplitude with distance traveled due to the β_{Im} term. The electromagnetic skin depth δ_S is defined by this attenuation factor:

$$\delta_S \equiv \frac{1}{\beta_{\mathrm{Im}}} = \left(\frac{2}{\mu\omega\sigma} \right)^{1/2} . \tag{2.3.20}$$

For $\mu = \mu_0$,

$$\delta_S \approx 500\sqrt{\rho T} \tag{2.3.21}$$

where $T = 1/f$ is the period of oscillation. Skin depth indicates the distance over which the field strength is attenuated by a factor of $1/e$ (Figure 2.1.a).

By examining skin depths for various resistivities and frequencies it is clear that diffusing harmonic fields are attenuated more rapidly with range at high frequencies, and in conductive media. The physical cause is simple: in a conductor, potential energy stored in the electric

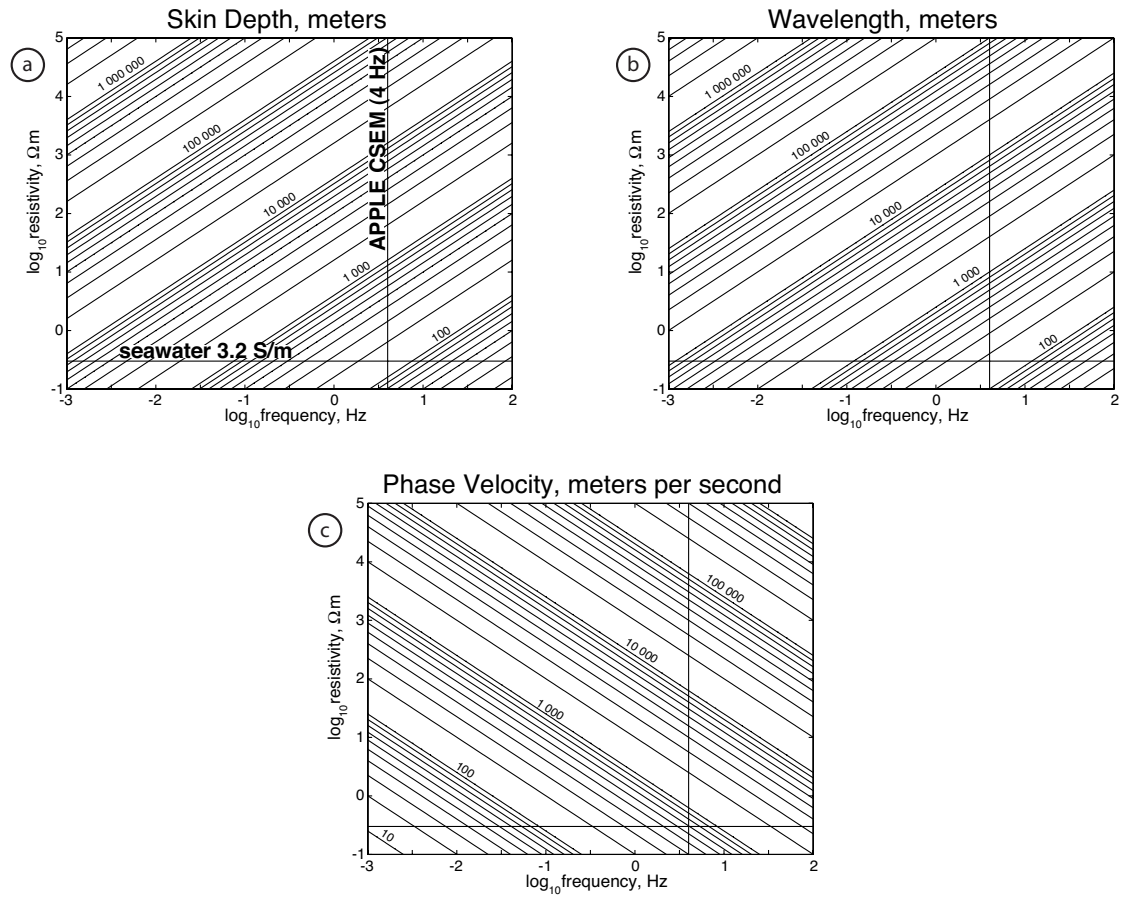

Figure 2.1 Computed from the simplified plane-wave approximation, the (a) skin depth e-folding distance δ_S is similar in scale to the (b) wavelength λ, while (c) phase velocity exhibits dispersion.

field is "used" to move charge carriers. Attenuation occurs with every oscillation, and propagation wavelength λ (Figure 2.1.b) is shorter at higher frequencies:

$$\lambda = \frac{2\pi}{\beta_{\mathrm{Re}}} = \left(\frac{\pi}{\mu\omega\sigma} \right)^{1/2} . \tag{2.3.22}$$

Phase velocity of the diffusing fields (Figure 2.1.c) is also a function of the wave number:

$$V_{ph} = f \cdot \lambda = \frac{\omega}{\beta_{\mathrm{Re}}} = \left(\frac{2\omega}{\mu\sigma} \right)^{1/2} . \tag{2.3.23}$$

This relatively simple approximation provides a useful conceptual framework for understanding the diffusion of low-frequency electromagnetic energy through earth materials. Electrically conductive materials and higher frequencies lead to shorter wavelengths and more attenuation, while resistive materials and lower frequencies result in longer wavelengths and stronger fields at distance from the source. Phase velocity, on the other hand, increases with both frequency and resistivity. For these reasons, in an ideal EM sounding experiment, field magnitude and phase are measured at multiple frequencies and locations (or source-receiver geometries, in CSEM) and used to estimate subsurface resistivity structure. Wavelength provides an estimate of the size of the secondary current loops induced in the earth by the time varying magnetic field [Y. Li, personal comm.]. In conductive materials, the phase velocity is relatively slow, and the current loops small; the opposite is true in resistive material.

2.3.2 Boundary conditions

At the boundary between regions of differing conductivities $\sigma_1 \neq \sigma_2$, Maxwell's equations (2.3.1) - (2.3.4) dictate that

$$\mathbf{J}^1_{\hat{\mathbf{n}}} = \mathbf{J}^2_{\hat{\mathbf{n}}} \quad \Rightarrow \quad \sigma_1 \mathbf{E}^1_{\hat{\mathbf{n}}} = \sigma_2 \mathbf{E}^2_{\hat{\mathbf{n}}} \tag{2.3.24}$$

$$\mathbf{E}^1_{\hat{\mathbf{t}}} = \mathbf{E}^2_{\hat{\mathbf{t}}} \quad \Rightarrow \quad \rho_1 \mathbf{J}^1_{\hat{\mathbf{t}}} = \rho_2 \mathbf{J}^2_{\hat{\mathbf{t}}} . \tag{2.3.25}$$

Vector superscripts designate region. Current flowing normal to the boundary ($\mathbf{J}_{\hat{\mathbf{n}}}$) is continuous across it, leading to a step in electric field and an accumulation of charge at the interface. $\mathbf{E}$ tangential to the boundary ($\mathbf{E}_{\hat{\mathbf{t}}}$) is continuous across it; $\mathbf{J}_{\hat{\mathbf{t}}}$ is thus discontinuous, and proportional to conductivity. Similarly, $\mathbf{B}_{\hat{\mathbf{n}}}$ and $\mathbf{H}_{\hat{\mathbf{t}}}$ are continuous across the boundary.

For all applications described in this dissertation, the assumption $\mu = \mu_0$ is made. Thus $\mathbf{B}_{\hat{\mathbf{t}}}$ and $\mathbf{H}_{\hat{\mathbf{n}}}$ may be considered continuous, as well.

2.3.3 Motivation

The magnetotelluric (MT) method was postulated independently, more or less simultaneously, by researchers in three different parts of the world [Cagniard, 1953; Kato and Kikuchi, 1950; Tikhonov, 1950]. It is a natural source EM sounding method; the source currents flow in the electrically conductive ionosphere, induced by the interaction between the earth's magnetic field and the solar wind. The magnetic field created by these currents propagates down through the highly resistive lower atmosphere and induces horizontal currents in the oceans and subsurface.

To apply the MT method, continuous measurements of the horizontal electromagnetic fields $\mathbf{E}(t)$ and $\mathbf{B}(t)$ are made at the earth's surface (and/or seafloor), and then transformed into the frequency domain. An estimate of the four-component complex impedance tensor $\mathbf{Z}(\omega)$ is computed for a range of frequencies:

$$\mathbf{E} = \mathbf{Z}\mathbf{H} \tag{2.3.26}$$

$$\begin{pmatrix} E_x \\ E_y \end{pmatrix} = \begin{pmatrix} Z_{xx} & Z_{xy} \\ Z_{yx} & Z_{yy} \end{pmatrix} \begin{pmatrix} H_x \\ H_y \end{pmatrix}. \tag{2.3.27}$$

Information about the subsurface is contained in $\mathbf{Z}(\omega)$: the local geoelectric strike, the dimensionality of the electrical conductivity structure, the bulk electrical conductivity. Processing and inversion schemes have been developed to interpret MT impedance tensor data; two key assumptions are a plane wave source field and a locally flat earth.

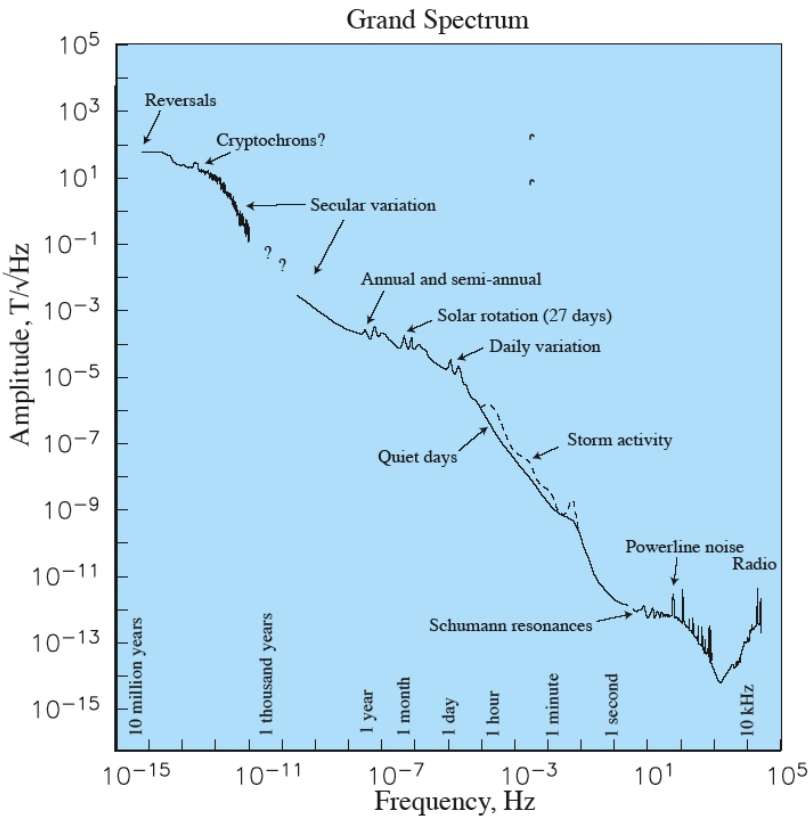

Figure 2.2 Amplitude spectrum of the ambient magnetic field at the earth's surface. [figure from Constable and Constable, 2004]

The ambient electromagnetic field at the earth's surface is relatively weak at frequencies of ~1 Hz and higher (Figure 2.2), motivating the use of an active source transmitter at these higher frequencies in land-based MT surveys [Zonge and Hughes, 1991]. The large resistivity contrast between the essentially non-conductive atmosphere and the relatively conductive earth refracts even nearby sources vertically downward into the subsurface, as dictated by Snell's Law.

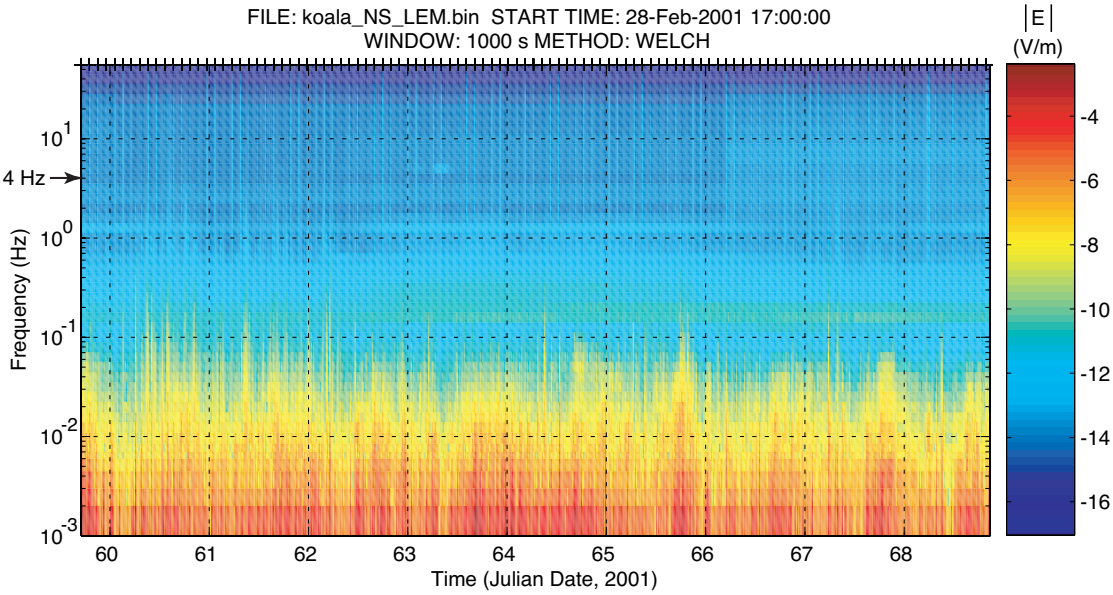

Figure 2.3 Amplitude spectrogram of the north-south component of the seafloor electric field, measured by instrument KOALA during the CSEM portion of the APPLE experiment and adjusted for the receiver transfer function. 4.4 km of electrically conductive seawater filters out exo-atmospheric sources above ~0.01 Hz, motivating the use of an active source (4 Hz for APPLE). Ticks along the top indicate logger diskwrites; these create broadband noise. Microseisms, generated by seasurface gravity waves, displace the electrodes relative to each other at ~0.2 Hz [Webb and Cox, 1986], and increased in intensity due to a period of stormy weather centered on day 64. Low-frequency MT fields exhibit diurnal variation.

In a MMT survey, MT source fields must propagate down through the electrically conductive seawater, which behaves as a low-pass filter (Figure 2.3). For typical abyssal ocean depths of 4 km, MMT source fields at frequencies greater than ~0.1 Hz are attenuated below the detection threshold of modern seafloor electromagnetic field sensors. Because the higher frequency source fields are absent, shallow subsurface conductivity properties cannot be independently determined using MMT data alone, motivating the use of an active source at

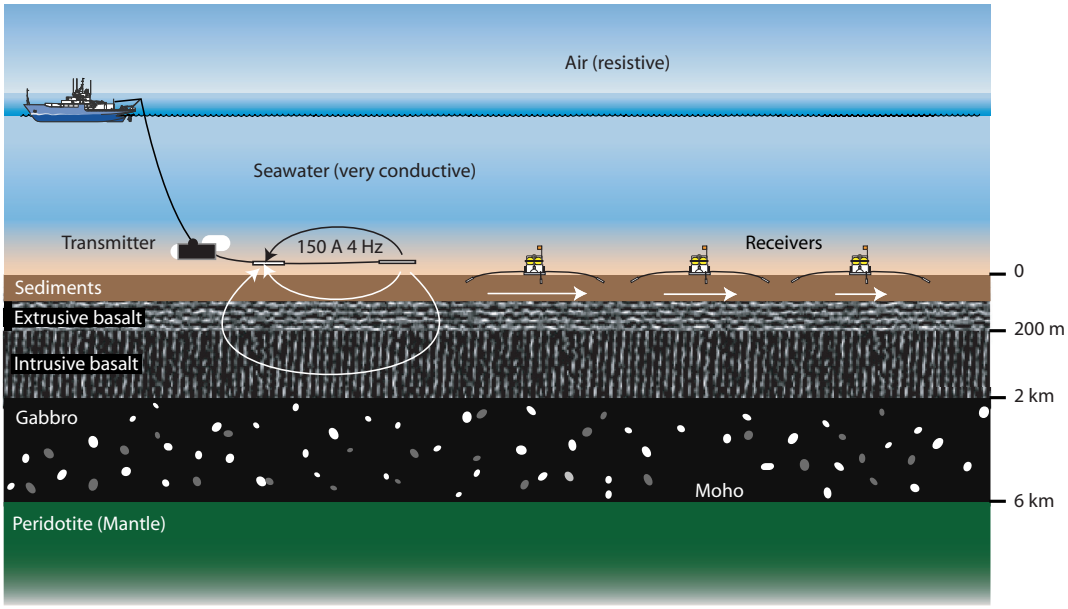

Figure 2.4 Conceptual diagram of CSEM data acquisition over mature oceanic lithosphere. The rate at which the horizontal electric field decays with distance from the transmitter is a function of lithospheric electrical conductivity. Sediment cover at the APPLE survey site was < 100 m. Layer thicknesses are approximate. (Top half of image courtesy S. Constable)

or near the seafloor. MMT data, furthermore, are subject to distortion due to galvanic bathymetric and coast effects [Heinson and Constable, 1992; Key, 2003].

A CSEM transmitter is used to generate an electromagnetic source current at the seafloor in the range $0.1 \leq f < 100$ Hz. An intrinsic advantage is that ambient noise is very weak above around 0.1 Hz, give or take a bit depending on water depth. Non-planar inductive source fields due to ocean currents moving conductive seawater through the earth's magnetic field are present [Cox, *et al.*, 1968] but typically minor at CSEM frequencies (Figure 2.3), [Chave and Luther, 1990]. Measurements in the North Pacific indicate correlation between barotropic (depth-independent) motion of the ocean and horizontal electric fields at the seafloor for $f \leq 2 \times 10^{-6}$ Hz ($T \geq 5$ days) [Luther, *et al.*, 1991].

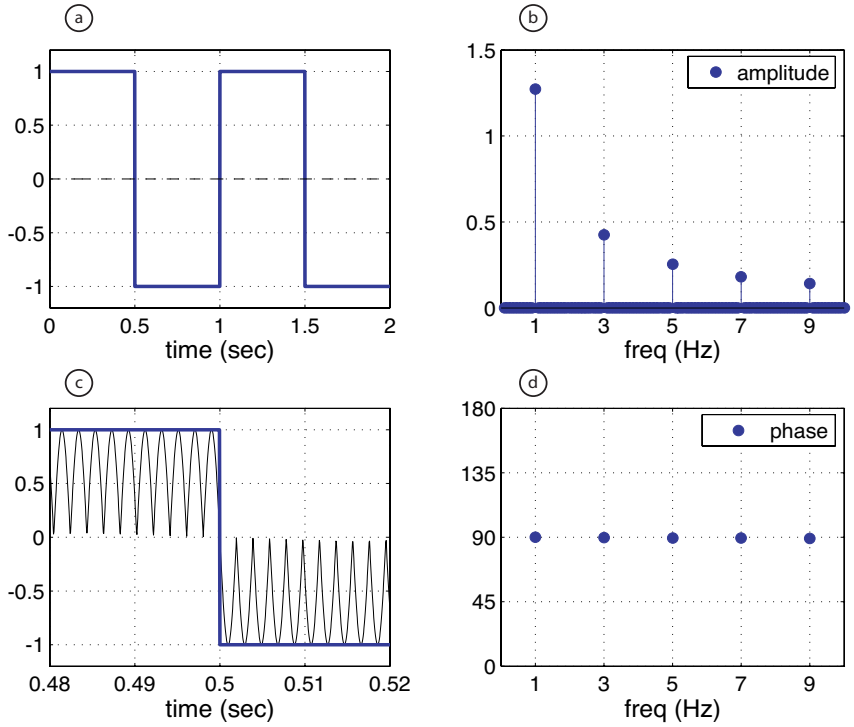

Figure 2.5 (a) Normalized idealized 1 Hz transmitter current due to (b) a fully rectified 256 Hz applied harmonic voltage with a square-wave envelope. Cosine transform of (a) into the frequency domain using sft6 (section 3.4) reveals (c,d) power at the odd harmonics of the fundamental square wave frequency.

2.3.4 Implementation

At present, CSEM data are acquired by first deploying autonomous EM field sensors (receivers) to the seafloor (section 3.3). Receiver arrays, as seen from above, may be linear, gridded, circular, asterisk-shaped, etc. depending on the target of interest. A Horizontal Electric Dipole (HED) transmitter (section 3.2) is lowered to the seafloor at the end of a winch cable, and subsequently deeptowed behind the ship (Figure 2.4). Tow paths may also take on various patterns depending on the target. After completion of the transmitter tows, the receivers are released from their anchors by remote acoustic control and recovered onto the deck of the ship once they float to the surface.

An AC voltage is applied across the dipole antenna, with seawater providing the return current path. The AC voltage typically follows a quasi-square wave (Figure 2.5, 3.8). A square wave can be decomposed into a sum of sinusoids at the odd-numbered harmonics of the fundamental square wave frequency; a square wave transmission waveform envelope thus creates energy at multiple frequencies. More elaborate waveforms have also been used to tailor the source amplitude spectrum [Constable and Cox, 1996].

Electric field time series measured by the receivers are transformed into the frequency domain at the transmission frequencies for subsequent analysis (section 3.4).

2.3.5 Modes

In CSEM parlance, the two "modes" typically discussed are the radial mode and the azimuthal mode (Figure 2.6). These names come from the solution of the horizontal electric fields in cylindrical components over a 1-D earth model (section 2.4.1).

For the isotropic 1-D case, the radial mode ($\phi = 0°, 180°$) is where the azimuthal component E_ϕ goes to zero, and the azimuthal mode ($\phi = 90°, 270°$) is where the radial component E_ρ goes to zero (see equations (2.4.15) - (2.4.16)). At intermediate azimuths, the horizontal field can be decomposed into a harmonically proportioned sum of these two components. For propagation through a material of some particular conductivity, the two components exhibit differing rates of attenuation and phase lag with increasing source-receiver offset (Figure 2.9)

This modal description loses literal meaning in the presence of anisotropic media or higher-dimensional structure, but the terms tend to be used in practice regardless. They are also sometimes called the "in-line" (radial) and "broadside" (azimuthal) components.

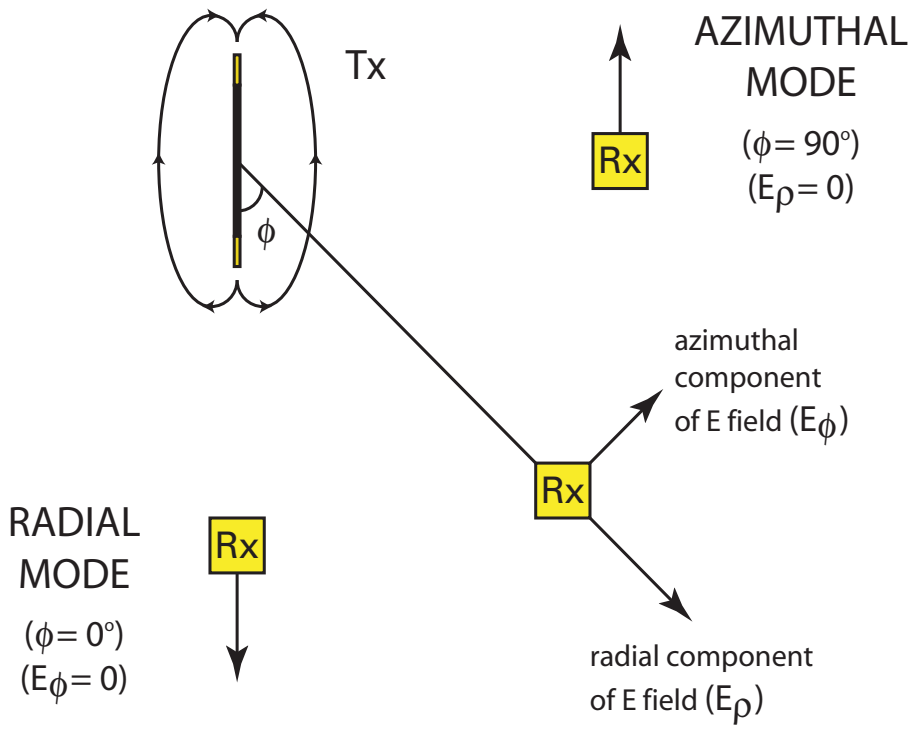

Figure 2.6 Plan view. Radial and azimuthal "modes" come from the cylindrical decomposition of section 2.4.1 and are only truly defined in the 1-D isotropic case; these terms are often applied more generally as geometric descriptors when $\phi = 0, 90, 180,$ or $270°$.

2.3.6 Polarization ellipse parameters

The horizontal electric field measured at the seafloor is rarely the result of purely radial or azimuthal source-receiver geometry. Furthermore, experimental source-receiver geometries are subject to uncertainty. CSEM data are often characterized in terms of the polarization ellipse parameters [Smith and Ward, 1974] to help address these issues.

Beginning with orthogonal coincident measurements of the complex horizontal electric field $E_1 = |E_1| e^{i\varphi_1}$ and $E_2 = |E_2| e^{i\varphi_2}$, with magnitudes $|E_1|$ and $|E_2|$ and phases φ_1 and φ_2 , the magnitudes of the major and minor axes of the polarization ellipse (Figure 2.7) are:

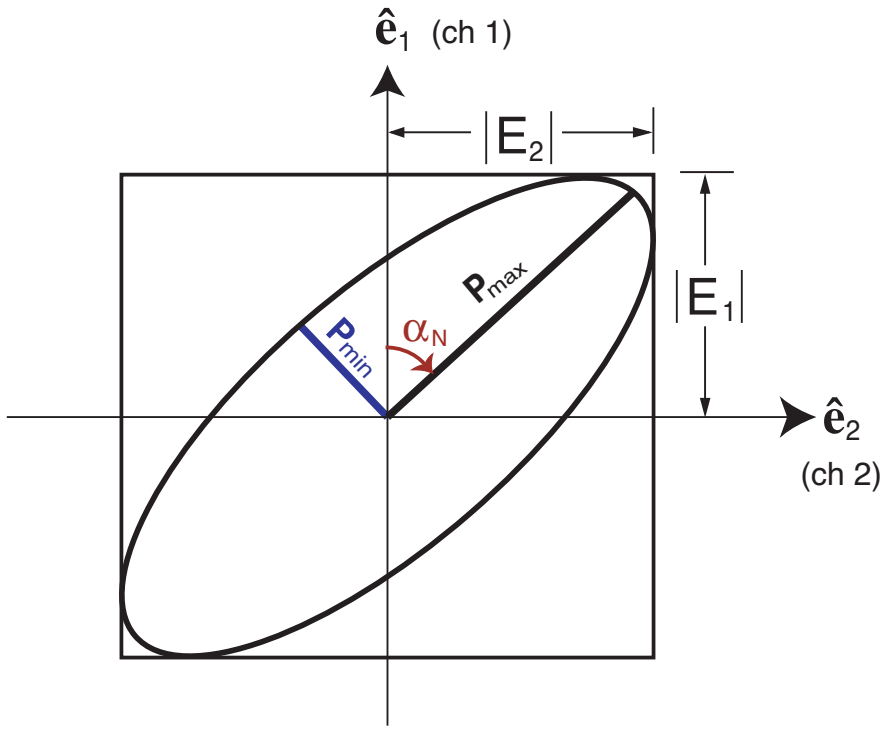

Figure 2.7 Horizontal electric field polarization ellipse parameters. In general, measured complex orthogonal components E_1, E_2 will be out of phase with each other; as a result, their phasor traces an elliptical path. APPLE CSEM data were characterized in terms of these ellipse parameters.

$$P_{MAX} = \left| |E_1| e^{i\Delta\varphi} \sin\alpha + |E_2| \cos\alpha \right| \tag{2.3.28}$$

$$P_{MIN} = \left| |E_1| e^{i\Delta\varphi} \cos\alpha - |E_2| \sin\alpha \right| \tag{2.3.29}$$

where $\Delta\varphi = \varphi_1 - \varphi_2$, with P_{MAX} oriented at a tilt angle α counterclockwise from $\hat{\mathbf{e}}_2$:

$$\tan 2\alpha = \frac{2|E_2||E_1|\cos\Delta\varphi}{|E_2|^2 - |E_1|^2}. \tag{2.3.30}$$

The angle $\alpha_N = 90° - \alpha$, positive clockwise from $\hat{\mathbf{e}}_1$ (channel 1, or instrument north) to P_{MAX}, was used to describe the APPLE data ellipse orientations.

P_{MAX} is a more robust estimate of field magnitude than either individual component when the orientation of the seafloor receiver is uncertain, which is often the case. Furthermore, α is a function of $\Delta\varphi$, so the absolute source-receiver phase need not be known (which was the situation for CSEM data collected prior to *circa* 2002, including the data set analyzed in this dissertation). P_{MAX} varies more gradually with relative transmitter azimuth than either individual component, making it less susceptible to geometric uncertainties. In addition, P_{MAX} is by definition the largest component of the field, making it least susceptible to random noise

2.4 Forward Modeling

Two algorithms were used to model CSEM data over a 1-D earth: one isotropic, the other incorporating a uniaxially anisotropic layer into an otherwise isotropic earth model. Both involve the application of numerical methods to find approximate solutions of analytic formulations, and were written in FORTRAN. Higher-dimensional modeling codes were not applicable to this data set – the geometric layout of the receiver array was not optimized for resolving 2- or 3-D conductivity structure across the survey site, nor did the single straight transmitter tow segment trend perpendicular to the geologic (and presumably geoelectric) strike.

2.4.1 1-D, isotropic

The HED CSEM 1-D isotropic modeling code used in this study was first presented by Chave and Cox [1982] and later revisited by Flosadóttir and Constable [1996]. Evans [1991] and MacGregor [1997] have explored the formulation of the solution in considerable detail.

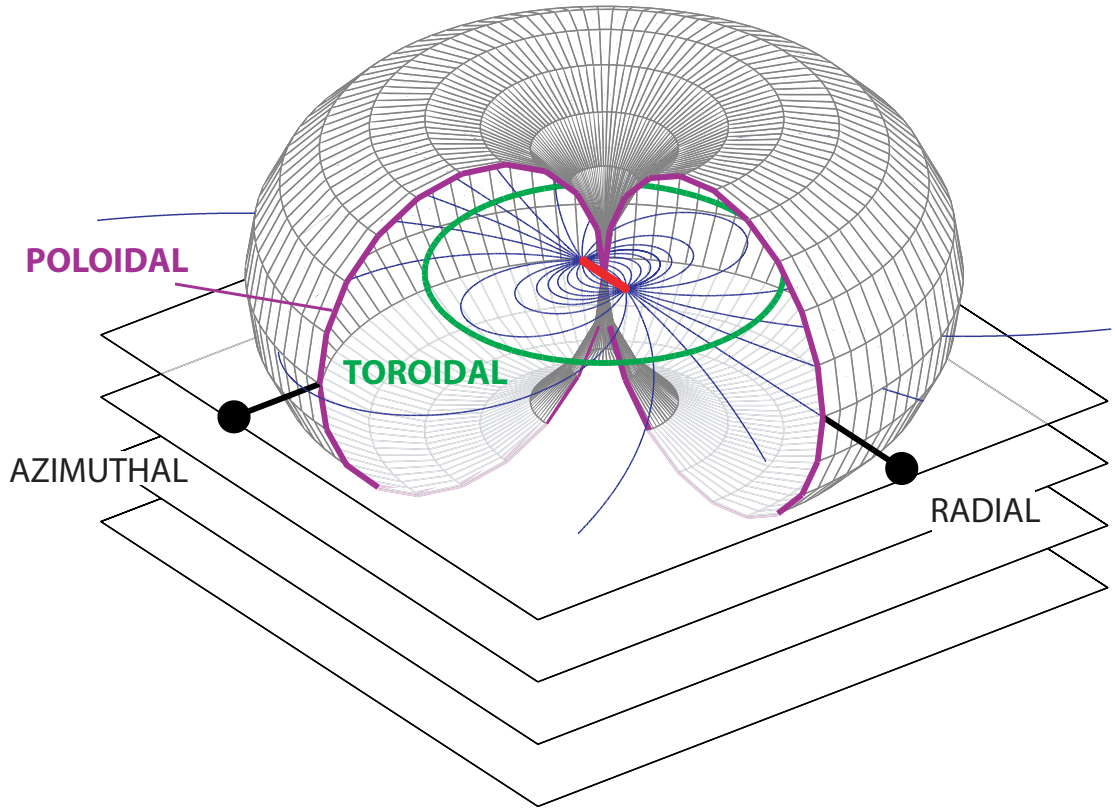

Figure 2.8 Cylindrically symmetric computation of induction in a 1-D isotropic seafloor due to a point HED source is facilitated by the decomposition of electric field **E** and magnetic flux **B** into orthogonal toroidal and poloidal modes. Static dipole current lines are drawn in blue.

In an electrically homogeneous (and thus isotropic) model, any arbitrary EM field may be decomposed into two orthogonal modes, toroidal and poloidal, which satisfy Maxwell's equations independently, and together describe the field completely. Their topological framework is a torus: poloidal currents and fluxes trace longitudinal circumferences, and toroidal, latitudinal. Toroidal **E** is coupled to poloidal **B**, and *vice versa*. The use of mathematical modes that are orthogonal loops is underpinned by the physical reality that currents and fluxes flow in closed circuits that curl around each other.

In the case of a dipole source over isotropic 1-D structure, it is useful to consider a torus with the source in the center and the pole of symmetry normal to the seafloor (Figure 2.8). Closed solutions of the fields exist in this formulation, and cylindrical symmetry allows for expedient analytical and numerical transformation between the spatial and horizontal wavenumber domains (through the use of a Fast Hankel Transform).

In a Cartesian coordinate system in which material properties vary only along $\hat{\mathbf{z}}$, any vector field **N** may be decomposed into a combination of three scalar fields ϑ, ψ, χ :

$$\mathbf{N} = \nabla\vartheta + \nabla\times(\psi\hat{\mathbf{z}}) + \nabla\times\nabla\times(\chi\hat{\mathbf{z}}). \tag{2.4.1}$$

Applying this decomposition to the source current $\mathbf{J}_S$,

$$\mathbf{J}_S = \nabla\times(\mathrm{Y}\hat{\mathbf{z}}) + \nabla\times\nabla\times(\Xi\hat{\mathbf{z}}) \tag{2.4.2}$$

and, since conductivity only varies along $\hat{\mathbf{z}}$, explicitly separating the $\hat{\mathbf{z}}$ component from the horizontal (h):

$$\mathbf{J}_S = J_S^z\hat{\mathbf{z}} + \mathbf{J}_S^h \tag{2.4.3}$$

$$\mathbf{J}_S = J_S^z\hat{\mathbf{z}} + \nabla_h\Gamma + \nabla\times\left(\mathrm{Y}\hat{\mathbf{z}}\right) \tag{2.4.4}$$

where $J_S^z = -\left(\nabla_h^2\Xi\right)$. $\Gamma = \dfrac{\partial\Xi}{\partial z}$ and Y satisfy the Poisson equations:

$$\nabla_h^2\Gamma = \nabla_h\cdot\mathbf{J}_S^h \tag{2.4.5}$$

$$\nabla_h^2\mathrm{Y} = -(\nabla_h\times\mathbf{J}_S^h)\cdot\hat{\mathbf{z}}. \tag{2.4.6}$$

The poloidal component of the source current, described in equation (2.4.4) by $J_S^z\hat{\mathbf{z}} + \nabla_h\Gamma$, provides sensitivity to vertical variations in electrical conductivity, as poloidal currents must pass directly through layer boundaries. The toroidal component of the source current, described by $\nabla\times\left(\mathrm{Y}\hat{\mathbf{z}}\right)$, is coupled to subsurface layers solely through induction – and

because subsurface toroidal currents rely on induction, they do not exist in the zero-frequency DC limit.

An HED source generates currents in both modes in this formulation, while a VED (vertical) source generates exclusively poloidal currents.

The decomposition of equation (2.4.1) is also applied to the magnetic flux induced in the subsurface by a harmonic $\mathbf{J}_S$:

$$\mathbf{B} = \nabla \times \left(\Pi \hat{\mathbf{z}}\right) + \nabla \times \nabla \times \left(\Psi \hat{\mathbf{z}}\right) \tag{2.4.7}$$

where Π represents the toroidal magnetic mode (coupled to poloidal **E**) and Ψ represents the poloidal magnetic mode (coupled to toroidal **E**).

Inserting equations (2.4.4) and (2.4.7) into Maxwell's equations (2.3.1)-(2.3.4) allows **E** to be expressed in terms of these modal scalar potentials:

$$\mathbf{E} = \frac{1}{\mu_0 \sigma} \nabla \times \nabla \times \left(\Pi \hat{\mathbf{z}}\right) - \frac{1}{\sigma}\left(\mathbf{J}_S^z \hat{\mathbf{z}} + \nabla_h \Gamma\right) - i\omega \nabla \times \left(\Psi \hat{\mathbf{z}}\right) \tag{2.4.8}$$

and the scalar potentials as a pair of differential equations

$$\nabla^2 \Psi - i\omega\mu_0\sigma\Psi = -\mu_0 \mathrm{Y} \tag{2.4.9}$$

$$\nabla_h^2 \Pi + \sigma \partial_z \left(\frac{\partial_z \Pi}{\sigma}\right) - i\omega\mu_0\sigma\Pi = -\mu_0 \mathbf{J}_S^z + \mu_0 \sigma \partial_z \left(\frac{\Gamma}{\sigma}\right) \tag{2.4.10}$$

which are subsequently converted into the horizontal wavenumber domain

$$\hat{\Pi}, \hat{\Psi}, \hat{\Gamma}, \hat{\mathrm{Y}}, \hat{\mathbf{J}}_S^z \left(k_x, k_y, z\right)$$

via the Hankel transform

$$\hat{f}(k,z) = \int_0^\infty J_0(kr)\, r\, f(r,z)\, dr$$
$$f(r,z) = \int_0^\infty J_0(kr)\, k\, \hat{f}(k,z)\, dk$$

where $J_N(kr)$ is the Bessel function of order N, k is the horizontal wavenumber, and $r = \sqrt{x^2 + y^2}$. Bessel functions are differential equation solutions that are finite at the origin and decay exponentially with distance as they oscillate, making them useful for calculating the propagation of diffusive EM waves in cylindrical coordinates. The Hankel transform is formally equivalent to a double Fourier transform:

$$\hat{A}(k_x, k_y) = \iint e^{i(k_x x + k_y y)} A(x, y)\, dx\, dy$$
$$A(x, y) = \iint e^{-i(k_x x + k_y y)} \hat{A}(k_x, k_y)\, dk_x\, dk_y$$

An improved Hankel transform algorithm [Anderson, 1989] was incorporated into the code of Chave and Cox [1982] by Flosadóttir and Constable [1996].

The dipole length is considered infinitesimal: for a HED at altitude z' above the seafloor,

$$\mathbf{J}_S = p\, \delta(x)\, \delta(y)\, \delta(z - z')\, \hat{\mathbf{x}} \tag{2.4.11}$$

where p is the source dipole moment. This is a valid approximation at ranges greater than a few actual dipole lengths, and allows the Green's function method to be used to solve the transformed differential equations for the scalar potentials while making use of the boundary conditions of section 2.3.2. The Green's functions describe the propagation of the source field through the model, and contain diffusive "reflection coefficients" R_{TM} and R_{PM} that scale the secondary fields which emanate from, respectively, the boundaries between the various layers in the poloidal current case (toroidal magnetic TM induction), and from the layers themselves in the toroidal current case (poloidal magnetic PM induction):

$$R_{TM} = \frac{\mathrm{K}\beta_w - \sigma_w}{\mathrm{K}\beta_w + \sigma_w} \tag{2.4.12}$$

$$R_{PM} = \frac{\Lambda\beta_w - 1}{\Lambda\beta_w + 1}. \tag{2.4.13}$$

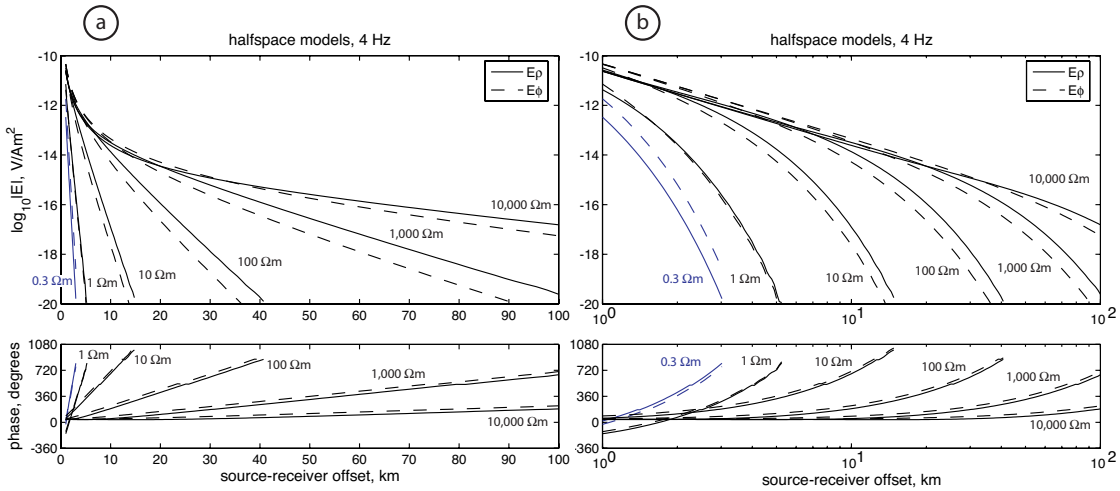

Figure 2.9 Amplitudes and phases of E_ρ, E_ϕ over isotropic halfspace resistivity models at 4 Hz, for a unit dipole moment. (a) Phase increases linearly while (b) amplitude decays exponentially, approaching the dipole-in-vacuum rate of $1/r^3$ as the underlying halfspace resistivity grows large.

In seawater of conductivity σ_w wave propagation is a function of $\beta_w \equiv \sqrt{k^2 - i\omega\mu_0\sigma_w}$. The response functions

$$\mathrm{K} = \left.\frac{\sigma_w \Pi}{\partial_z \Pi}\right|_{z=0} \qquad \Lambda = \left.\frac{\Psi}{\partial_z \Psi}\right|_{z=0} \tag{2.4.14}$$

contain all the information about the conductivity structure and are computed using recursion through the model.

The source function equation (2.4.11) is incorporated into the Poisson equations (2.4.5) - (2.4.6) to characterize Γ and Υ in terms of $\mathbf{J}_S$, and the Hankel transform is applied.

The seafloor EM field is computed through substitution back into equations (2.4.7) and (2.4.8) after inverse Hankel transform is applied to the modal scalars. The radial, azimuthal, and vertical components of **E** in a transmitter-centered cylindrical coordinate system are:

$$E_\rho = \frac{p\cos\phi}{4\pi\sigma_w}\left[\int_0^\infty dk\left(I(kr)\beta_w R_{TM} - \frac{i\omega\mu_0\sigma_w}{\beta_w r}J_1(kr)R_{PM}\right)e^{-\beta_w(z+z')} - \int_0^\infty dk\left(J_0(kr)k\beta_w - \frac{k^2}{\beta_w r}J_1(kr)\right)e^{-\beta_w|z-z'|}\right] \tag{2.4.15}$$

$$E_\phi = -\frac{p\sin\phi}{4\pi\sigma_w}\left[\int_0^\infty dk\left(\frac{\beta_w}{r}J_1(kr)R_{TM} - \frac{i\omega\mu_0\sigma_w}{\beta_w}I(kr)R_{PM}\right)e^{-\beta_w(z+z')} - \int_0^\infty dk\left(\frac{ik\omega\mu_0\sigma_w}{\beta_w^2}J_0(kr) - \frac{k^2}{\beta_w r}J_1(kr)\right)e^{-\beta_w|z-z'|}\right] \tag{2.4.16}$$

$$E_z = -\frac{p\cos\phi}{4\pi\sigma_w}\int_0^\infty dk\, J_1(kr)k^2\left(R_{TM}\, e^{-\beta_w(z+z')} \mp e^{-\beta_w|z-z'|}\right) \tag{2.4.17}$$

where $I(kr) \equiv \left(kJ_0(kr) - \frac{J_1(kr)}{r}\right)$, z is the receiver altitude (normally 0) and z' the transmitter height. Components of **B** can be similarly computed. The radial component is usually denoted E_ρ, even though r has been representing radial distance in this discussion to avoid confusion with resistivity.

The first term in brackets in equations (2.4.15) - (2.4.17) represents the EM field scattered by the surrounding conductivity structure, while the second term denotes the primary field traveling through a wholespace of σ_w.

All azimuthal dependence is contained in the coefficient in front of the brackets. The relative contributions of the components vary harmonically with azimuth around the dipole. E_ρ and E_ϕ diffuse differently (Figure 2.9) and combine at $\phi \neq 0, 90, 180, 270°$ to generate elliptically polarized horizontal electric fields at the seafloor (Figure 2.10, Figure 2.11). It is noteworthy that both E_ρ and E_ϕ contain contributions from both toroidal and poloidal modes.

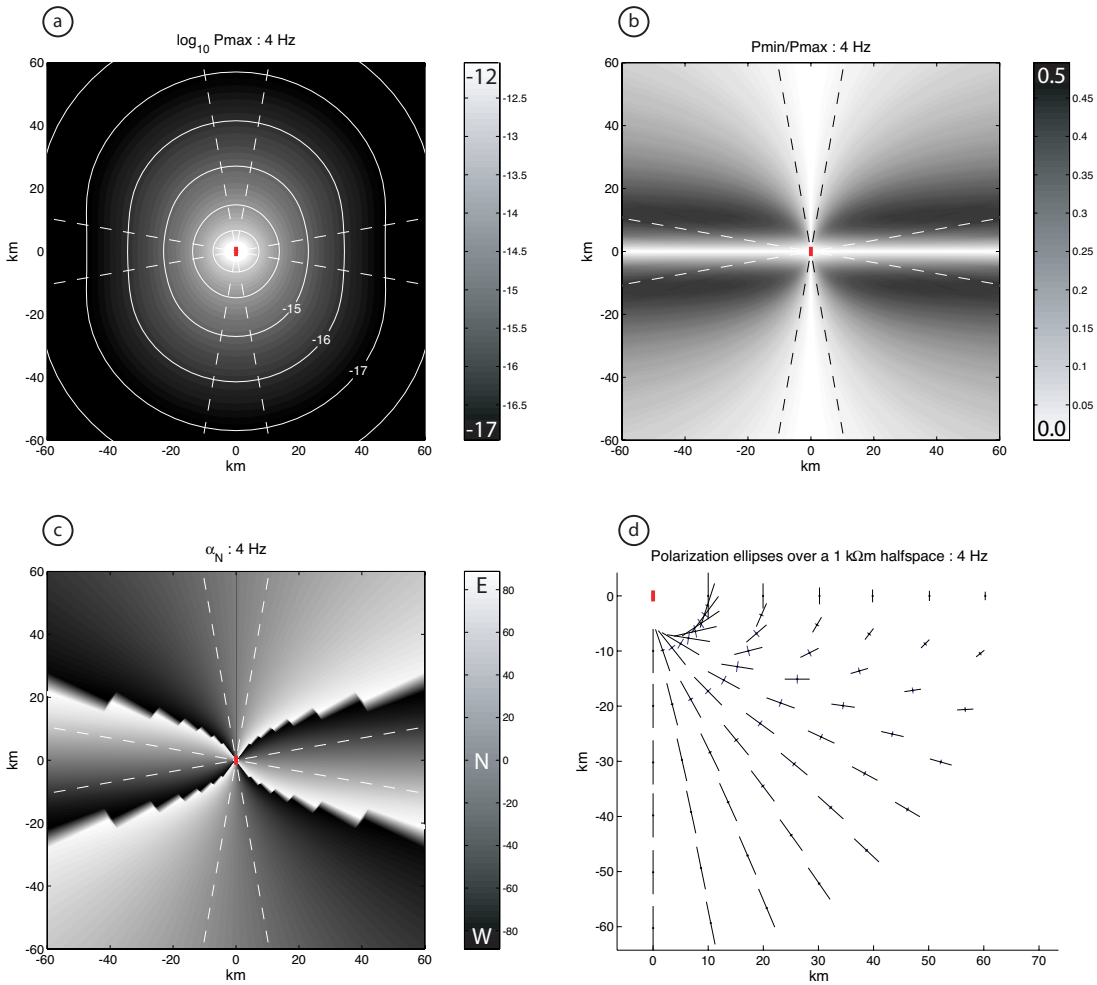

Figure 2.10 The horizontal electric field polarization ellipse parameters at the seafloor over a 1,000 Ωm halfspace: (a) field intensity P_{MAX}; (b) ellipse eccentricity P_{MIN} / P_{MAX}; (c) ellipse orientation α_N, which wraps at $\pm 90°$. Water depth is 4400 m, transmitter height is 100 m above the seafloor, and point unit HED is oriented north/south. Wedges indicate $\pm 10°$ from pure radial and azimuthal modes. (d) Ellipse axes at several azimuths; normalized within each radius to its radial mode magnitude.

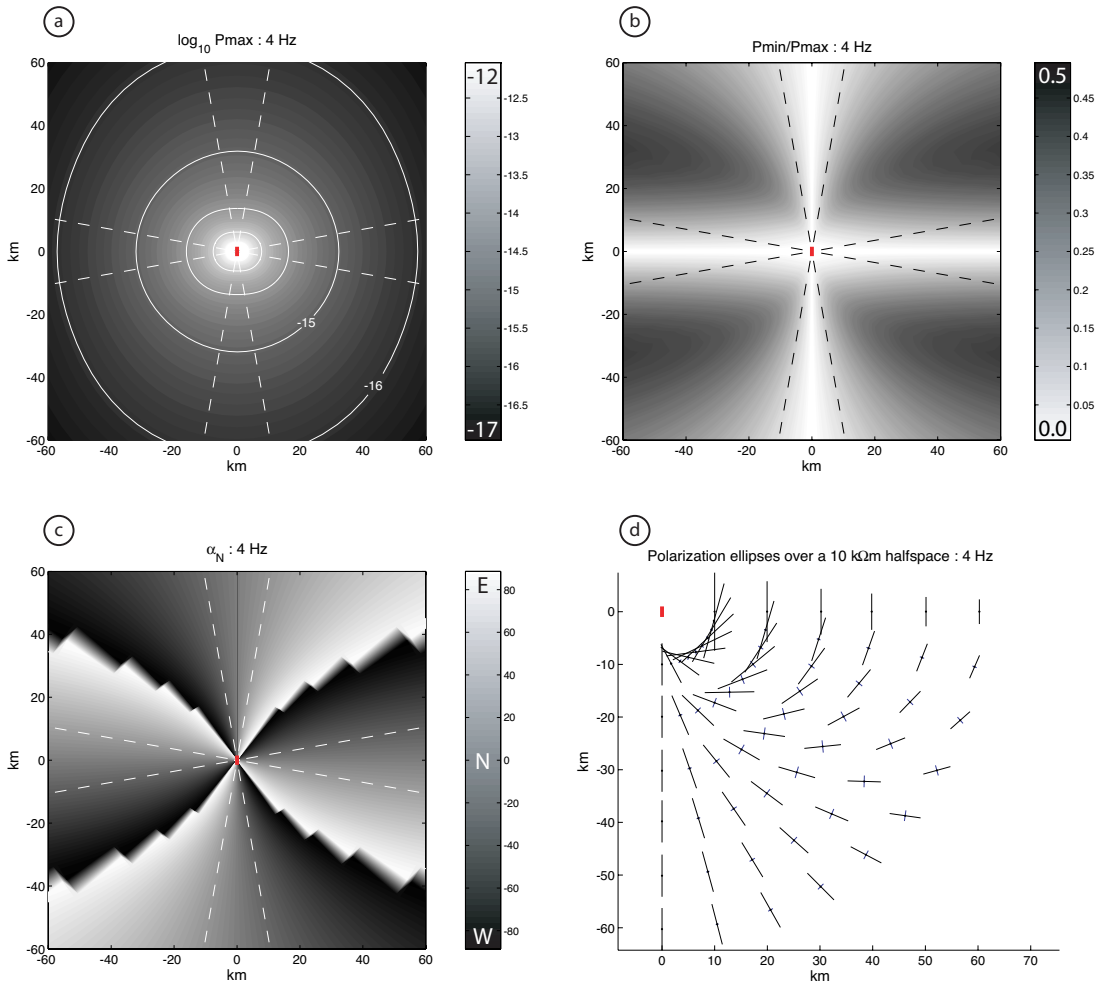

Figure 2.11 Same as Figure 2.10, but over a 10,000 Ωm halfspace.

2.4.2 1-D, anisotropic

The uniaxial electrically anisotropic forward modeling codes used in this study are based on the double half-space formulation of Yu and Edwards [1992], where the transmitter and receivers were assumed to be aligned with the principal axes of the conductivity tensor. To analyze the PEGASUS CSEM data, Everett and Constable [1999] computed the response of a transmitter aligned oblique to the anisotropic strike. For this analysis of the APPLE CSEM data, Everett, *et al.* [in preparation] compute the response of a three-layer 1-D subsurface, with a uniaxially anisotropic layer sandwiched between an isotropic top layer and basal halfspace. The seawater is modeled as a uniform halfspace, i.e. infinitely deep. Due to the great depth of the ocean at the APPLE survey site (4.4 km), high lithospheric resistivities, and relatively high sounding frequency of 4Hz, the effect of finite water depth on the data is insignificant, and can be safely neglected for the sake of analytic convenience and numerical efficiency.

Mark Everett wrote the code and ran a forward modeling study. The author of this dissertation assisted in the model studies and adapted the code for subsequent Marquardt inversion (section 2.5.1), under the supervision of Steven Constable.

In brief, the horizontal fields are solved component-wise along the primary axes of the anisotropy, x and y. They are decomposed into up- and down-going diffusive terms, and the coefficients for the fields are solved in the horizontal wavenumber domain by application of boundary conditions and source terms. For the case of an obliquely oriented transmitter, the fields are computed for virtual transmitters aligned along both x and y, and a harmonically scaled vector sum is found. Finally, the fields are transformed into the spatial domain via double Fourier transform.

Closed analytic solutions to the toroidal formulation of section 2.4.1 exist only in the 1-D isotropic case, so forward models of electrically anisotropic media cannot utilize the numerical

efficiency of a Fast Hankel Transform. Instead, the horizontal electric field components $\hat{E}_x, \hat{E}_y$ are computed in the 2-D horizontal wavenumber domain (k_x, k_y, z) and then converted into E_x, E_y in the spatial domain (x, y, z) via a double Fourier transform:

$$\hat{A}(k_x, k_y) = \iint e^{i(k_x x + k_y y)} A(x, y)\, dx\, dy$$
$$A(x, y) = \iint e^{-i(k_x x + k_y y)} \hat{A}(k_x, k_y)\, dk_x\, dk_y.$$

Up until now, the scalar conductivity σ has been assumed to be independent of orientation. In an anisotropic medium, however, a diagonal matrix is used to represent the vector conductivity $\boldsymbol{\sigma}$:

$$\boldsymbol{\sigma} = \begin{pmatrix} \sigma_x & & \\ & \sigma_y & \\ & & \sigma_z \end{pmatrix}. \tag{2.4.18}$$

In the isotropic case $\sigma_x = \sigma_y = \sigma_z$. In a uniaxially anisotropic medium, two of the tensor components share the same conductivity $\sigma_{\parallel}$, with $\sigma_{\perp}$ perpendicular to them (Figure 2.12). When $\sigma_{\parallel} > \sigma_{\perp}$, "sheets" of increased conductivity within a more resistive medium are being modeled; when $\sigma_{\perp} > \sigma_{\parallel}$, "rods" of increased conductivity. The anisotropic strike is defined as the horizontal direction where the horizontal and vertical conductivities are the same. Anisotropic strike is not necessarily equivalent to geologic strike.

The anisotropic medium may be characterized by the geometric mean conductivity

$$\sigma_m \equiv \sqrt{\sigma_{\parallel} \sigma_{\perp}} \tag{2.4.19}$$

and ratio of anisotropy

$$f_a \equiv \frac{\sigma_{\perp}}{\sigma_{\parallel}}. \tag{2.4.20}$$

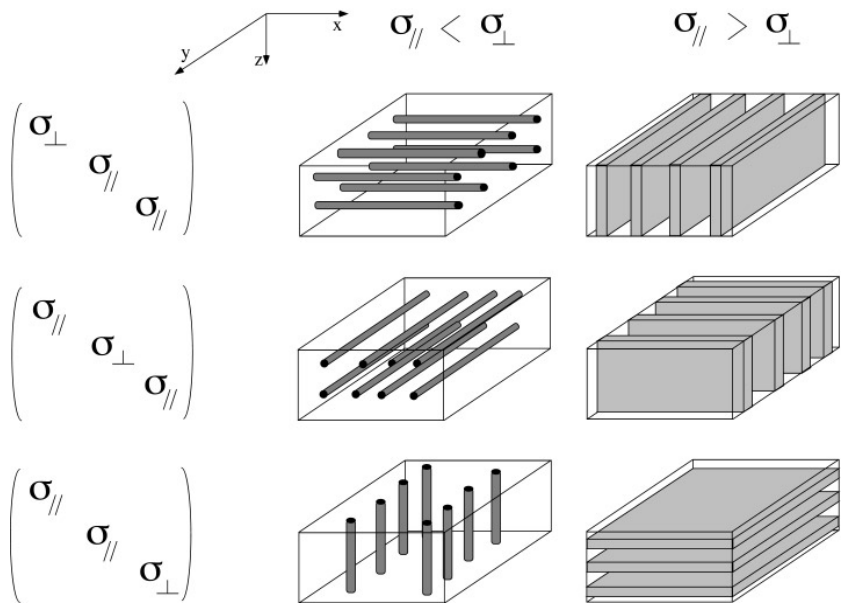

Figure 2.12 A uniaxially anisotropic model layer can simulate "rods" or "sheets" of increased conductivity within a more resistive medium. The anisotropic strike is defined as the horizontal direction that has the same resistivity as the vertical (applicable only to the first two tensors). [figure from Everett and Constable, 1999]

For the uniaxial case of $\sigma_x = \sigma_\perp$, the across-strike component E_x within the anisotropic layer obeys the partial differential form of equation (2.3.13):

$$-\frac{\sigma_\perp}{\sigma_\parallel}\frac{\partial^2 E_x}{\partial x^2} - \frac{\partial^2 E_y}{\partial y^2} - \frac{\partial^2 E_z}{\partial z^2} + i\omega\mu_0\sigma_\perp E_x = 0\,. \tag{2.4.21}$$

Upon applying a double Fourier transform, this becomes an ordinary differential equation in the horizontal wavenumber domain:

$$\frac{d^2\hat{E}_x}{dz^2} - \beta_\perp^2\hat{E}_x = 0 \tag{2.4.22}$$

where

$$\beta_{\perp} \equiv \sqrt{\left(\frac{\sigma_{\perp}}{\sigma_{\parallel}}\right) k_x^2 + k_y^2 + i\omega\mu_0\sigma_{\perp}} \ .$$

The magnetic field component can be similarly derived:

$$\frac{d^2 \hat{B}_x}{dz^2} - \beta_{\parallel}^2 \hat{B}_x = 0 \tag{2.4.23}$$

where

$$\beta_{\parallel} \equiv \sqrt{k_x^2 + k_y^2 + i\omega\mu_0\sigma_{\parallel}} \ .$$

A subset of the APPLE data was modeled by computing the response of a three-layer subsurface model, with an anisotropic layer between an isotropic upper layer and basement. In the isotropic model layers, equations (2.4.22) and (2.4.23) are valid, but with

$$\beta_n \equiv \sqrt{k_x^2 + k_y^2 + i\omega\mu_0\sigma_n}$$

where the subscript $n = 0$ denotes the seawater, $n = 1$ the top layer, and $n = 3$ the basal halfspace.

In each layer of the model, the EM field is decomposed into up- and down-going diffusive terms. Between the transmitter and the seafloor,

$$\hat{E}_x^0 = \Gamma_E \, e^{-\beta_0 z} + A \, e^{\beta_0 z} \tag{2.4.24}$$

$$\hat{B}_x^0 = \Gamma_B \, e^{-\beta_0 z} + B \, e^{\beta_0 z} \ . \tag{2.4.25}$$

The known source terms Γ_E, Γ_B scale the down-going fields, while the up-going coefficients A, B are a function of the subsurface conductivity. In the top layer,

$$\hat{E}_x^1 = C \, e^{-\beta_1 z} + D \, e^{\beta_1 z} \tag{2.4.26}$$

$$\hat{B}_x^1 = E\, e^{-\beta_1 z} + F\, e^{\beta_1 z}\,. \tag{2.4.27}$$

In the anisotropic layer, the fields vary differently with z:

$$\hat{E}_x^2 = G\, e^{-\beta_\perp z} + H\, e^{\beta_\perp z} \tag{2.4.28}$$

$$\hat{B}_x^2 = I\, e^{-\beta_\parallel z} + J\, e^{\beta_\parallel z}\,. \tag{2.4.29}$$

In the underlying basement halfspace, there is no up-going component:

$$\hat{E}_x^3 = K\, e^{-\beta_3 z} \tag{2.4.30}$$

$$\hat{B}_x^3 = L\, e^{-\beta_3 z}\,. \tag{2.4.31}$$

In each layer, the y-component (aligned with the electrical strike) is a function of the x-component. In the isotropic layers,

$$\hat{E}_y^n = \frac{k_x k_y \hat{E}_x + i\omega\partial_z \hat{B}_x}{\tau_n^2} \tag{2.4.32}$$

$$\hat{B}_y^n = \frac{-\mu_0\sigma_n \partial_z \hat{E}_x + k_x k_y \hat{B}_x}{\tau_n^2} \tag{2.4.33}$$

while in the anisotropic layer (n=2),

$$\hat{E}_y^{n=2} = \frac{k_x k_y \hat{E}_x + i\omega\partial_z \hat{B}_x}{\tau_\parallel^2} \tag{2.4.34}$$

$$\hat{B}_y^{n=2} = \frac{-\mu_0\sigma_\parallel \partial_z \hat{E}_x + k_x k_y \hat{B}_x}{\tau_\parallel^2} \tag{2.4.35}$$

where $\tau_n \equiv \sqrt{k_x^2 + i\omega\mu_0\sigma_n}$ and $\tau_\parallel \equiv \sqrt{k_x^2 + i\omega\mu_0\sigma_\parallel}$.

Applying the boundary conditions of section 2.3.2 yields 12 linear complex equations for the 12 coefficients A-L, which are solved using the LAPACK routine **dgesv**.

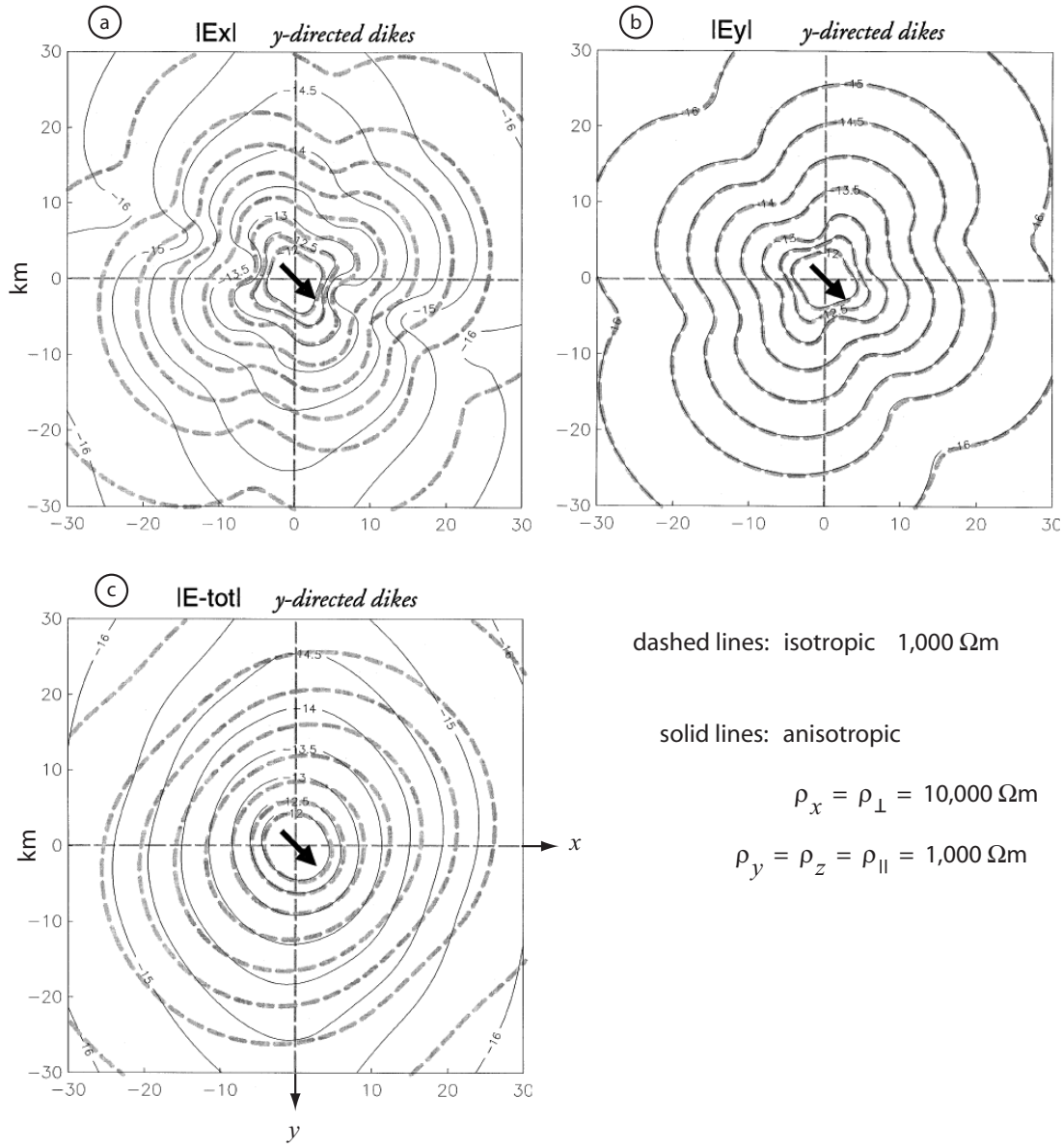

Figure 2.13 Log spaced contours of electric field magnitudes over two halfspace models, one isotropic and the other anisotropic representing y-directed vertical sheets of increased conductivity with $f_a = 10$ and $\sigma_m = 3.16 \times 10^{-3}$ S/m. The transmitter is oriented at 45° to the anisotropic axes. Both models predict the same field strength parallel to the anisotropic strike; this is a robust feature of uniaxial anisotropy. [adapted from Everett and Constable, 1999]

The source terms Γ_E, Γ_B are wavenumber domain solutions for a HED in a wholespace of seawater conductivity $\sigma_0 = \sigma_w$. For an *x*-directed HED of moment *p* at height *h* above the seafloor,

$$\Gamma_E = -\frac{\tau_0^2 p}{2\sigma_0 \beta_0} e^{-\beta_0 h} \tag{2.4.36}$$

$$\Gamma_B = 0 . \tag{2.4.37}$$

For a *y*-directed HED,

$$\Gamma_E = -\frac{k_x k_y p}{2\sigma_0 \beta_0} e^{-\beta_0 h} \tag{2.4.38}$$

$$\Gamma_B = -\frac{\mu_0 p}{2} e^{-\beta_0 h} . \tag{2.4.39}$$

Once all 12 coefficients have been computed for a given conductivity model, the horizontal electric fields at the seafloor are found by solving equations (2.4.24), (2.4.25), and (2.4.32) for $n = 0,\ z = 0$:

$$\hat{E}_x\left(k_x, k_y, z = 0\right) = \Gamma_E + A \tag{2.4.40}$$

$$\hat{E}_y\left(k_x, k_y, z = 0\right) = \frac{k_x k_y \left(\Gamma_E + A\right) - i\omega\beta_0 \left(\Gamma_B - B\right)}{\tau_0^2} . \tag{2.4.41}$$

Equations (2.4.40) and (2.4.41) describe the field for hypothetical transmitters aligned parallel or perpendicular to the uniaxial anisotropic strike. For the case of a transmitter oriented at some angle θ_T with respect to the strike of anisotropy *y*, the model response is a geometric mix of the *x*- and *y*-directed transmitter responses:

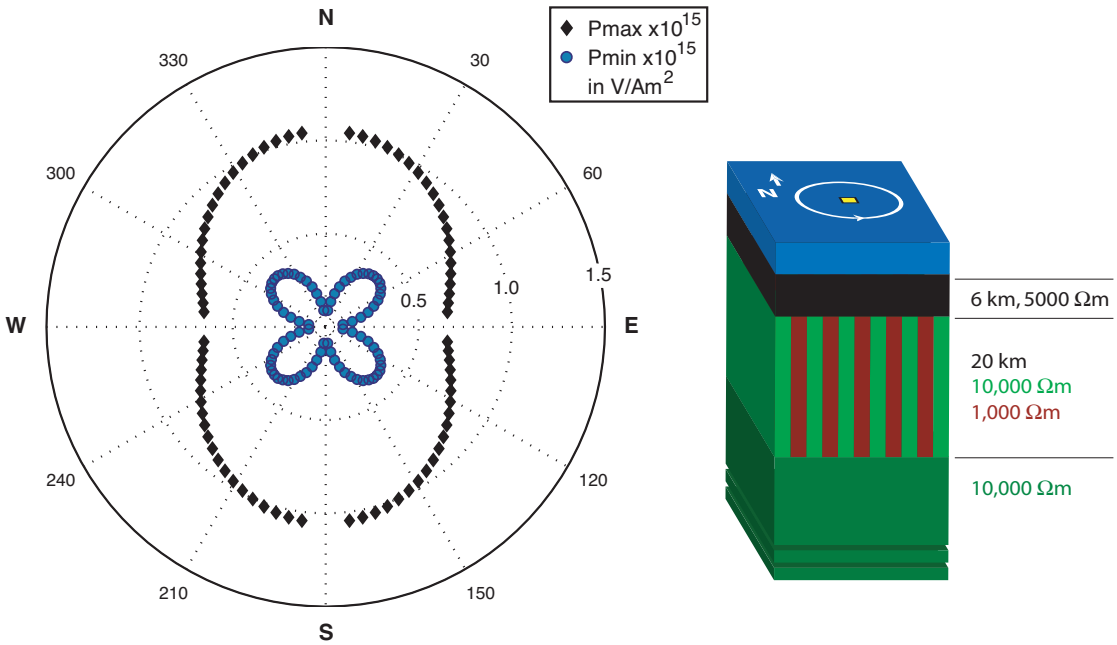

Figure 2.14 P_{MAX} and P_{MIN} computed at the center of a 30 km radius circular transmitter tow over a hypothetical three-layer lithosphere model: 6 km of isotropic crust; 20 km of anisotropic upper mantle with north/south trending vertical sheets of increased conductivity ($f_a = 0.1$); isotropic halfspace basement. Transmitter height is 100 m. The geometry is purely azimuthal mode; thus, over an isotropic seafloor, P_{MAX} would be independent of azimuth and P_{MIN} exactly zero.

$$\hat{E}_x^{\theta_T} = \hat{E}_x^X \cos\theta_T + \hat{E}_x^Y \sin\theta_T \tag{2.4.42}$$

$$\hat{E}_y^{\theta_T} = \hat{E}_y^X \cos\theta_T + \hat{E}_y^Y \sin\theta_T \tag{2.4.43}$$

where the superscript indicates transmitter orientation. In the final step, the fields are converted into the spatial domain via double Fourier transform.

For fixed source-receiver geometry, varying θ_T produces patterns in the seafloor horizontal electric field polarization ellipse parameters that are indicative of anisotropic

subsurface conductivity (Figure 2.14). Regardless of the transmitter orientation, the electric field component aligned parallel to the anisotropic strike is identical to that predicted by the isotropic model with $\sigma_{\parallel}$ as the layer conductivity [Everett and Constable, 1999] (Figure 2.13).

2.5 Inversion Methods

Forward computations of seafloor electromagnetic fields are non-linear. Furthermore, electromagnetic sounding data are noisy and incomplete: any realistic data set is satisfied by an infinite number of conductivity models. Regardless, a preferred model (or set of models) is desired for interpretation of the data. *Regularization* is the application of additional constraints to find particular solutions to non-unique problems.

Two different inversion methods, *Marquardt* and *Occam*, were used to invert subsets of the APPLE CSEM data. Both were written in FORTRAN. Marquardt is a parameter-fitting method that employs a biased estimator to find the minimum misfit model nearest to a particular initial guess, regularized in this study through coarse parameterization of the model. Occam is a regularized method used to find the minimum roughness model for a given misfit tolerance. The Marquardt method was also used to invert acoustic navigation data to estimate the deployed locations of several seafloor receivers (section 3.3.1). A review of inversion concepts and methods for DC resistivity soundings has been presented by Narayan, *et al.* [1994]; their example is loosely followed here.

A forward modeling algorithm **F** produces a set of N synthetic data **d** that would be measured over an earth modeled with M variable parameters **p** (*i.e.* layer resistivities) and some number of fixed model parameters **x** (*i.e*. layer thicknesses, source-receiver geometries):

$$\mathbf{d} = \mathbf{F}[\mathbf{p}, \mathbf{x}] . \tag{2.5.1}$$

In general, the goal of a least-squares inversion method is to find a vector $\mathbf{p}^*$ that minimizes the weighted squared misfit X^2 of the predicted data **d** to the real data $\mathbf{d}^*$, which are uncertain with standard deviations s_i:

$$X^2 = \sum_{i=1}^{N} \frac{\left(d_i - d_i^*\right)^2}{s_i^2} . \tag{2.5.2}$$

In the case of zero-mean Gaussian data uncertainty that is uniform across the data set and independent for each variable, X^2 is distributed as χ^2. In reality, CSEM data (at sufficiently large transmitter-receiver offsets to overcome systematic navigational uncertainties) follows all but the uniformity condition, motivating the use of a diagonal $N \times N$ weighting matrix **W** that contains the reciprocal standard deviations:

$$\mathbf{W} = \begin{bmatrix} 1/s_1 & & & 0 \\ & 1/s_2 & & \\ & & \ddots & \\ 0 & & & 1/s_N \end{bmatrix} . \tag{2.5.3}$$

The data misfit is also often described in terms of the Root-Mean-Squared (RMS) value:

$$\mathrm{RMS} \equiv \sqrt{\frac{X^2}{N}} . \tag{2.5.4}$$

When data misfit is equal to data uncertainty, the expectation value of X^2 is *N*. An RMS value of 1.0, therefore, is usually the desired misfit.

The goal of regularized inversion is more complicated – a functional is minimized that weighs data misfit against some other aspect of **p**, such as model "roughness", or distance from some set of parameters which apply a particular bias to the model.

2.5.1 Marquardt inversion

The ridge regression method formulated by Marquardt [1963; 1970] is an established and stable technique for the inversion of electromagnetic sounding data [*e.g.*, Inman, 1975; Petrick*, et al.*, 1977]. The Marquardt inversion code used in this work was originally written by Steven Constable based on the algorithm of Bevington [1969]. The author of this dissertation adapted the code for use with the anisotropic forward modeling code of section 2.4.2.

In component form, the Taylor expansion of **F** about an initial vector of variable parameters $\mathbf{p}^0$ is

$$d_i = F_i[\mathbf{p},\mathbf{x}] \qquad i = 1,N \tag{2.5.5}$$

$$d_i = F_i[\mathbf{p}^0,\mathbf{x}] + \left(F_i'[\mathbf{p}^0,\mathbf{x}]\right)\left(\mathbf{p}-\mathbf{p}^0\right) + \tilde{\varepsilon} \tag{2.5.6}$$

$$d_i = d_i^0 + \sum_{j=1}^{M} \frac{\partial F_i}{\partial p_j}\delta p_j + \tilde{\varepsilon}\,. \tag{2.5.7}$$

When **F** is linear, the higher-order terms $\tilde{\varepsilon}$ are exactly zero. When **F** is nonlinear, as in the case of CSEM sounding, a local linear approximation can be made by simply neglecting $\tilde{\varepsilon}$. The linear, matrix form of equation (2.5.7) is

$$\delta\mathbf{d} = \mathbf{A}\,\delta\mathbf{p} \tag{2.5.8}$$

where $\delta\mathbf{d} = \mathbf{d} - \mathbf{d}^0$ results from a step in parameters $\delta\mathbf{p} = \mathbf{p} - \mathbf{p}^0$. The $N \times M$ matrix operator **A** is the *Jacobian*, the gradient of **F** with respect to **p** at $\mathbf{p}^0$:

$$\mathbf{A} = \nabla_{\mathbf{p}}\mathbf{F}[\mathbf{p}^0,\mathbf{x}]\,. \tag{2.5.9}$$

In component form,

$$A_{ij} \equiv \frac{\partial F_i[\mathbf{p}^0, \mathbf{x}]}{\partial p_j} . \tag{2.5.10}$$

This simple linear approximation of the Jacobian at $\mathbf{p}^0$ is used in the Marquardt technique, while a more sophisticated method is used to deal with nonlinearity in the Occam technique. As a result, Marquardt inversion requires an initial guess $\mathbf{p}^0$ that is relatively close to the minimum-misfit solution $\mathbf{p}^*$, which it steps towards over the course of a few iterations. Occam inversions, in contrast, may start from a uniform halfspace to avoid applying prejudice to the solution.

Once the Jacobian has been calculated, the linear least-squares solution to equation (2.5.7) may be found by computing

$$\delta\mathbf{p} = \left(\mathbf{A}^{\mathbf{T}}\mathbf{A}\right)^{-1} \mathbf{A}^{\mathbf{T}} \delta\mathbf{d} . \tag{2.5.11}$$

To step towards the minimum misfit solution, $\delta\mathbf{d}^{*0} = \mathbf{d}^* - \mathbf{d}^0$ is used. The weighting matrix **W** is applied to account for data uncertainties:

$$\delta\mathbf{p} = \left((\mathbf{WA})^{\mathbf{T}} \mathbf{WA}\right)^{-1} \left((\mathbf{WA})^{\mathbf{T}} \mathbf{W}\right) \delta\mathbf{d}^{*0} . \tag{2.5.12}$$

In practice, one or more of the parameters **p** may be poorly determined, leading to near-zero eigenvalues of $(\mathbf{WA})^{\mathbf{T}} \mathbf{WA}$, leaving it rank-deficient, thus nearly singular and unfit for stable inversion. Marquardt's method of dealing with this problem is to add a small positive constant λ to the diagonal elements of $(\mathbf{WA})^{\mathbf{T}} \mathbf{WA}$ prior to inversion:

$$\delta\mathbf{p} = \left((\mathbf{WA})^{\mathbf{T}} \mathbf{WA} + \lambda\mathbf{I}\right)^{-1} \left((\mathbf{WA})^{\mathbf{T}} \mathbf{W}\right) \delta\mathbf{d}^{*0} . \tag{2.5.13}$$

This technique is also known as ridge regression, or damped least-squares. Any small eigenvalues of the matrix to be inverted are increased by λ, stabilizing the inversion. A large

value of λ obscures the small eigenvalues, leading to a more stable algorithm that is sensitive to only the most strongly constrained features of the model. Ridge regression with large λ is appropriate away from the solution, *i.e.* when $\mathbf{d}^{*0}$ is also relatively large, but converges slowly because the eigenvectors of the inverted matrix $\left((\mathbf{WA})^{\mathbf{T}}\mathbf{WA}\right)^{-1}$ have been scaled down. For this reason, ridge regression is said to provide a *biased* estimate of $\delta\mathbf{p}$. Ridge regression with small λ converges rapidly near a minimum misfit solution, but may diverge away from any minima.

An iteration of the Marquardt inversion algorithm used in this study begins with the forward computation of $\mathbf{d}^0$ at $\mathbf{p}^0$, along with the initial misfit vector $\delta\mathbf{d}^{*0} = \mathbf{d}^* - \mathbf{d}^0$ and misfit X_0^2. The weighted Jacobian **WA** is computed at $\mathbf{p}^0$.

Next, the matrix $(\mathbf{WA})^{\mathbf{T}}\mathbf{WA} + \lambda\mathbf{I}$ is computed using an initial $\lambda = 0.01$. If it is not positive definite to numerical precision (a prerequisite for the numerical inversion method used), λ is increased by a factor of 10. Matrix inversion is then performed using the Cholesky factorization code of R. L. Parker, and equation (2.5.13) is solved for the parameter correction vector $\delta\mathbf{p}$.

A forward computation using the new parameter vector $\mathbf{p}^1$ yields $\mathbf{d}^1$ of misfit X_1^2; if the misfit increases, the code re-iterates with λ increased by a factor of 10 each time until the fit improves.

The algorithm continues to iterate until either convergence $\left(\mathrm{X}_0^2 - \mathrm{X}_1^2\right)/\mathrm{X}_0^2 < 10^{-4}$ (yielding $\mathbf{p}^*$) or excessive damping $\lambda > 10^{10}$ occurs.

Upon convergence, the parameter covariance matrix is computed at $\mathbf{p}^*$ to assess how well the model parameters are determined by the data:

$$\mathrm{cov}\left(\mathbf{p}^*\right) = \frac{\mathrm{X}_*^2}{N-M}\left(\left(\mathbf{WA}\right)^{\mathbf{T}}\mathbf{WA}\right)^{-1}. \tag{2.5.14}$$

An estimate of the standard deviation of each parameter comes from taking the square root of the associated diagonal element of $\mathrm{cov}\left(\mathbf{p}^*\right)$. The normalized correlation coefficients between parameters are found through normalization of the covariance matrix:

$$\mathrm{cor}\left(p_{ij}^*\right) = \frac{\mathrm{cov}\left(p_{ij}^*\right)}{\left[\mathrm{cov}\left(p_{ii}^*\right)\cdot\mathrm{cov}\left(p_{jj}^*\right)\right]^{1/2}} \ . \tag{2.5.15}$$

If $\left|\mathrm{cor}\left(p_{ij}^*\right)\right| \approx 1.0$, the relationship between parameters i and j is, by implication, linear. If $\mathrm{cor}\left(p_{ij}^*\right) \approx -1.0$, only the product $p_i p_j$ is well determined. If $\mathrm{cor}\left(p_{ij}^*\right) \approx +1.0$, only the ratio p_i/p_j is well determined.

2.5.2 Occam inversion

The Occam inversion method of Constable, *et al*. [1987] was designed to fit the data to a given misfit tolerance, regularized through minimization of the "roughness" R of the model. Occam was used to invert several subsets of CSEM data, with the 1-D isotropic modeling code of section 2.4.1 as the forward operator. Layer resistivities were variable parameters **p**, and layer thicknesses were fixed parameters **x** (Figure 2.15). Deeper layers were exponentially thicker; this is physically appropriate due to the exponential decrease in sensitivity with depth inherent in induction sounding.

Roughness is defined as the integrated square of the first or second derivative of resistivity **p** vs. depth:

$$R_1 = \int \left(dp/dz\right)^2 dz \tag{2.5.16}$$

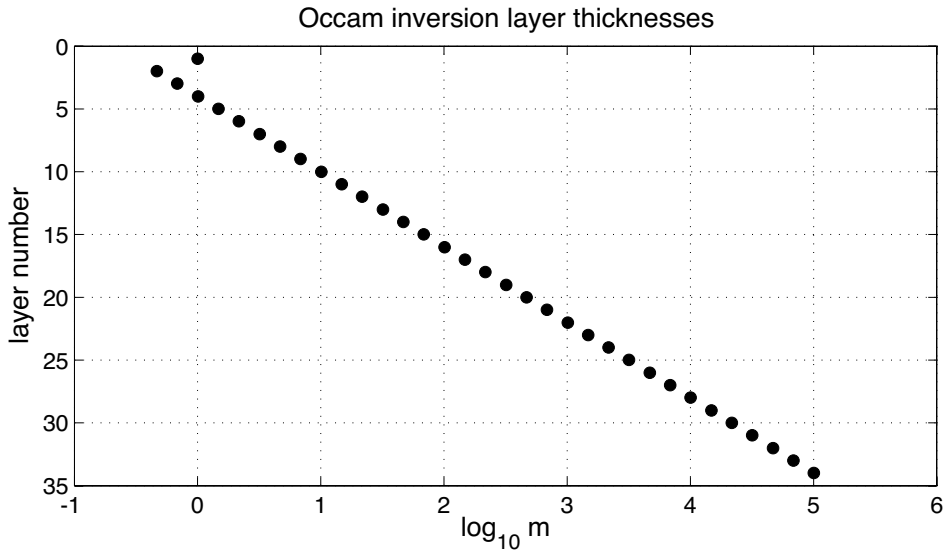

Figure 2.15 Occam inversion model layer thickness increases exponentially with depth below the seafloor. The top layer is set to 1.0 m, and the 35th subsurface layer is a basal halfspace. For unprejudiced Occam inversions of APPLE CSEM data, all layers began at $\rho = 3{,}000\ \Omega$m.

$$R_2 = \int \left(d^2 p / dz^2 \right)^2 dz \,. \tag{2.5.17}$$

Minimizing R_1 for a given misfit tolerance X^2_{TOL} finds the "smoothest" model, and so any structure present is essential to fitting the data. Minimizing R_2 penalizes departures from a linear trend in **p** vs. depth. It is important to note that abrupt, significant jumps in resistivity may very well occur in the real earth; these will be spread out across several model layers in a smooth inversion. The relatively long wavelengths of the diffusive electromagnetic waves generated in a CSEM sounding prevent high-resolution recovery of resistivity contrast interfaces, however, so a smoothing constraint fits the inherent resolution of the method.

In matrix notation, the roughness of a discrete model is computed by Euclidian norm

$$R_1 = \| \partial \mathbf{p} \|^2 \tag{2.5.18}$$

$$R_2 = \| \partial^2 \mathbf{p} \|^2 \tag{2.5.19}$$

where the $M \times M$ first-differencing operator is

$$\partial = \begin{bmatrix} 0 & & & & 0 \\ -1 & 1 & & & \\ & -1 & 1 & & \\ & & \ddots & \ddots & \\ 0 & & & -1 & 1 \end{bmatrix}. \tag{2.5.20}$$

The data misfit can also be expressed as a Euclidian norm:

$$\mathrm{X}^2 = \| \mathbf{W}\mathbf{d}^* - \mathbf{F}[\mathbf{p},\mathbf{x}] \|^2 . \tag{2.5.21}$$

This functional was minimized in Marquardt inversion; an Occam inversion finds the minimum of a functional that incorporates the model roughness (R_1 in this case) and target misfit X^2_{TOL}, as well:

$$U = \| \partial \mathbf{p} \|^2 + \xi^{-1} \left\{ \| \mathbf{W}\mathbf{d}^* - \mathbf{F}[\mathbf{p},\mathbf{x}] \|^2 - \mathrm{X}^2_{TOL} \right\} \tag{2.5.22}$$

where ξ is a Lagrange multiplier that weighs data misfit against model smoothness. Null values of the gradient $\nabla_{\mathbf{p}} U$ yield stationary values of U, and thus extremal values of R_1, including, of course, the minimum.

Occam is an iterative scheme; for sufficiently small steps $\delta\mathbf{p} = \mathbf{p}^1 - \mathbf{p}^0$, the Taylor expansion of equation (2.5.5) is again used:

$$\mathbf{F}[\mathbf{p}^0 + \delta\mathbf{p}] = \mathbf{F}[\mathbf{p}^0] + \mathbf{A}_0 \delta\mathbf{p} + \tilde{\varepsilon} \tag{2.5.23}$$

where $\mathbf{A}_0$ is the Jacobian evaluated at $\mathbf{p}^0$. Ignoring the higher order terms $\tilde{\varepsilon}$ to linearize the nonlinear problem, the functional U becomes

$$U = \left\| \partial \mathbf{p}^1 \right\|^2 + \xi^{-1} \left\{ \left\| \mathbf{W}\left(\mathbf{d}^* - \mathbf{F}[\mathbf{p}^0] + \mathbf{A}_0\mathbf{p}^0\right) - \mathbf{W}\mathbf{A}_0\mathbf{p}^1 \right\|^2 - \mathrm{X}_{TOL}^2 \right\}. \qquad (2.5.24)$$

Setting the gradient $\nabla_{\mathbf{p}} U$ equal to zero; solving for $\mathbf{p}^1$ will yield the model that minimizes *U*:

$$\mathbf{p}^1(\xi) = \left[\xi \partial^{\mathbf{T}} \partial + \left(\mathbf{W}\mathbf{A}_0\right)^{\mathbf{T}} \mathbf{W}\mathbf{A}_0 \right]^{-1} \left(\mathbf{W}\mathbf{A}_0\right)^{\mathbf{T}} \mathbf{W}\left(\mathbf{d}^* - \mathbf{F}[\mathbf{p}^0] + \mathbf{A}_0\mathbf{p}^0\right). \qquad (2.5.25)$$

The model misfit is now a function of ξ:

$$\mathrm{X}_{\mathbf{p}^1}^2(\xi) = \left\| \mathbf{W}\mathbf{d}^* - \mathbf{W}\mathbf{F}\left[\mathbf{p}^1(\xi)\right] \right\|^2. \qquad (2.5.26)$$

Sweeping through values of ξ minimizes the misfit in early iterations, and keeps the misfit at X_{TOL}^2 in later iterations, when roughness is being minimized.

Convergence is defined numerically as $\left\| \delta \mathbf{p} \right\|^2 \le 10^{-4}$, the algorithm quits after 99 iterations if it has not yet converged. It was observed that if convergence was to occur at all, it nearly always did so within 20 iterations (Table 4.3). All models presented in the analysis have been run to convergence, unless otherwise noted.

The functional *U* was for some inversions modified to include a model prejudice term:

$$\begin{aligned} U = \left\| \partial \mathbf{p}^1 \right\|^2 &+ \xi^{-1} \left\{ \left\| \mathbf{W}\left(\mathbf{d}^* - \mathbf{F}[\mathbf{p}^0] + \mathbf{A}_0\mathbf{p}^0\right) - \mathbf{W}\mathbf{A}_0\mathbf{p}^1 \right\|^2 - \mathrm{X}_{TOL}^2 \right\} \\ &+ \nu \left\| \mathbf{p}^1 - \mathbf{p}^{prej} \right\|^2 \end{aligned} \qquad (2.5.27)$$

where $\mathbf{p}^{prej}$ is the prejudice model and ν assigns a relative weight to the prejudice term. A value of $\nu = 10$ was used in this study (section 4.3.2); $\nu = 1$ had little effect on the inversion, while $\nu = 100$ completely overwhelmed the other terms in *U*.

2.6 Acknowledgement

Section 2.4.2, in part, is from the manuscript "The detection of an anisotropic layer in oceanic lithosphere by the seafloor controlled-source electromagnetic method" by Everett, M. E., Constable, S. C., and Behrens, J., prepared for submission to Geophysical Journal International. The dissertation author was a co-author of this manuscript.

2.7 References

Anderson, W. L. (1989), A hybrid fast Hankel transform algorithm for electromagnetic modeling, Geophysics, 54, 263-266.

Bannister, P. R. (1968), Determination of the electrical conductivity of the sea bed in shallow waters, Geophysics, 33, 995-1003.

Bevington, P. R. (1969), Data Reduction and Error Analysis for the Physical Sciences, McGraw-Hill, Boston.

Cagniard, L. (1953), Basic theory of the Magneto-Telluric method of geophysical prospecting, Geophysics, 18, 605-635.

Cairns, G. W., R. L. Evans, and R. N. Edwards (1996), A time domain electromagnetic survey of the TAG hydrothermal mound, Geophysical Research Letters, 23, 3455-3458.

Chave, A. D., S. C. Constable, and R. N. Edwards (1991), Electrical exploration methods for the seafloor, in Elecromagnetic Methods in Applied Geophysics, edited by M. N. Nabighian, pp. 931-966, Society of Exploration Geophysicists.

Chave, A. D., and C. S. Cox (1982), Controlled Electromagnetic Sources for Measuring Electrical Conductivity Beneath the Oceans, 1, Forward Problem and Model Study, Journal of Geophysical Research, 87, 5327-5338.

Chave, A. D., and D. S. Luther (1990), Low-frequency, motionally induced electromagnetic fields in the ocean. 1. Theory, Journal of Geophysical Research, 95, 7185-7200.

Cheesman, S. J., R. N. Edwards, and A. D. Chave (1987), On the theory of sea-floor conductivity mapping using transient electromagnetic systems, Geophysics, 52, 204-217.

Constable, C. G., and S. C. Constable (2004), Satellite magnetic field measurements: Applications in studying the deep earth, in The State of the Planet: Frontiers and Challenges in Geophysics, edited by R. S. J. Sparks and C. T. Hawkesworth, pp. 147-159, American Geophysical Union, Washington, D.C.

Constable, S., and C. S. Cox (1996), Marine controlled-source electromagnetic sounding 2. The PEGASUS experiment, Journal of Geophysical Research, 101, 5519-5530.

Constable, S. C. (1990), Marine electromagnetic induction studies, Surveys in Geophysics, 11, 303-327.

Constable, S. C., A. S. Orange, G. M. Hoversten, and H. F. Morrison (1998), Marine magnetotellurics for petroleum exploration; Part I, A seafloor equipment system, Geophysics, 63, 816-825.

Constable, S. C., R. L. Parker, and C. G. Constable (1987), Occam's inversion: a practical algorithm for generating smooth models from electromagnetic sounding data, Geophysics, 52, 289-300.

Cox, C. S., S. C. Constable, A. D. Chave, and S. C. Webb (1986), Controlled-source electromagnetic sounding of the oceanic lithosphere, Nature, 320, 52-54.

Cox, C. S., J. H. Filloux, and J. C. Larsen (1968), Electromagnetic studies of ocean currents and electrical conductivity below the ocean-floor, in The Sea, edited by A. E. Maxwell, pp. 637-693, Wiley, New York.

Daout, F., A. Khenchaf, and J. Saillard (1994), The effect of salinity and temperature on the electromagnetic field scattered by sea water, paper presented at OCEANS '94, Brest, France.

deGroot-Hedlin, C., and S. Constable (1990), Occam's inversion to generate smooth, two-dimensional models from magnetotelluric data, Geophysics, 55, 1613-1624.

Edwards, R. N., L. K. Law, and J. M. DeLaurier (1981), On measuring the electrical conductivity of the oceanic crust by a modified magnetometric resistivity method, Journal of Geophysical Research, 86, 11609-11615.

Eidesmo, T., S. Ellingsrud, L. M. MacGregor, S. Constable, M. C. Sinha, S. Johansen, F. N. Kong, and H. Westerdahl (2002), Sea Bed Logging (SBL), a new method for remote and direct identification of hydrocarbon filled layers in deepwater areas, FIrst Break, 20.3, 144-152.

Ellingsrud, S., T. Eidesmo, S. Johansen, M. C. Sinha, L. M. MacGregor, and S. Constable (2002), The Meter Reader - Remote sensing of hydrocarbon layers by seabed logging (SBL): Results from a cruise offshore Angola, The Leading Edge, 21, 972-982.

Evans, R. L. (1991), Electrical Resistivity Structure of the East Pacific Rise Near 13° N, Ph.D. thesis, 229 pp, University of Cambridge.

Evans, R. L., M. C. Sinha, S. C. Constable, and M. J. Unsworth (1994), On the electical nature of the axial melt zone at 13° N on the East Pacific Rise, Journal of Geophysical Research, 99, 577-588.

Everett, M. E., and S. Constable (1999), Electric dipole fields over an anisotropic seafloor: theory and application to the structure of 40 Ma Pacific Ocean lithosphere, Geophysical Journal International, 136, 41-56.

Everett, M. E., S. C. Constable, and J. Behrens (in preparation), The detection of an anisotropic layer in oceanic lithosphere by the seafloor controlled-source electromagnetic method, Geophysical Journal International.

Filloux, J. H. (1977), Ocean-floor magnetotelluric sounding over North Central Pacific, Nature, 269, 297-301.

Flosadóttir, Á. H., and S. Constable (1996), Marine controlled-source electromagnetic sounding 1. Modeling and experimental design, Journal of Geophysical Research, 101, 5507-5517.

Heinson, G., and S. Constable (1992), The electrical conductivity of the oceanic upper mantle, Geophysical Journal International, 110, 159-179.

Inman, J. R. (1975), Resistivity inversion with ridge regression, Geophysics, 40, 798-817.

Kato, Y., and T. Kikuchi (1950), On the phase difference of earth current induced by the changes of the earth's magnetic field, Sci. Rep. Tohoku Univ. Serv. V. Geophys., 2, 139-145.

Katsube, T. J., and L. S. Collett (1976), Electromagnetic Propagation Characteristics of Rocks, in The Physics and Chemistry of Minerals and Rocks: Proceedings of the NATO Advanced Study Institute on Petrophysics, held at the University of Newcastle upon Tyne, 22-26 April 1974, edited by R. G. J. Strens, John Wiley & Sons.

Keller, G. V. (1988), Rock and Mineral Properties, in Electromagnetic Methods in Applied Geophysics: Volume 1, Theory, edited by M. N. Nabighian, pp. 13-51, Society of Exploration Geophysicists, Tulsa, OK.

Key, K., S. Constable, J. Behrens, G. Heinson, and C. Weiss (2004), A look at the data from "Constraining the Magmatic Budget of the EPR at 9 N Using Broadband Marine MT", paper presented at American Geophysical Union, Fall Meeting, San Francisco, California.

Key, K. W. (2003), Application of Broadband Marine Magnetotelluric Exploration to a 3D Salt Structure and a Fast-Spreading Ridge, 109 pp, University of California, San Diego.

Luther, D. S., J. H. Filloux, and A. D. Chave (1991), Low-frequency, motionally induced electromagnetic fields in the ocean 2. electric field and Eulerian current comparison, Journal of Geophysical Research, 96, 12797-12814.

MacGregor, L., M. Sinha, and S. Constable (2001), Electrical resistivity structure of the Valu Fa Ridge, Lau Basin, from marine controlled-source electromagnetic sounding, Geophysical Journal International, 146, 217-236.

MacGregor, L. M. (1997), Electromagnetic investigation of the Reykjanes Ridge near 58° North, Ph.D. thesis, 264 pp, University of Cambridge.

MacGregor, L. M., S. Constable, and M. C. Sinha (1998), The RAMESSES experiment-III. Controlled-source electromagnetic sounding of the Reykjanes Ridge at 57°45' N, Geophysical Journal International, 135, 773-789.

Marquardt, D. W. (1963), An algorithm for least-squares estimation of nonlinear parameters, J Soc Indust Appl Math, 11, 431-441.

Marquardt, D. W. (1970), Generalized inverses, ridge regression, biased linear estimation, and nonlinear estimation, Technometrics, 12, 591-612.

Narayan, S., M. B. Dusseault, and D. C. Nobes (1994), Inversion techniques applied to resistivity inverse problems, Inverse Problems, 10, 669-686.

Olhoeft, G. R. (1976), Electrical properties of rocks, in The Physics and Chemistry of Minerals and Rocks: Proceedings of the NATO Advanced Study Institute on Petrophysics, held at the University of Newcastle upon Tyne, 22-26 April 1974, edited by R. G. J. Strens, pp. 261-278, John Wiley & Sons.

Petrick, W. R., W. H. Pelton, and S. H. Ward (1977), Ridge regression inversion applied to crustal resistivity sounding data from South Africa, Geophysics, 42, 995-1005.

Schwalenberg, K., E. Willoughby, R. Mir, and R. N. Edwards (2005), Marine gas hydrate electromagnetic signatures in Cascadia and their correlation with seismic blank zones, FIrst Break, 23, 57-63.

Shannon, R. D., M. A. Subramanian, S. Hosoya, and G. R. Rossman (1991), Dielectric Constants of Tephroite, Fayalite and Olivine and the Oxide Additivity Rule, Phys. Chem. Minerals, 18, 1-6.

Sinha, M. C., P. D. Patel, M. J. Unsworth, T. R. E. Owen, and M. G. R. MacCormack (1990), An active source electromagnetic sounding system for marine use, Marine Geophysical Research, 12, 59-68.

Smith, B. D., and S. H. Ward (1974), On the computation of polarization ellipse parameters, Geophysics, 39, 867-869.

Spiess, F. N., K. C. Macdonald, T. Atwater, R. Ballard, A. Carranza, D. Cordoba, C. Cox, V. M. Diaz Garcia, J. Francheteau, J. Guerrero, J. Hawkins, R. Haymon, R. Hessler, T. Juteau, M. Kastner, R. Larson, B. Luyendyk, J. D. Macdougall, S. Miller, W. Normark, J. Orcutt, and C. Rangin (1980), East Pacific Rise: Hot Springs and Geophysical Experiments, Science, 207, 1421-1433.

Tikhonov, A. N. (1950), On determining electrical characteristics of the deep layers of the earth's crust, Dokl. Akad. Nauk., USSR, 73, 295-297.

Tyburczy, J. A., and D. K. Fisler (1995), Electrical Properties of Minerals and Melts, in Mineral Physics and Crystallography: A Handbook of Physical Constants, edited by T. Ahrens, pp. 185-208, American Geophysical Union, Washington, DC.

Unsworth, M. J., B. J. Travis, and A. D. Chave (1993), Electromagnetic induction by a finite electric dipole source over a 2-D earth, Geophysics, 58, 198-214.

Vanyan, L. L. (1967), Electromagnetic Depth Soundings, 312 pp., Consultants Bureau, New York.

Ward, S. H., and G. W. Hohmann (1988), Electromagnetic Theory for Geophysical Applications, in Electromagnetic Methods in Applied Geophysics: Volume 1, Theory, edited by M. N. Nambighian, pp. 130-311, Society of Exploration Geophysicists, Tulsa, OK.

Warren, S. (2004), Exxon Mobil Bets On New Technology In the Hunt for Oil, in The Wall Street Journal, edited, p. A1, New York.

Webb, S. C., S. C. Constable, C. S. Cox, and T. K. Deaton (1985), A Seafloor Electric Field Instrument, Journal of Geomagnetism and Geoelectricity, 37, 1115-1129.

Webb, S. C., and C. S. Cox (1986), Observations and modeling of seafloor microseisms, Journal of Geophysical Research, 91, 7343-7358.

Weitemeyer, K., S. Constable, K. Key, and J. Behrens (2004), A Pilot Marine EM Study of Hydrate Ridge, Oregon, paper presented at American Geophysical Union, Fall Meeting, San Francisco, California.

Young, P. D., and C. S. Cox (1981), Electromagnetic active source sounding near the East Pacific Rise, Geophysical Research Letters, 8, 1043-1046.

Yu, L., and R. N. Edwards (1992), The detection of lateral anisotropy of the ocean floor by electromagnetic methods, Geophysical Journal International, 108, 433-441.

Yu, L., R. L. Evans, and R. N. Edwards (1997), Transient electromagnetic responses in seafloor with triaxial anisotropy, Geophysical Journal International, 129, 292-304.

Zonge, K. L., and L. J. Hughes (1991), Controlled Source Audio-Frequency Magnetotellurics, in Electromagnetic Methods in Applied Geophysics, edited by M. N. Nabighian, pp. 713-809, Society of Exploration Geophysicists, Tulsa, Oklahoma.

Chapter 3

Data Acquisition and Processing

3.1 Introduction

In this chapter, acquisition and processing of the APPLE CSEM data set will be described: the equipment used in the field, instrument positions and orientations, data reduction routines, and data uncertainty analysis.

In brief, eight receivers were deployed around a 30 km radius circle, with several more deployed at the center (Figure 3.1). The transmitter was towed around the perimeter of this circle to test for anisotropic conductivity; the other tow paths provide supplementary data. The western part of the large circle was towed during days 61 and 62; the semicircle and long

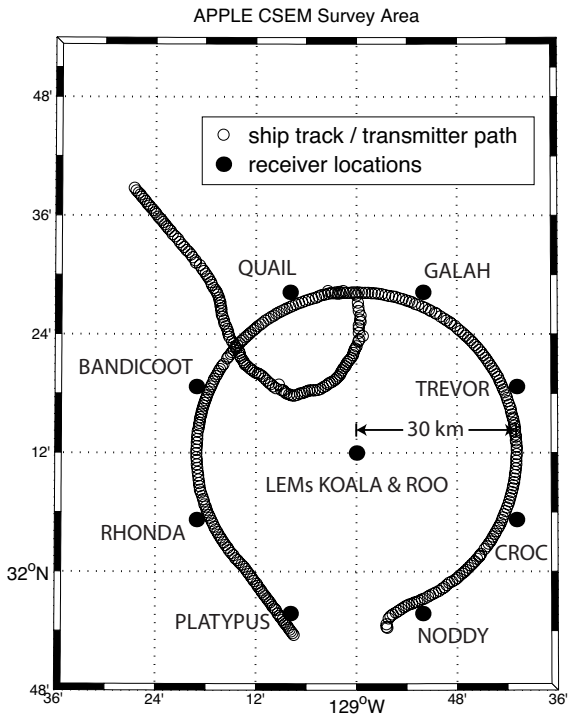

Figure 3.1 Transmitter tow paths with receiver names and locations. (UTM Projection)

radial tow during days 63 and 64, and the eastern circle on days 66 and 67 (Table 3.1). (These are ordinal dates of the year 2001, which run from 1 [Jan 1] to 365 [Dec 31]; the term Julian Date is sometimes used to name this convention.)

For all of the navigation work described herein, latitudes and longitudes (computed by the ship's navigational software from GPS positioning using the WGS84 spheroid) were converted to a UTM projection, based on the Clark 1866 spheroid, with the equator as basal latitude and 129°W as the central meridian. (The available UTM code used was hardwired for the Clark spheroid; it has earth radii that are within 500 m of more recently developed spheroids (such as WGS84). Across the ~100 km APPLE CSEM survey area, relative geometric relationships between data acquisition equipment are not significantly affected by

Time (Julian Date, 2001)		Tow Path Event
061:06:30:00	61.270833	Start West Circle
062:18:30:00	62.770833	End West Circle
063:00:42:00	63.029167	Start Semicircle
063:11:00:00	63.458333	Start Long Radial Tow
064:11:00:00	64.458333	End Long Radial Tow
066:06:38:00	66.276389	Start East Circle
067:17:30:00	67.729167	End East Circle

Table 3.1 Transmitter tow path timeline.

its use.) The R/V Thompson acquired GPS positions using P-Code, and her navigation log, which was updated automatically every minute, on the minute, was the dataset upon which all equipment positions were based. The lateral offset between the GPS antenna and the hull transducer was accounted for when surveying seafloor instruments (section 3.3.1) and estimating transmitter position using ship track bathymetry (section 3.2.2).

3.2 Transmitter

The transmitter used in this experiment was the Deeptowed Active Source Instrument (DASI), operated by Southampton Oceanography Centre (SOC). High voltage at low current was fed down the winch cable to the main body of DASI, where it was transformed into low voltage, high amperage current between two electrodes: one near the body, and the other trailing 100 m behind the first; an arrangement which creates a horizontal electric dipole. The seawater carries the return current. The output current was governed by a fully rectified quasi-square waveform, with a zero-to-peak amplitude of ~135 A. The resulting dipole moment was

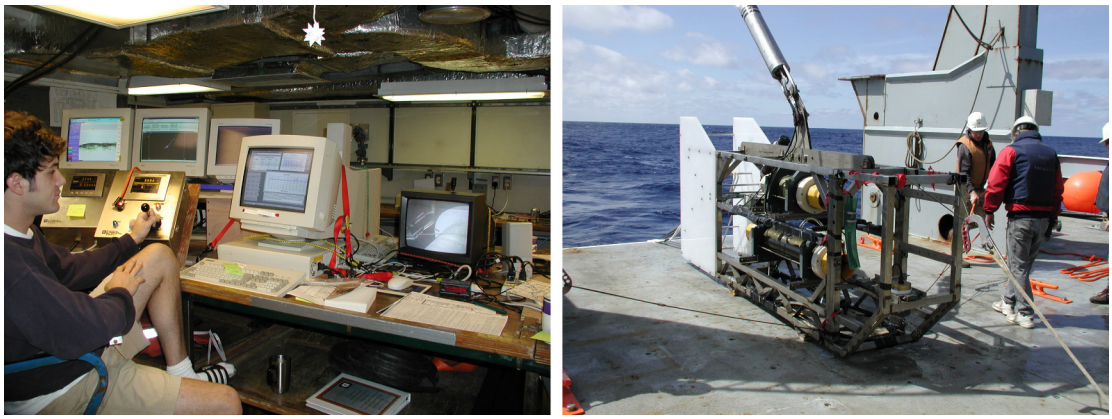

Figure 3.2 (*l*) Deeptow winch control station and (*r*) DASI on the aft deck.

17040 Am at the fundamental frequency of 4 Hz. This dipole moment estimate comes from transforming the waveform, as captured by a "piggyback" logger on DASI's frame, into the frequency domain – work done by Lucy MacGregor of SOC.

DASI was deeptowed at the end of a winch line at a mean altitude of 90 m above the seafloor (Figure 3.2). A 1 Hz stream of data from an acoustic altimeter mounted on DASI's frame allowed for continuous, real-time active control of transmitter height via the winch. Altitude was kept within 10 m of the target value. DASI also carried a pressure-sensitive depth gauge, the measurements from which were also recorded once every second.

Ship speed was restricted to 1 - 2 kts during deeptow operations (Figure 3.3) (1 kt = 1.852 km/hr = 30.83 meters/minute ≈ ½ m/s). This slow speed was maintained for several reasons. A small winch line angle affords better vertical control of the deeptow package. Keeping it closer, laterally, to the ship also reduces the uncertainty in transmitter position and orientation. Furthermore, a slowly moving transmitter means that longer stack frames can be analyzed during data processing (section 3.4.2.3).

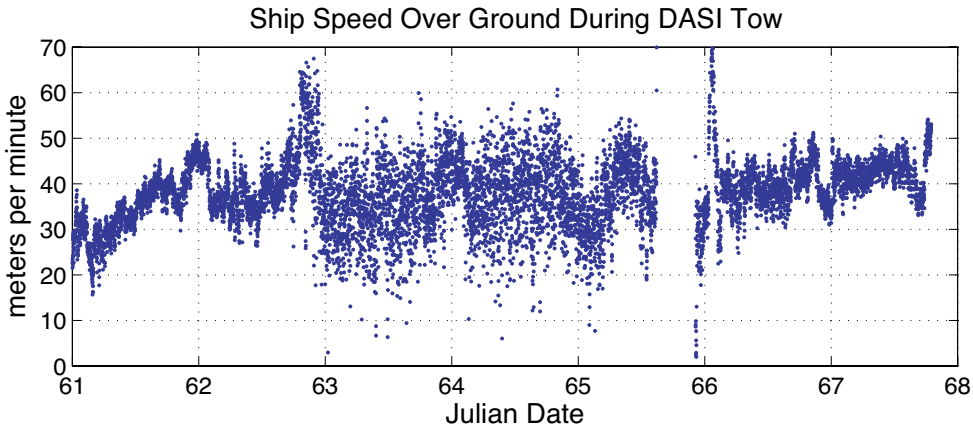

Figure 3.3 In order to maintain a steep wire angle, transmitter tow speeds were kept as slow as the sea state would allow. Inclement weather on days 63-64 is visible as increased scatter in the data.

3.2.1 Tow Extent

DASI was towed 7/8 of the way around a 30 km radius circle, in a smaller semi-circle of approximately 15 km radius around receiver QUAIL, and on a long radial tow away from the center receivers, transmitting continuously out to a range of 70 km (Figure 3.1).

The proposed experiment design also called for a 5 km radius tow around the center of the array, another, partial circular tow at 50 km radius, and an additional, orthogonal radial tow. The R/V Thompson, however, arrived late in San Diego prior to the experiment, eliminating 2.5 days of time at sea; winch installation cost another day. Furthermore, a strong storm (40 kt winds, 5-10 m swell) passed through the area during transmitter deeptow operations, costing nearly 40 hours of transmission time. It arrived as the west side of the circle was being completed; maintaining the ship's heading into the wind fortuitously resulted in the small semi-circle and long radial tows.

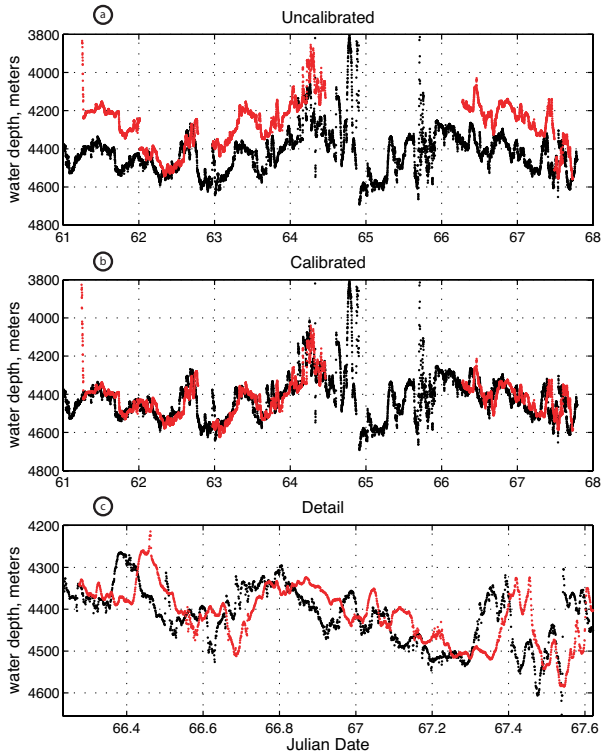

Figure 3.4 The preferred estimate of transmitter location was achieved through correlation of (c) peaks and valleys in DASI's bathymetric profile with those in the ship's bathymetric profile. (a) DASI's raw pressure depth gauge data (b) required calibration.

3.2.2 Transmitter Position and Orientation

Navigational uncertainty is a significant issue in CSEM data analysis, especially at short source-receiver offsets and in mixed-mode orientations. When operating in shallower water (depth < 3 km), hull mounted short baseline acoustic navigation systems can be used to track, ideally, both the head and tail of the transmitter. APPLE, however, was carried out in ~4400 m water depth, and with no acoustic ranging of any sort between the ship and the transmitter.

An initial attempt was made to chart the transmitter's location along the ship track by simply assuming a triangle with the ship's acoustically determined water depth on one side

(minus transmitter height) and the winch wire out as hypotenuse. A few variations on this idea were tried (i.e. using the pressure gauge inferred DASI depth as a triangle side; retracing along the arc of the ship track instead of along a chord). The maximum electric field magnitudes measured by the receivers and the shortest source-receiver offsets were, however, misaligned systematically by at least a kilometer or two. This method was placing the transmitter too close to the ship. The likely culprit is the wire-out estimate: it was not recorded automatically in the ship's log, so the manual log, recorded at 15 minute intervals, was the only estimate available. In addition, the wire-out value may have been poorly calibrated, or may not have been zeroed properly.

Since DASI carried a pressure depth gauge and a bottom-ranging acoustic transponder, data from these instruments were combined to generate a bathymetric profile along DASI's tow path. When compared with the bathymetric profile along the GPS-determined ship track (Figure 3.4), a high degree of correlation is obvious. The calibration offset of the pressure depth gauge jumped several times during the deeptow. After removing these offsets, the peaks and valleys of the two profiles were correlated manually. The transmitter was then simply assigned to the same position that the ship had been over the same bathymetric feature.

The position estimates obtained from these two methods differ systematically (Figure 3.5). Cubic splines were used to interpolate the correlated position picks; this was done independently in Northing vs. time and Easting vs. time. When the splined correlated transmitter positions were merged with the electric field data, maximum field strength corresponded with shortest source-receiver offset (except for one anomalous instrument; section 3.4.2.2).

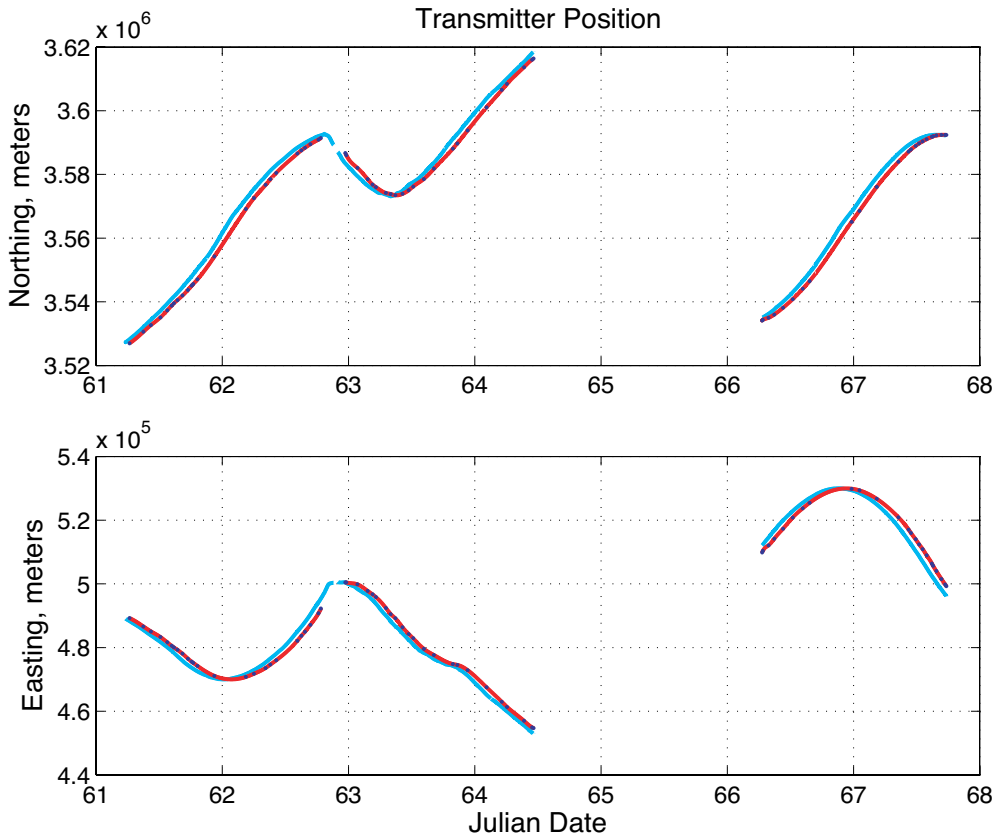

Figure 3.5 Two estimates of transmitter position. The blue lines are from retracing the ship track by a distance determined by creating a triangle with the transmitter depth on one side and the winch wire out as hypotenuse. The red lines are cubic splines through points determined by correlating the bathymetric profile at DASI with the profile below the ship. The correlation method produced a more accurate estimate, based on comparison with the electric field magnitudes measured by perimeter instruments, and was used in data processing.

Figure 3.6 illustrates the process of estimating transmitter azimuth (here, synonymous with geodetic orientation). Retracing the ship track and choosing the course over ground (COG) value is clearly unrealistic, due to the amount of scatter. The correlated azimuth value was therefore computed by averaging 21 minutes worth of COG values, centered at the correlation pick. These azimuth picks were then interpolated by cubic spline.

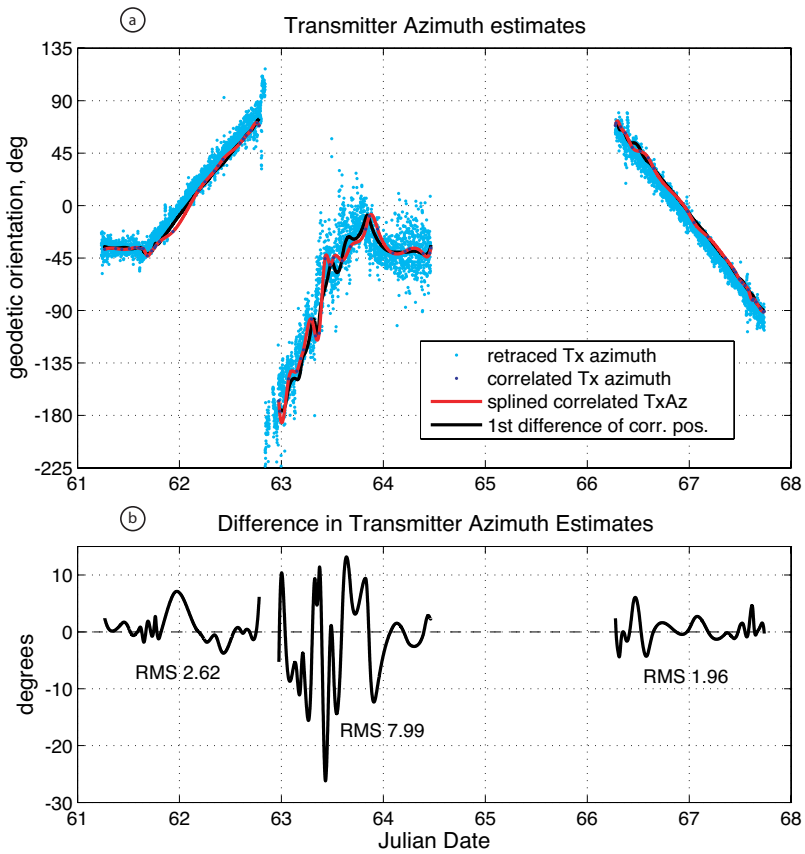

Figure 3.6 (a) Three estimates of the geodetic orientation of the transmitter. The cyan dots correspond to the cyan lines in Figure 3.5; this retracing method was found to be biased and was rejected. Correlated azimuth values are means of 21-minute data segments centered at the correlation pick, with a cubic spline interpolating (represented in red). The black line comes from the first difference of the splined positions in Figure 3.5. The red line was used for data processing, but the black line estimate is equally valid; the RMS difference between the two (b) provides an estimate of uncertainty.

These splined correlation picks became the navigational parameters used for merger with the electric field data. Figure 3.7 summarizes the preferred navigation parameters used for data processing.

In regards to the uncertainty of these estimated navigational parameters, it is highly unlikely that the transmitter followed the ship track exactly; indeed, while towing a curved path, the transmitter tends to trace a curve inside that of the ship, when seen from above.

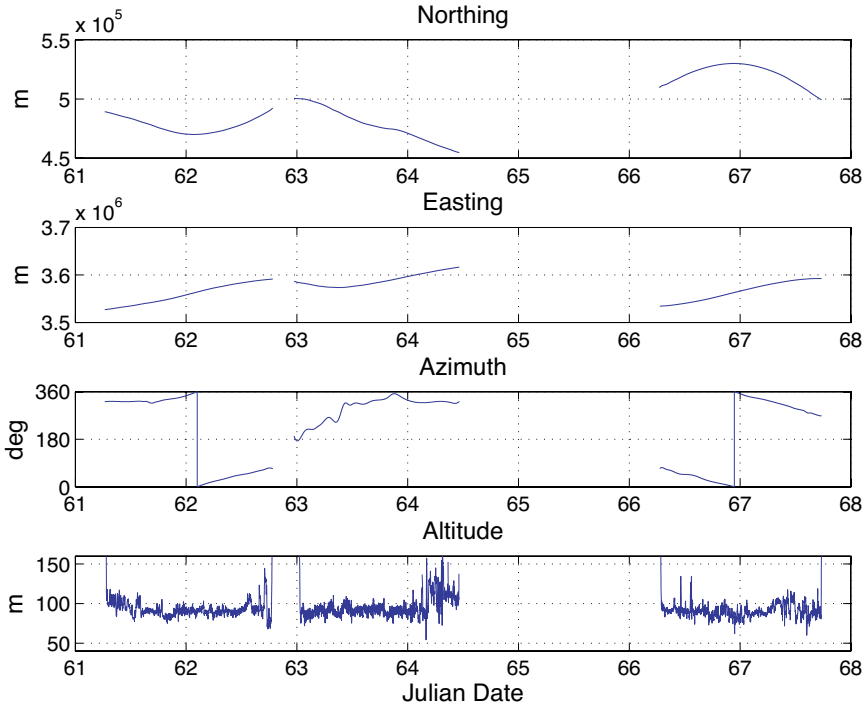

Figure 3.7 A summary plot of the navigational parameters used to process the data.

Another concern is that currents could push the transmitter horizontally away from the hypothetical tow path, or yaw the transmitter antenna. Furthermore, the sampling period of the ship's navigation log is one minute, which corresponds to ~ 40 meters of motion during deeptow operations. It is reasonable to assume uncertainty in the location on the order of 100 m.

An estimate of the uncertainty in azimuth comes from comparing the splined correlated picks with the first difference of the splined location picks. RMS values for the three main segments (western part of the large circle; semicircle and long radial tow; eastern part of the large circle) are 2.62°, 7.99°, and 1.96°, respectively.

The discussion of data uncertainty will be continued in section 3.5.

3.2.3 Clock Drift and Transmission Frequency

DASI's transmission frequency was regulated by a quartz crystal oscillator, internal to the deeptowed transformer package. This clock was, unfortunately, not stable enough to produce a constant output frequency: its primary linear drift shifted the mean transmission frequency away from the intended 4.00 Hz; higher-order components of the clock drift caused the transmission frequency to wander about this mean.

An FFT of the electric field time series at perimeter receiver CROC during the nearest approach of DASI yielded a mean transmission frequency of 3.99 Hz. To get a more precise estimate, data from receiver KOALA at the shortest source-receiver offset and coincident data from the DASI piggyback logger were analyzed more carefully. First, the sinusoid which best fit the electric field time series in the least squares sense (section 3.4.2.1) was computed for a range of frequencies centered about 3.99 Hz. Then, for each frequency f the residual R to the fit was computed as the 2-norm of the difference between the data and the parameter fit, integrated over the time series by use of the trapezoidal rule:

$$R(f) \equiv \frac{1}{2f_s} \sum_t \left[E(t_i) - A(f)\sin(2\pi f t_i) + B(f)\cos(2\pi f t_i) \right]^2 \qquad (3.3.1)$$

where f_s is sampling frequency, E is the electric field data, and A and B are the best-fit sinusoid coefficients. Data from KOALA were analyzed: 120 seconds of time series starting at JD 063:08:30:00 (Figure 3.8 b,c). Data from DASI's piggyback logger were also analyzed: file 110a, which contains 35 minutes of data, sampled at 125 Hz, starting at 063:08:18:21 (Figure 3.8 a,d). The minimum values of $R(f)$ occur at a mean of f = 3.9889 Hz, and vary by +/- 0.0006 Hz. A fundamental transmission frequency of 3.9889 Hz was, therefore, used to process the electric field data from all instruments in the array.

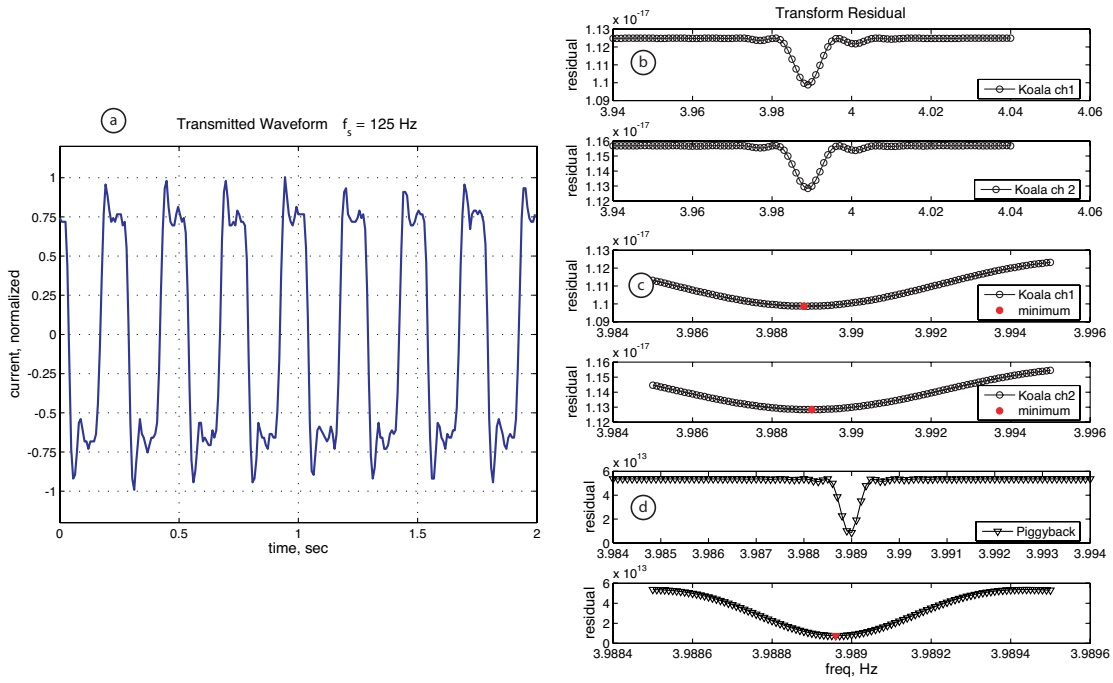

Figure 3.8 (a) Transmitted waveform as recorded by the piggback logger at time JD 063:08:18:21. An imprecise clock in DASI caused the transmission frequency to drift away from the intended 4 Hz. (b) Two minutes of high signal-to-noise ratio data from KOALA were transformed at a range of frequencies. The minimum residual indicates the true transmission frequency. (c) A denser array of frequencies was investigated near the minimum misfit. (d) 35 minutes of data from DASI's piggyback logger, coincident with the KOALA data, were also analyzed.

The largest, linear portion of the clock drift (3 ms per second, equal to 10 seconds per hour) was thus remedied by adjusting the data processing frequency. Initial data processing indicated two slightly different rates of linear clock drift, as well the presence of higher order terms on day 62; these were compensated for by directly applying corrective terms to the phase drift in the data – see section 3.4.2.2 for further discussion.

The unfortunate consequence of the severe, variable clock drift is that absolute phase data are fundamentally unavailable for interpretation. All CSEM transmitters are now regulated with GPS time, leaving this complication in the past.

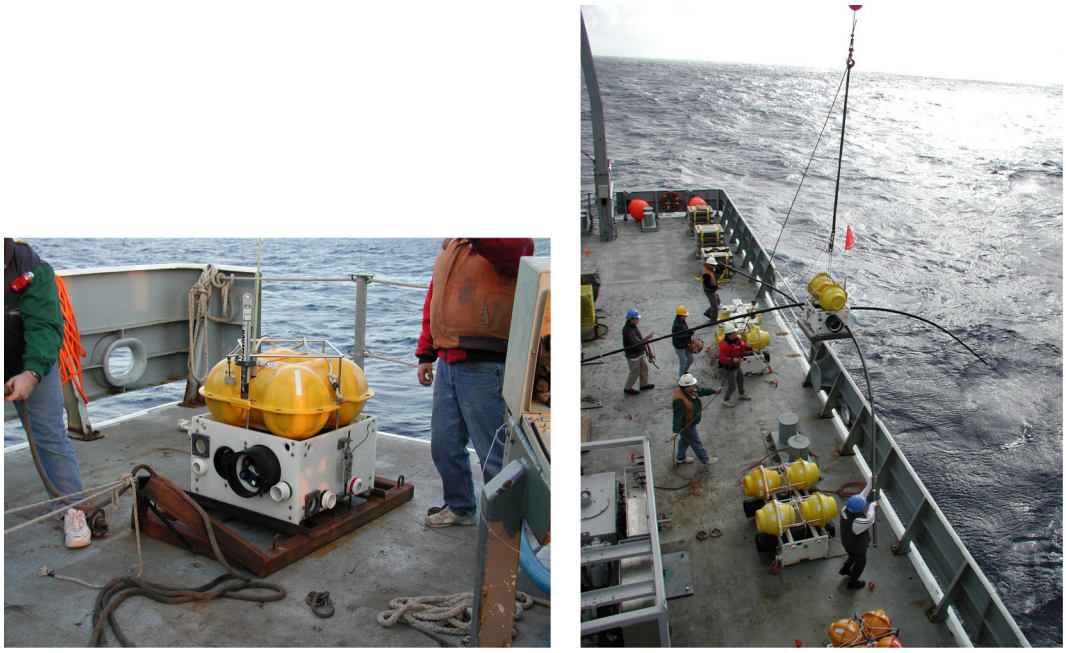

Figure 3.9 (*l*) OBEM Mk II instrument on a LEM sled just prior to deployment; the 177 m HED antenna trails behind the sled during deeptow deployment. (*r*) ELF instrument (with orthogonal 10 m HED antennae) being deployed over the port side of the aft deck.

3.3 Receiver Array

Eight electric field sensors (Figure 3.9), each with two orthogonal horizontal 10 m dipole antennae, were deployed at the perimeter of the array. They were located at vertices of a regular octagon, the sides of which were tangential to the circumference of a 30 km radius circle (Figure 3.1). Four single-component long-wire electric field receivers (LEMs) were deployed at the center of the circle, two aligned north-south and two aligned east-west. These had 177 m electrode offsets for increased sensitivity. Additionally, three more short-arm (10 m dipole), two-component receivers were deployed at the center of the array.

Two vintages of SIO seafloor electric field sensors were used. Seven older-generation

ELFs (ELectric Field sensors) were deployed: at four of the perimeter sites (QUAIL, TREVOR, NODDY, and RHONDA), as a pair of orthogonal LEMs (KERMIT and ULYSSES), and as a two-component instrument at the center of the array, near the LEMs (LOLITA). Eight newer-generation SIO OBEM (Ocean-Bottom ElectroMagnetic) Mk II instruments were also deployed: at the remaining four perimeter sites (BANDICOOT, PLATYPUS, CROC, and GALAH), as another pair of orthogonal LEMs (KOALA and ROO), and two as short-arm instruments at the center of the array (WALLABY and WOMBAT). WALLABY, WOMBAT, and Lolita returned data that were used in the MT analysis, but the transmitted CSEM electric fields were at or below the noise levels of these instruments for the duration of the experiment.

These receivers are the result of several decades of development at SIO [Constable*, et al.*, 1998; Webb*, et al.*, 1985]. Pairs of 15 cm long by 4 cm diameter silver-silver chloride electrodes were capacitively coupled to a chopper amplifier circuit, common to all the instruments. Time-varying potential differences between electrode pairs were converted into binary digital data through the use of voltage controlled oscillators in the ELFs (at a sampling rate of 32 Hz), or 16-bit analog-to-digital converters in the OBEM Mk II instruments (at a sampling rate of 125 Hz). Data were stored temporarily in a RAM buffer. Each time the RAM reached its storage capacity, the logger's hard drive was powered up and the contents of the buffer were transferred over all at once.

Two of the channels on each of these instruments were used to record electric fields. Each orthogonal electrode pair was assigned to its own channel on a standard instrument, while the LEMs were configured to have two pairs of electrodes of equal offset and orientation, each with its own channel.

All of the receivers were successfully recovered with data.

3.3.1 Locations and orientations

Instruments deployed at the center of the array, which includes the LEMs, were surveyed acoustically. In this simple survey, the ship traced two orthogonal lines over the instrument cluster, while acoustic pulses were broadcast every four seconds and the subsequent instrument reply arrivals were recorded on a graphic log. Later, the graphic log was carefully hand-digitized with a ruler and a ten-point divider.

In-situ sound speed data were not collected at the survey site, so a standard seawater sound speed estimate of 1500 m/s was used to analyze the two-way travel time data. After combining the ship's log of GPS positions with the acoustic data by matching the time axes, the data were inverted with a Marquardt algorithm using a simple geometric triangulation forward model.

3.3.1.1 LEM receivers

The LEMs had one acoustic unit each, on the instrument package at one end of the 177 m dipole. The ship speed and course over ground were recorded in the log, and a careful look at these parameters during deployment of OBEM Mk II LEMs KOALA and ROO (Figure 3.10) indicate that they are aligned to 0° and -90° +/- 0.5° geodetic, respectively. LEMs KERMIT and ULYSSES contained the higher-noise ELF data logger system. They were deployed as a redundant backup because, unlike the ELFs, OBEM Mk II receivers had never been deployed as LEMs before this experiment. The OBEM Mk II LEMs recorded significantly cleaner data (Figure 3.28); the ELF LEM data were ultimately not required to meet the objectives of the experiment.

Data from the KOALA/ROO pair of orthogonal dipoles were combined to create a virtual two-component instrument, the location of which was computed by starting with the surveyed

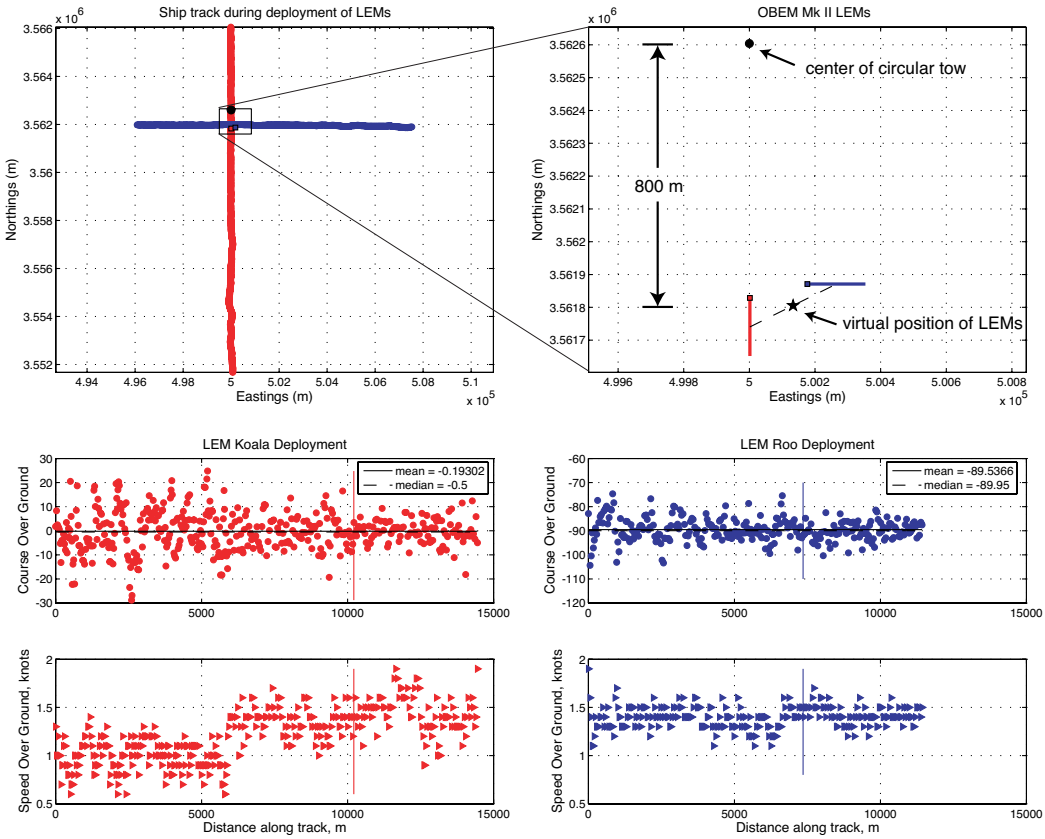

Figure 3.10 LEMs were deeptowed into position near the center of the array. KOALA was deployed while the ship was traveling due north (a,c), and ROO while traveling due west (a,d). Their "heads" were located by acoustic survey; the mean location of the dipole midpoints (b) was used as the virtual location of the combined full horizontal field measurement.

positions of the data loggers, estimating the antenna midpoints by moving 88.5 m towards the far end of each, and finding the center of the straight line joining those midpoints.

3.3.1.2 Perimeter receivers

Drop locations for the short-arm receivers were recorded during deployment. The ship's GPS antenna was the reference location, and the instruments were deployed from the port side of the aft deck, approximately 20 m aft and 8 m to port of the GPS antenna. For the receivers

	Drop Location				water depth, m
	Latitude N	Longitude W	UTM North, m	UTM East, m	
GALAH OBEM	32° 28.2340’	128° 52.0790’	3592415	512406	4470
TREVOR ELF	32° 18.7066’	128° 40.8704’	3574850	530014	4325
CROC OBEM	32° 05.2463’	128° 40.9418’	3549984	529975	4307
NODDY ELF	31° 55.7620’	128° 52.1080’	3532427	512434	4351
PLATYPUS OBEM	31° 55.7533’	129° 07.8562’	3532411	487623	4394
RHONDA ELF	32° 03.2360’	129° 19.0597’	3549965	470023	4101
BANDICOOT OBEM	32° 18.6993’	129° 19.0955’	3574837	470041	4452
QUAIL ELF	32° 28.2340’	129° 07.9340’	3592415	487574	4344
LEMs OBEM			3561806	500133	4465

Table 3.2 Receiver locations. Combined LEMs position is from estimated antenna midpoints, not drop location. Central meridian is 129° W.

on the perimeter of the array, those drop locations are the best estimates of their locations on the seafloor. Due to time constraints, no attempt was made to better estimate their positions through acoustic surveying. Table 3.2 lists instrument positions used in the data analysis.

The acoustically surveyed short-arm receivers at the center of the array remained too far from the transmitter, unfortunately, to collect useful CSEM data (their data, however, were used in the MT analysis). By comparing the recorded drop location with the surveyed seafloor location of instrument LOLITA, it was estimated to have drifted ~200 m laterally in a south-southwesterly direction during descent, providing a constraint on the magnitude of navigational uncertainty (see section 3.5 for further discussion).

Seafloor orientation of the short-arm, two-component receivers is uncontrollable and unpredictable. At the time of the APPLE experiment, seafloor orientations were ostensibly measured with an outboard mechanical “sugar compass”: a simple compass needle is allowed to rotate freely until spring-loaded plunger clamps down on it; crystalline sugar secures the

plunger in a small metal tube (and away from the compass needle) initially. In theory, the sugar would not dissolve until after the instrument has settled onto the seafloor, and upon recovery the compass would indicate its deployment orientation. In practice, however, the sugar compass has proven to be unreliable (this became evident during CSEM surveys conducted shortly after APPLE, including data collected over the Gemini salt body in the Gulf of Mexico [Key, 2003]).

Anisotropic forward modeling [Everett and Constable, 1999] (see section 2.4.2) has demonstrated the potential usefulness of single-component field analysis, motivating further attempts to determine perimeter instrument orientations.

Two methods were employed to estimate these orientations. The first was computation of the coherence of the long period natural source electric fields between the combination of LEMs KOALA and ROO (for which the antenna orientations are well constrained) and each perimeter receiver. The second involves a close look at the orientation of the polarization ellipse during the closest approach of the transmitter.

At low enough temporal frequencies, the natural source electromagnetic fields measured across the instrument array will be noticeably coherent. This, indeed, is the basis of the "plane wave approximation" used in the MT method (section 2.3.3). LEMs KOALA and ROO were used as the reference fields aligned with geodetic north and east, respectively. Fields measured on the orthogonal electric field channels of the perimeter instruments were mathematically rotated in increments of five degrees; channel 1 was compared with KOALA, channel 2 with ROO. Coherence is a normalized measure of the cross spectrum between two time series:

$$C_{xy} = \frac{\left|P_{xy}\right|^2}{P_{xx}\,P_{yy}} \tag{3.4.1}$$

where P_{xy} is the cross-spectrum between time series *x(t)* and *y(t)*, and P_{xx} and P_{yy} are the power spectra of *x* and *y* (this is, more specifically, the *mean squared coherence*).

Coherence ranges in value from 0 to 1, with 1 designating complete coherence. In this rotational example, coherence has a periodicity of 180°, so the cross-correlation was also computed to remove the polarity ambiguity. The cross-correlation *r*, which ranges from –1 (anti-correlated) to 0 (uncorrelated) to 1 (correlated), is the normalized zero-lag cross-covariance:

$$r_{xy} = \frac{\sigma_{xy}}{\sigma_x \sigma_y} \tag{3.4.2}$$

where σ_{xy} is the cross-covariance between *x(t)* and *y(t)* and σ_x and σ_y are the individual variances.

Ambient electromagnetic field fluctuations are not truly stationary, so some trial-and-error was necessary to find a period of time when they were coherent enough for this analysis. Julian Date 2001:65, from 16:00-22:00 UTC provided the requisite quasi-stationary natural source fields (also untainted by controlled-source transmission). Comparing QUAIL to the LEMs (Figure 3.11), the signals are coherent for periods longer than ~500 seconds, reaching maximum coherence when QUAIL has been rotated by ~140° anticlockwise. In the way they were deployed and subsequently handled in this calculation, the virtual combined LEM channel polarization is opposite that of the two-channel instruments. The negative correlation coefficients mean, therefore, that QUAIL's channel 1 is oriented at 140±5° geodetic. The broad peaks in the coherence show that this method is subject to significant inherent uncertainty; the peaks in the correlation coefficient are even broader.

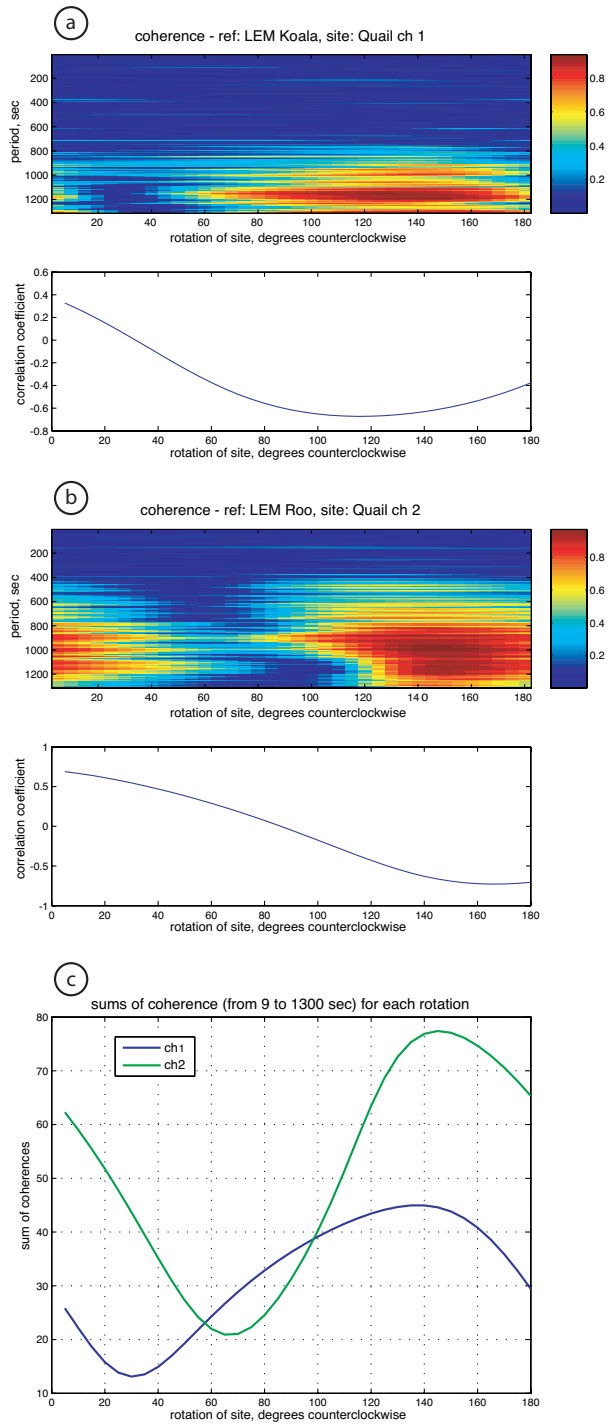

Figure 3.11 Orientation of the perimeter instruments was estimated by rotating the data and measuring coherence and correlation with natural source fields measured by the LEMs. Each channel was compared independently (a,b), and peaks in the summed coherence (c) indicate the best estimate.

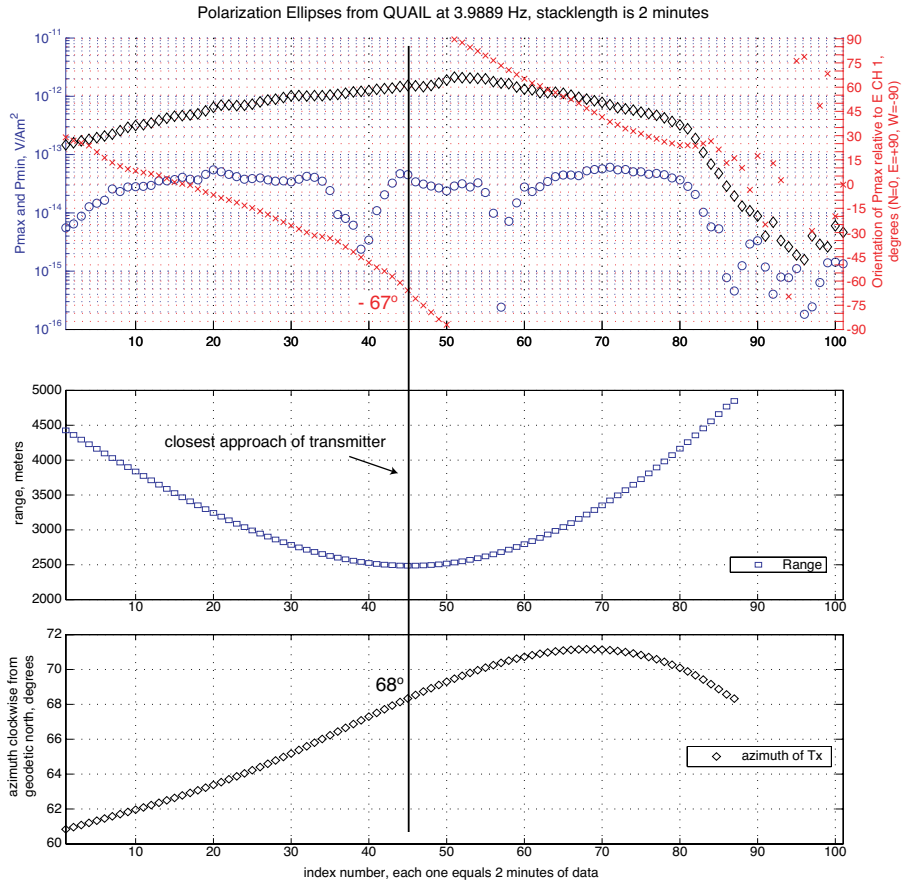

Figure 3.12 Perimeter instrument orientation as estimated by comparing polarization ellipse orientation with the transmitter orientation at the shortest source-receiver offset.

For the second method of determining instrument orientation, the transmitter orientation, source-receiver offset, and polarization ellipse parameters were analyzed during the closest approach of the transmitter. Ideally, the instrument would be receiving a purely azimuthal-mode electric field, and it can be assumed that the polarization ellipse will be narrow and aligned very nearly parallel to the transmitter (section 2.4.1).

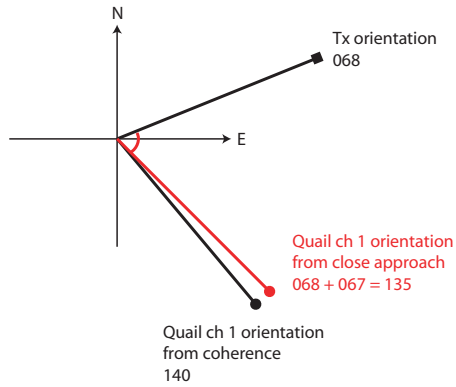

Figure 3.13 Channel 1 orientation estimates for QUAIL; in the closest approach method, it was assumed that the polarization ellipse was aligned with the transmitter, and ellipse orientation was then used to infer instrument orientation.

	Geodetic Orientation of Channel 1 (Instrument N)		
	coherence	**closest approach**	**used in processing**
GALAH OBEM	080	085	080
TREVOR ELF	095	111	100
CROC OBEM	030	045	040
NODDY ELF	225	195	225
PLATYPUS OBEM	045	035	040
RHONDA ELF	255	253	255
BANDICOOT OBEM	ambiguous	069	070
QUAIL ELF	140	135	140

Table 3.3 Perimeter instrument orientation estimates.

Applying this method to QUAIL (Figure 3.12) indicates that it is not so clear-cut in practice (the processing routines used are described in section 3.4.2). Ideally, the closest approach would coincide with the maximum value of P_{MAX} and a minimum in P_{MIN}. Empirically, the P_{MAX} maximum, the closest approach, and both of the P_{MIN} minima (two minima suggesting a bit of "wag" in the transmitter antenna) all occur at different times within

a forty-minute period. In addition, the ellipse orientation changes rapidly in this interval. Choosing the minimum source-receiver range, the two estimates of QUAIL channel 1 orientation land only 5° apart (Figure 3.13). Results for all the instruments are summarized in Table 3.3; for most, the P_{MAX} maximum, P_{MIN} minimum, and closest approach line up more closely, and there is only one minimum in P_{MIN}.

3.4 Data Processing

3.4.1 Development of the Processing Code

SFT6 is a Matlab-based generalized CSEM processing routine written by the author of this dissertation. It is based on CSEM processing techniques used in earlier academic experiments [Constable and Cox, 1996; MacGregor, 1997]. Its name is an ad-hoc designation, it being the sixth version of a routine based on the "slow Fourier transform". Earlier versions of the code (one through five) were hardwired for use with the APPLE data set, just as its academic predecessors were for their particular data sets.

A beneficial development occurred when the author was working as an at-sea consultant on the first industrial CSEM data acquisition cruises. The algorithm had to be adapted to handle arbitrary data sets and equipment upgrades, and the source code heavily commented for use by third parties. Because the basic routines were written while working under NSF funding, these codes are freely available, and are at the core of software that has been used to process hundreds of industry data sets to date.

The advantages of freely sharing the code with industry partners is that it has been thoroughly de-bugged, and its results compared against some of the most advanced proprietary modeling codes available. The APPLE data set was re-processed using SFT6, and the code has been used to process subsequent data sets collected by the SIO EM Laboratory.

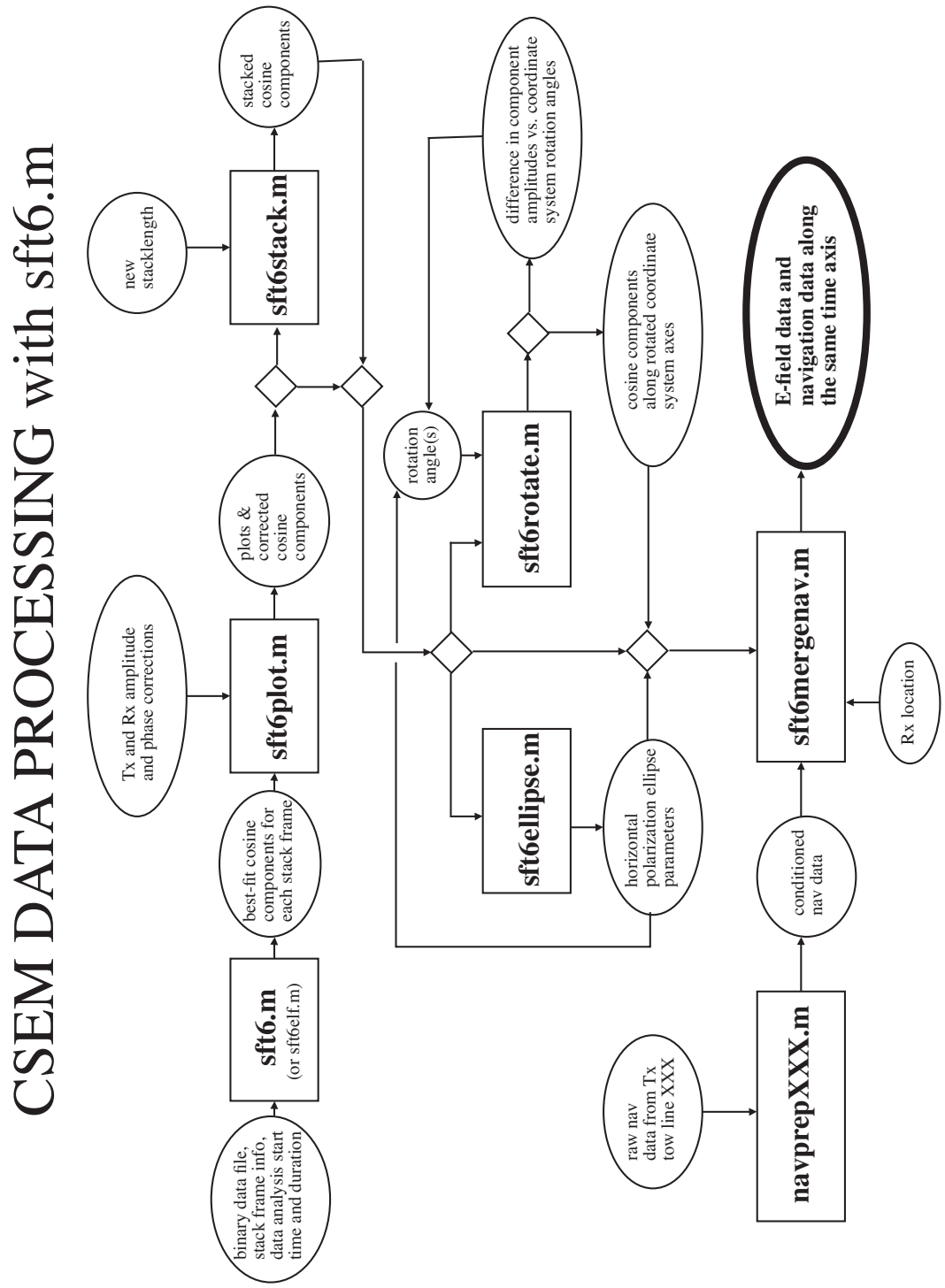

Figure 3.14 The sft6 processing routine is modular.

3.4.2 Components of SFT6

SFT6 consists of several modules (Figure 3.14); individual executable scripts that load data, perform their particular mathematical operations, plot the results, and save the modified data to a new file. This modular structure allows the processor to compare different approaches to handling the data, and to isolate technical issues.

3.4.2.1 sft6 (and sft6elf): initial processing

The first routine begins by loading the raw time series data recorded by the receivers. Short segments of the time series ("stack frames") are transformed in sequence. Stack frames were 120 seconds for APPLE data processing, which is roughly the amount of time it takes for the transmitter to move one transmitter-length. Longer stacks were generated by averaging the transformed data from these initial frames (section 3.4.2.3).

Typically, the fundamental transmission frequency and its harmonics are queried, but other applications may arise: the frequency search described in section 3.2.3, for example, or investigations of spurious instrument noise.

A continuous sinusoid *d(t)* of angular frequency $\omega = 2\pi f$ and arbitrary phase offset from $t = 0$ can be represented as the sum of two orthogonal harmonic basis functions, scaled by coefficients:

$$A\cos(\omega t) + B\sin(\omega t) = d(t)\,. \tag{3.5.1}$$

When *d(t)* is the discrete electric field data stack frame time series vector **d** (Figure 3.15), it contains oscillations at a wide range of frequencies. Thus, for any particular frequency $\omega_j = 2\pi f_j$ the system of equations

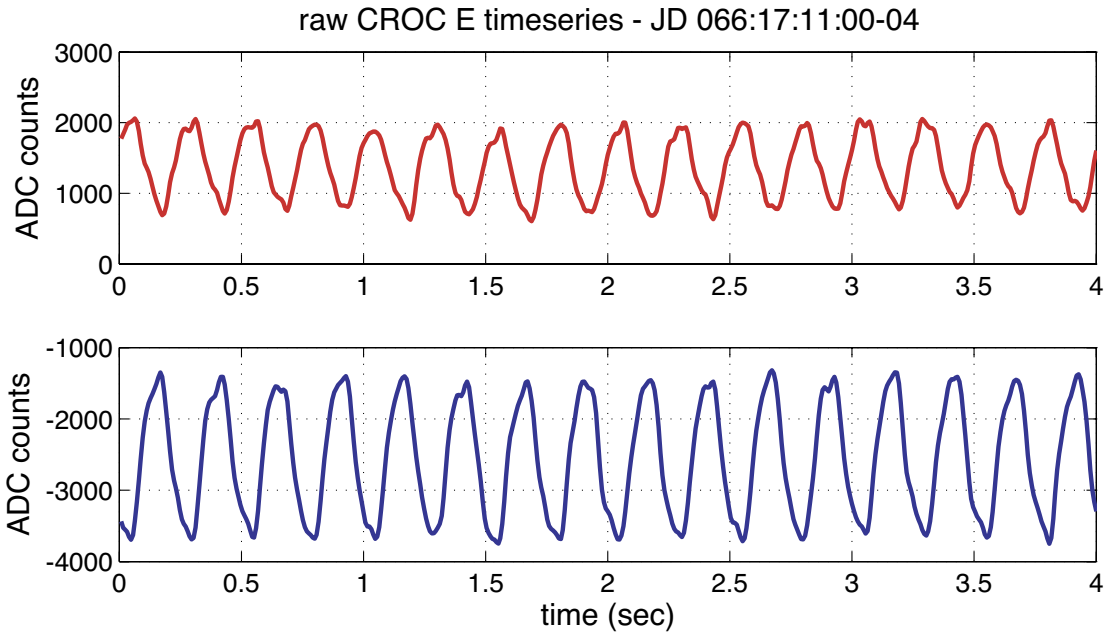

Figure 3.15 High SNR electric fields measured by OBEM CROC on orthogonal channels 1 (red) and 2 (blue); $f_S = 125$ Hz.

$$\begin{bmatrix} \cos(\omega_j t_1) & \sin(\omega_j t_1) \\ \cos(\omega_j t_2) & \sin(\omega_j t_2) \\ \vdots & \vdots \\ \cos(\omega_j t_n) & \sin(\omega_j t_n) \end{bmatrix} \begin{bmatrix} A_j \\ B_j \end{bmatrix} = \begin{bmatrix} d_1 \\ d_2 \\ \vdots \\ d_n \end{bmatrix} \tag{3.5.2}$$

is overdetermined and thus no exact solution for the coefficients exists. A linear least-squares method is used to solve for the "best fit" coefficients: equations (3.5.2) can be written as

$$\mathbf{MC} = \mathbf{d} \tag{3.5.3}$$

where **M** is the basis function matrix, and **C** is the coefficient vector. A QR factorization algorithm is applied to **M** to find an orthogonal matrix **Q** and an upper triangular matrix **R** such that

$$\mathbf{M} = \mathbf{QR} \,. \tag{3.5.4}$$

Substitution back into (3.5.3) and multiplication of both sides by $\mathbf{Q}^{\mathbf{T}}$ yields

$$\mathbf{RC} = \mathbf{Q}^{\mathbf{T}}\mathbf{D} \,. \tag{3.5.5}$$

Equation (3.5.5) can be solved linearly for **C**, which now contains the coefficients $\tilde{A}, \tilde{B}$ that minimize the L^2 norm of the misfit:

$$\| \mathbf{MC} - \mathbf{d} \|_2 = \sqrt{\sum_i \left(\left[\tilde{A}_j \cos \omega_j t_i + \tilde{B}_j \sin \omega_j t_i \right] - d_i \right)^2} \,. \tag{3.5.6}$$

The "least-squares fit" to equations (3.5.2) has been found. In practice, the MATLAB backslash operator was used to call the factorization routine. These coefficients are used to characterize the amplitude and phase of the signal at that particular frequency ω_j:

$$\tilde{d}_{i,j} = \left(\sqrt{\tilde{A}_j^{\,2} + \tilde{B}_j^{\,2}} \right) \cos\left(\omega_j t_i - \tan^{-1} \frac{\tilde{B}_j}{\tilde{A}_j} \right) = \left| E_j \right| \cos\left(\omega_j t_i - \varphi_j \right) \tag{3.5.7}$$

where $|E|$ is the amplitude and φ is the phase of the least-squares fit sinusoid $\tilde{d}(t)$. Phase is relative to the start of the stack frame, and lag is positive.

The data loggers stored several hours worth of data in RAM memory before writing it all to a hard disk drive mass storage device over the course of a minute or two. While the hard drive is active, it creates a significant amount of noise in the system due to increased power consumption and the electromagnetic field created by a spinning magnetic disk. Coefficients from these stack frames are set to NaN (Not a Number) and ignored by subsequent modules. Length of the disruption depends on instrument generation. The newest carry flash memory instead of hard drives, diminishing noise during disk writes.

Data are converted from counts to Volts via the least count of the analog-to-digital converter; data are then normalized by the receiver's antenna length and nominal gain to give electric field amplitude in Volts per meter. Antenna lengths for APPLE were 10 m on the perimeter instruments and 177 m on the LEMs; all had a gain of 10^6.

The receivers carried internal clocks. They were synchronized with GPS time shortly before deployment, and the OBEM clocks were compared against GPS time again upon recovery. Drift was on the order of a few milliseconds per day. Assuming a linear drift, the phase of each stack frame was adjusted by a cumulative factor to remove the effect. This correction made a significant difference in the combined LEM data, in which the two components of the same virtual instrument had separate clock drifts. With no absolute transmitter phase information, however, it was not very important for the perimeter receiver data.

The final step in sft6 is to save the coefficients to a binary file. The ELF loggers and the OBEM loggers created binary data in different formats; sft6elf was modified from sft6 to handle raw time series with the ELF format; the least-squares fitting algorithms and output file formats are identical.

3.4.2.2 sft6plot: equipment-specific adjustments

This routine loads in the output of sft6 and applies equipment-specific adjustments before plotting the data from each channel. Data are normalized by the transmitter source dipole moment and adjusted to remove the receiver amplifier transfer function (Figure 3.16). If the transmitter phase is known, absolute phase shift may be computed here as well.

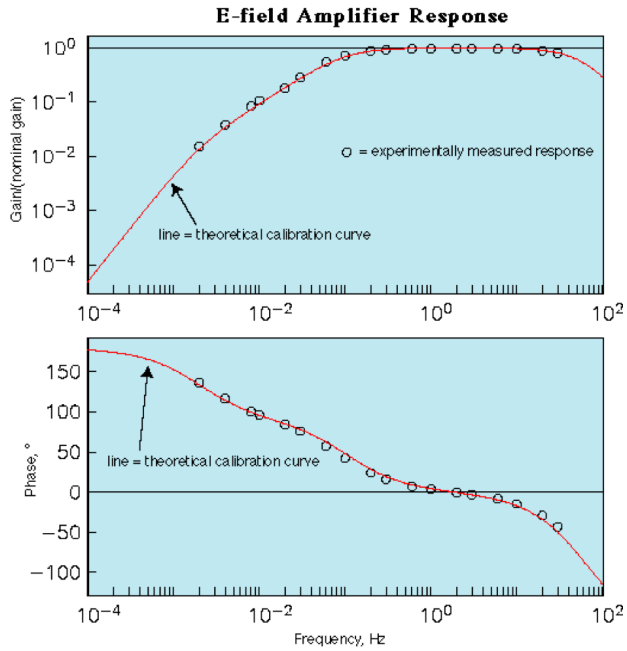

Figure 3.16 The complex transfer function of the E-field amplifier (figure courtesy S. Constable). Several of the calibrations plotted here were run by the author in a cold room at 1°C to simulate deep-sea temperature conditions.

Plotting the data from LEMs KOALA and ROO (Figure 3.17), transformed at 3.9889 Hz, the phase data indicate an abnormality. At this high of frequency (where natural source fields are extremely weak), phase should be coherent when the transmitted signal is being detected, and random otherwise. During the two halves of the large circular tow (when range and azimuth are nearly constant), phase should be nearly constant for KOALA (aligned N/S), and switch polarity halfway through on ROO (E/W). In reality, "phase wrapping" was observed, which is to be expected if the queried frequency is slightly different from the true transmitted frequency (estimated in section 3.2.3).

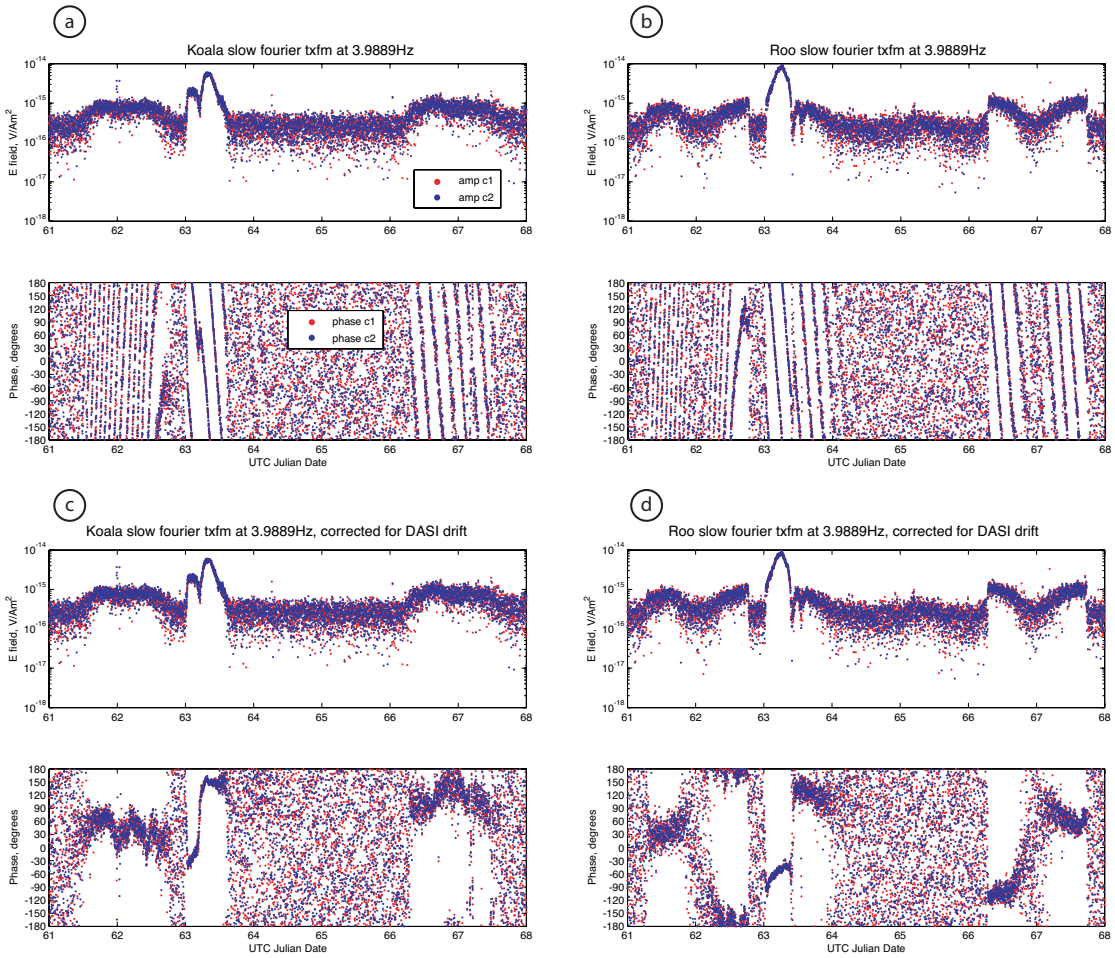

Figure 3.17 Electric fields measured by LEMs (a,c) KOALA and (b,d) ROO at the fundamental transmission frequency of 3.9889 Hz throughout the duration of the experiment, processed using stack frames of 120 seconds, normalized by the source dipole moment and adjusted for receiver dipole length, clock drift, and amplifier response. (a,b) "Phase wrapping" caused by transmitter clock drift was (c,d) removed.

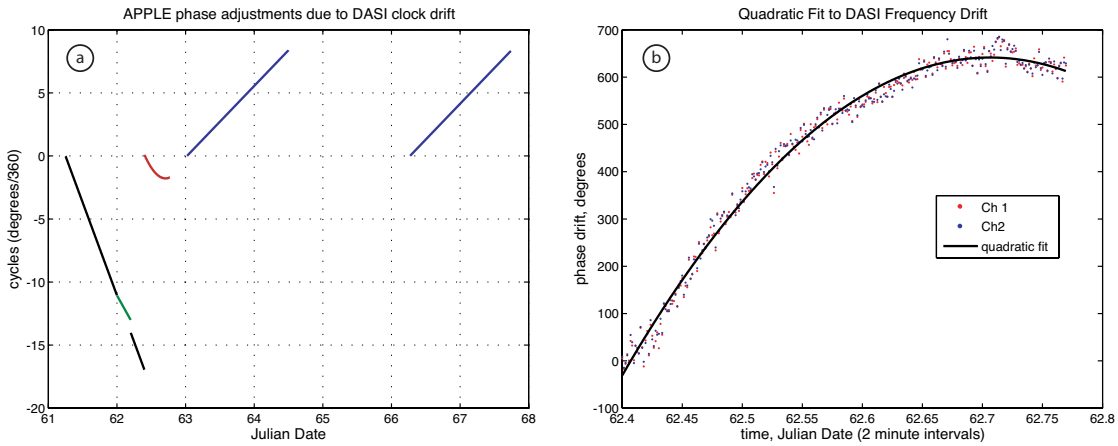

Figure 3.18 A phase adjustment (a) was applied to all of the data processed for CSEM analysis. (b) A quadratic function was used to fit one portion of the phase drift trend.

In order to coherently stack the data into longer stack frames (section 3.4.2.3), this phase wrapping had to be remedied to avoid phase cancellation. If it had been just a matter of refining the transmission frequency estimate, the observed phase wrapping would have had a constant sign and nearly constant slope throughout the experiment. This was not the case: the transmission frequency varied during the experiment, so time-specific cumulative phase adjustments were made instead (Figure 3.18). The frequency mismatch was 1.71×10^{-4} Hz during the west circle tow, and 6.56×10^{-5} Hz otherwise. A higher-order component to the drift was observed during the second half of JD 062, which was fit to a quadratic function by least squares and incorporated into the phase adjustment. The resultant phase values are much steadier (Figure 3.17 c,d), and the amplitudes are unaffected. These same phase adjustments were applied to every channel of every instrument during processing.

This module also allows the electric field data to be "pushed" by a constant offset along the time axis. ELF TREVOR's electric field time series was out of alignment with the navigational data by 13440 seconds = 224 minutes. Each ELF diskwrite contains 32 minutes

of data; the misalignment was exactly 7 diskwrites long, indicating that, at some point earlier in the deployment, the logger was unable to draw enough current from the batteries to power up the hard drive – possibly due to passivation of the lithium batteries, known to occur on occasion. In this instance, it was perfectly acceptable to "push" the time series into alignment.

3.4.2.3 sft6stack: stack frame length

This module computes the coefficients of longer stack frames by finding the mean coefficient values of a contiguous series of shorter stack frames.

The amplitude of the transform misfit at frequency ω_j is the bias-corrected standard deviation between the least squares fit sinusoid and the original data vector:

$$s_{N-1}(j) = \sqrt{\frac{\sum_{i=1}^{N}\left(\tilde{d}_{i,j} - d_i\right)^2}{N-1}} \,. \tag{3.5.8}$$

In the presence of normally distributed stationary noise, a longer stack frame yields a smaller normalized variance, and thus a lower effective noise "floor". Transmitted field data that lie below the noise floor cannot be recovered. If the stack frame length N is increased by a factor η, the noise floor is lowered by a factor $\sim\sqrt{\eta}$.

For a stationary transmitter-receiver pair, N is only limited by the amount of time the transmitter was switched on. For APPLE (and all modern CSEM surveys), N was limited by the dynamic nature of the source-receiver geometry – the navigational parameters are "smeared out" over the stack frame. Another concern is phase cancellation – if the phase shift within the stack frame is more than a few degrees, the transformed amplitude will be artificially decreased. For APPLE, phase cancellation did not present a serious problem, since the phases were artificially smoothed (section 3.4.2.2).

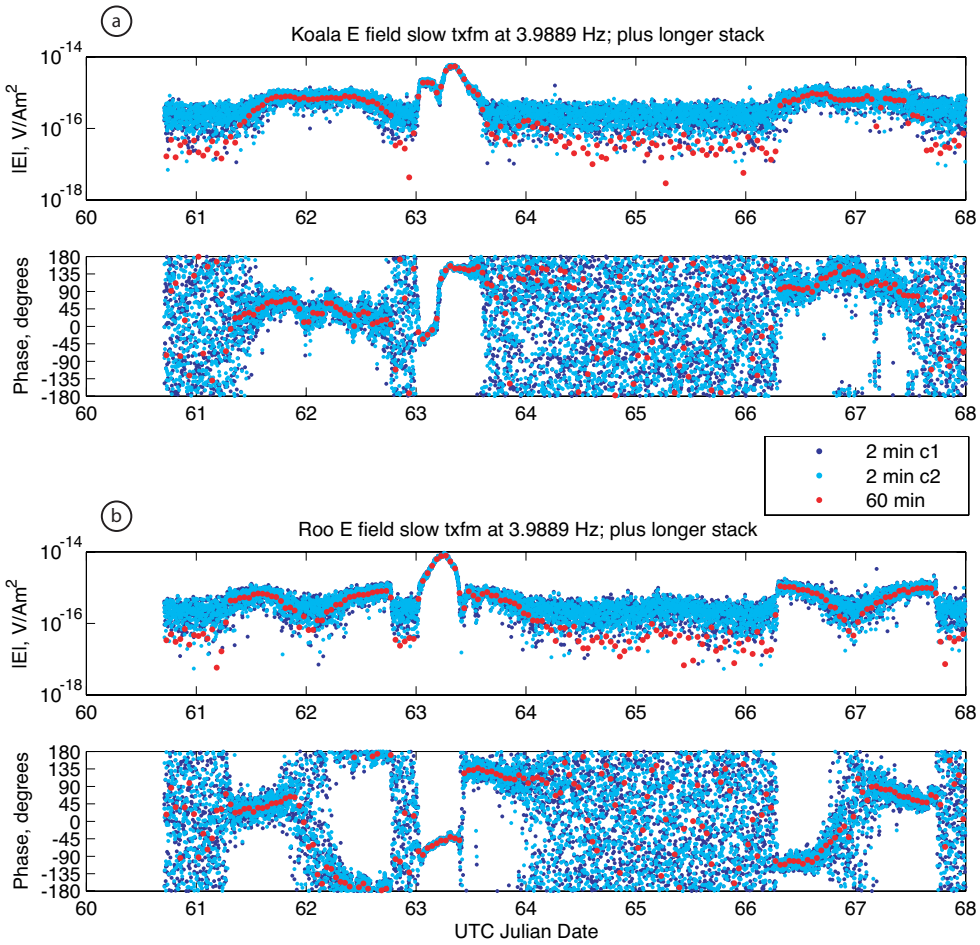

Figure 3.19 Processing the data from (a) KOALA and (b) ROO with longer stack frames lowers the effective noise floor; since these were LEMs,, the two parallel channels were stacked together as well. Because the phase was stabilized (section 3.4.2.2), stack frames of 60 minutes are still brief enough to preserve amplitude measurements when the signal-to-noise ratio is large.

Stack frame lengths for the short-range, radial-mode perimeter instrument data were 20 minutes. For the LEM data, they were set to 60 minutes, except at the very longest ranges, where two stacks of 150 minutes were used. Data from ELF QUAIL recorded during the semicircular tow were stacked at 60 minutes length; the ~15 km ranges were too near the 20 minute stack noise level (QUAIL, unfortunately, was among the noisiest of the instruments deployed, but the significance of its data was an unforeseen consequence of having to tow directly into the wind during inclement weather, which resulted in the semicircular tow).

Figure 3.19 illustrates the benefit of combining stack frames of 2 minutes into frames of 60 minutes on the LEM instruments: longer range data became available, while short range data amplitudes were preserved.

When processing LEM data, the two parallel electrode pairs are stacked together, further reducing the noise level. The mean value of each coefficient was computed.

3.4.2.4 sft6ellipse: polarization ellipse parameters

Horizontal electric field polarization ellipse parameters (section 2.3.6) are computed for each stack frame from the calculated coefficients. Orthogonal components are required; data from the OBEM LEMs were combined in this step (Figure 3.20). Ellipse parameters are a function of the relative phase between components. The universal phase adjustments applied in sft6plot and lack of absolute phase data, therefore, did not affect the ellipse parameter estimates.

The ellipse orientation datum α_N (ranging from -90° to 90°) is the angle positive clockwise from instrument north (Channel 1, or geodetic north for LEMs) to P_{MAX}; it was used to estimate perimeter receiver orientation in section 3.3.1.2

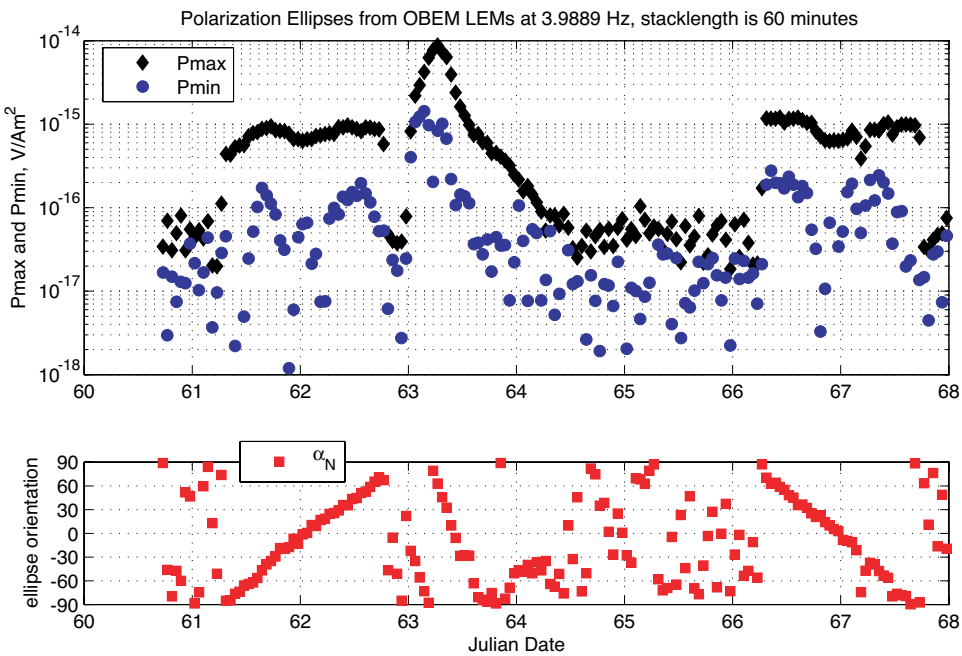

Figure 3.20 The size and orientation of the horizontal electric field polarization ellipse was computed for each stack frame.

3.4.2.5 sft6rotate: component rotation

This module reads in the coefficients, computes the complex E-field components (E_1, E_2) for each stack frame, rotates the horizontal coordinate system counterclockwise by an angle ψ, and calculates the components (E_x, E_y) in the new coordinate system (Figure 3.21). The equations used are:

$$\begin{aligned}
\mathrm{Re}(E_x) &= \mathrm{Re}(E_2)\sin\theta + \mathrm{Re}(E_1)\cos\theta \\
\mathrm{Im}(E_x) &= \mathrm{Im}(E_2)\sin\theta + \mathrm{Im}(E_1)\cos\theta \\
\mathrm{Re}(E_y) &= \mathrm{Re}(E_1)\sin\theta - \mathrm{Re}(E_2)\cos\theta \\
\mathrm{Im}(E_y) &= \mathrm{Im}(E_1)\sin\theta - \mathrm{Im}(E_2)\cos\theta
\end{aligned} \tag{3.5.9}$$

where $\theta = \psi - 90°$.

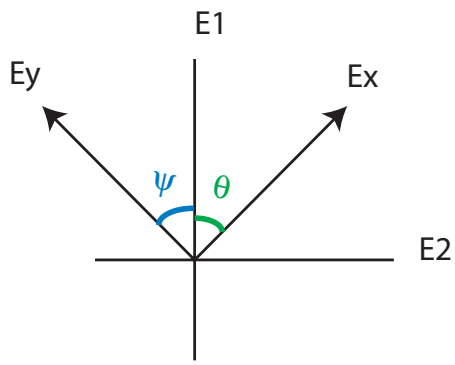

Figure 3.21 Angles used in sft6rotate: ψ is E_1 to E_y, positive counterclockwise; $\theta = 90° - \psi$ is E_x to E_1, positive counterclockwise.

For APPLE, the perimeter instrument data were rotated from their estimated orientations into the principal axes of the observed large circular tow anisotropy (Figure 4.1) for single component analysis (section 4.3.2).

Once α_N is known, the polarization ellipse axis magnitudes (and, more significantly, the phase vales for the components aligned with the ellipse axes) can be computed with this rotation algorithm. Due to the lack of absolute phase data, no information would be added, so the APPLE data were not processed in this way.

3.4.2.6 sft6mergenav: merge E fields with navigation data

The final processing step is to merge the electric field data with the navigation data by aligning their respective time vectors, so that any combination of parameters can be assembled together into arbitrarily formatted data files. The mean position and orientation of the transmitter during each stack frame is used to compute the relative ranges and azimuths.

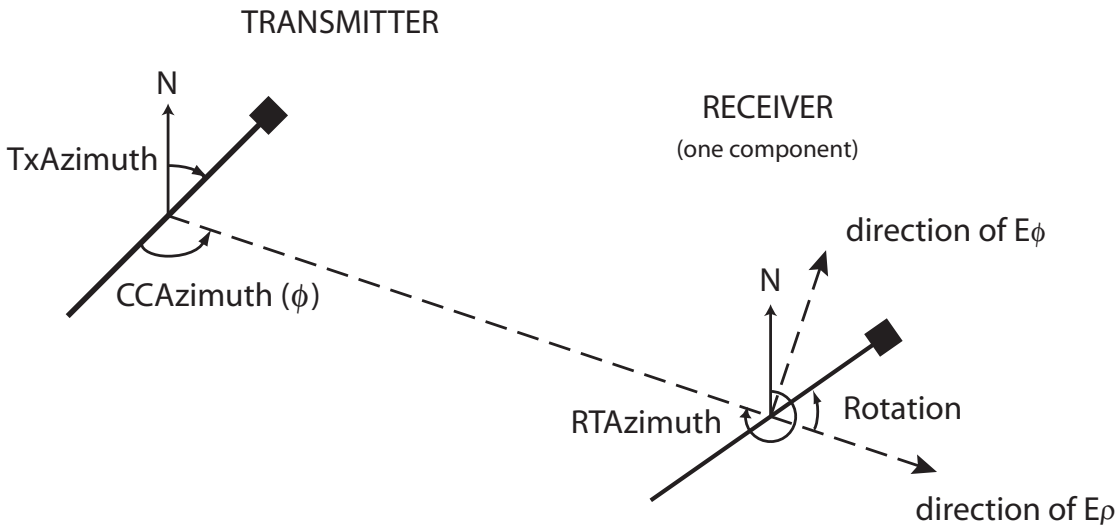

Figure 3.22 Transmitter-centered navigation parameters [adapted from Constable and Cox, 1996], also incorporating a receiver-centered azimuth and a geodetic reference frame.

A transmitter-centered coordinate system [Constable and Cox, 1996] was used to define the merged navigational parameters for isotropic modeling code analysis, while geodetic orientations and a receiver-centered coordinate system (Figure 3.22) were used to prepare data subsets for anisotropic model inversion.

This module can read in electric field data at any point along the processing stream. For APPLE, both polarization ellipse data and single-component data sets (using rotated perimeter instrument data, and/or individual LEM data) were created. Figure 3.23 displays the LEM ellipse data aligned with the navigation data.

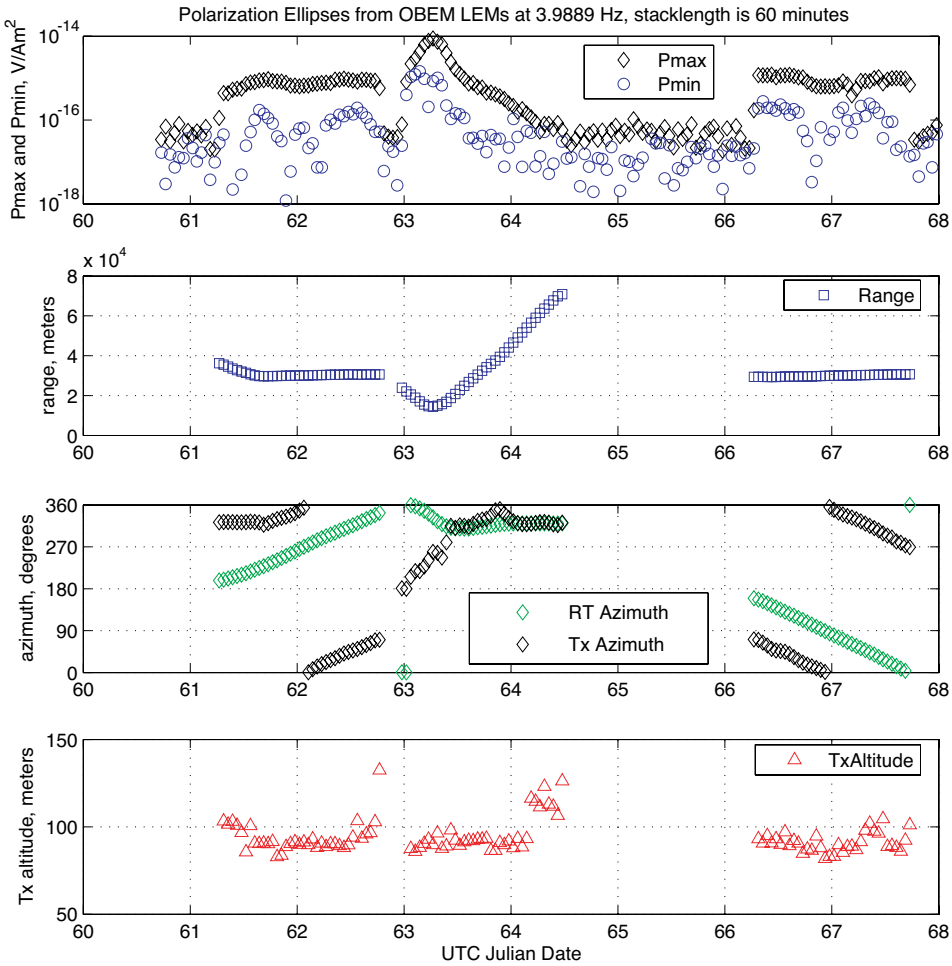

Figure 3.23 The final step in processing: sft6mergenav aligns the electric field and relative navigational data along the same time vector.

3.5 Uncertainty Analysis

Two distinct types of uncertainty occur in CSEM data: navigational uncertainty dominates at short source-receiver offsets, while instrument and environmental noise interferes with the low-magnitude, long-offset data.

3.5.1 Navigational uncertainty

The single most significant source of uncertainty in the data comes from uncertainty in transmitter location; in section 3.2.2 it was shown that systematic location errors on the order of 100 m were likely. Short-arm receivers were estimated to have drifted ~150 m laterally during descent to the seafloor (section 3.3.1.2), adding to the geometric uncertainty in the perimeter instrument data.

A forward modeling study was undertaken to test how this navigational uncertainty affects the electric field data. Using the 1-D isotropic CSEM modeling code of Flosadóttir and Constable [1996] (section 2.4.1), $|E_\rho|$ and $|E_\phi|$ were computed over four different simplified mature seafloor resistivity models: a 10^3 Ωm halfspace, a 10^4 Ωm halfspace, and both again but with relatively conductive upper crustal layers of 10 Ωm, 1 km thick, between the seawater and the basal halfspaces. Normalized differences in the field magnitudes were computed for differences in range of 100 m and 200 m (Figure 3.24). Data are affected profoundly at close source-receiver offsets, but errors fall below 10% by 5 km, and 5% around 10 km.

For ranges < 5 km, therefore, uncertainty in $|E|$ was set to 25%. The minimum uncertainty for ranges > 5 km was set to 10%.

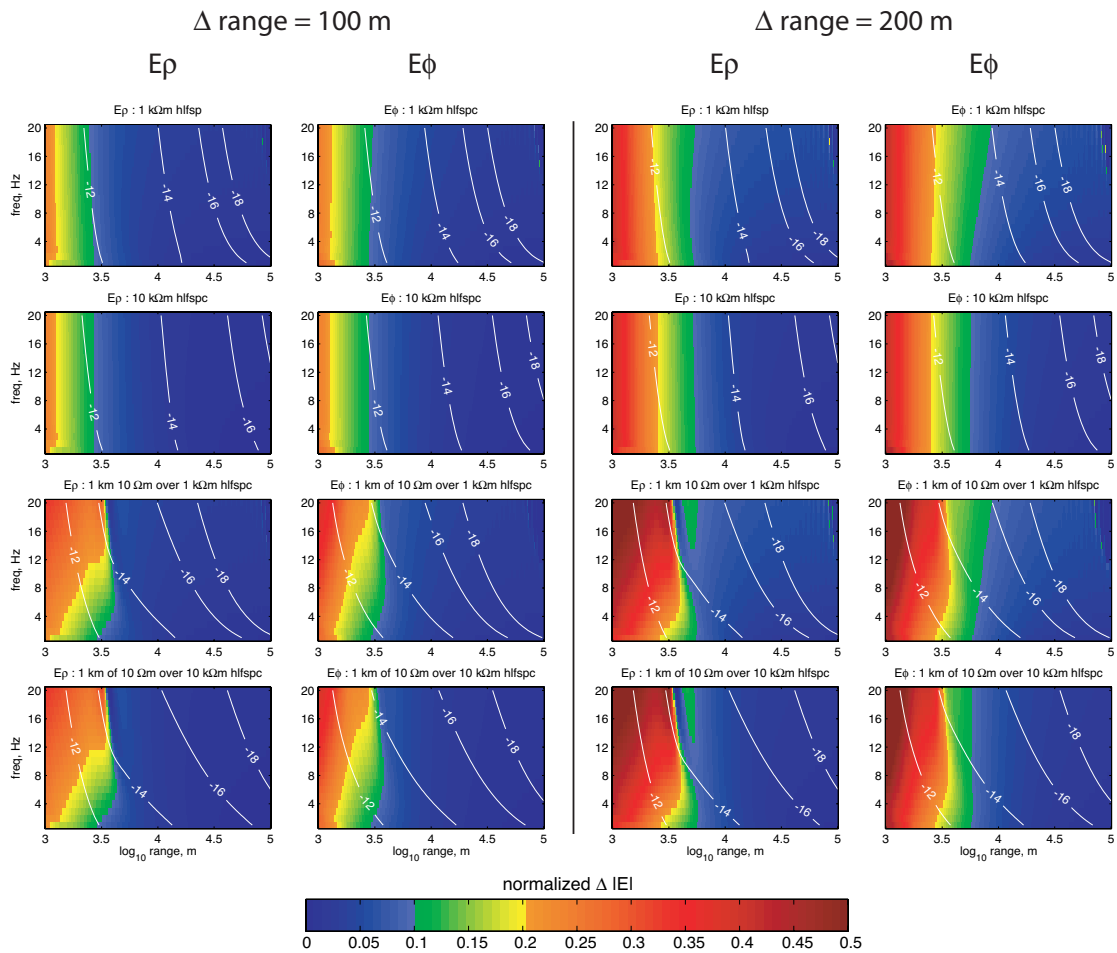

Figure 3.24 Normalized difference in $|E_\rho|$ and $|E_\phi|$ for changes in source-receiver offset of 100 m and 200 m over resistive halfspace models, both without (top) and with (bottom) a conductive upper crust.

3.5.2 sft6noise: ambient noise estimation

Uncertainty stemming from noise in the receiver electronics and the ambient environment is much less problematic than navigation at short ranges, but does create a “noise floor” which adds scatter to, and ultimately overwhelms, data at the long ranges.

Due to stormy weather that prevented transmitter operation, the CSEM instruments collected 42 hours of continuous ambient electric field data during the experiment, beginning at JD 64.5. These data were processed with sft6, sft6plot, and sft6stack. Another module, sft6noise, was developed to read in the estimated components and perform statistical analyses of the real and imaginary parts of the complex fields, following the method of Evans [1991].

In sft6noise, the mean value μ_m and bias-corrected sample standard deviation s_{N-1} are computed for both parts of complex field individually for each stack frame. The Kolmogorov-Smirnov test for normalcy is applied at the 5% significance level: the KS statistic is the maximum deviation of the empirical cumulative distribution function (cdf) from a normal cdf with the measured μ_m and s_{N-1}; if the KS statistic is less than the critical value of the 5% significance level, the data pass the test (data underlain by a truly normal distribution will, theoretically, fail this test only 5% of the time).

The noise data are checked to see if their (normal) distributions were centered about μ_m:

$$\mu_m < \frac{2s_{N-1}}{\sqrt{N}} . \tag{3.6.1}$$

An F-Test at the 95% confidence level is also performed; if the data pass this test, the ratio of the real to imaginary component variances is close enough to 1.0 that the two distributions can be assumed to be the same, and thus the mean of the two standard deviations is used to represent the amplitude of the noise in that data [Evans, 1991].

Each channel of each perimeter receiver was analyzed (Figure 3.25 and Figure 3.26), as were both pairs of LEMs (Figure 3.27), channels combined. Statistical test results (Table 3.4) indicate that the ambient noise, as recorded by the receivers, is indeed random and normally distributed, and that both the real and complex parts have the same underlying distribution. This was not the case for earlier versions of the ELF instruments [Constable, pers. comm.].

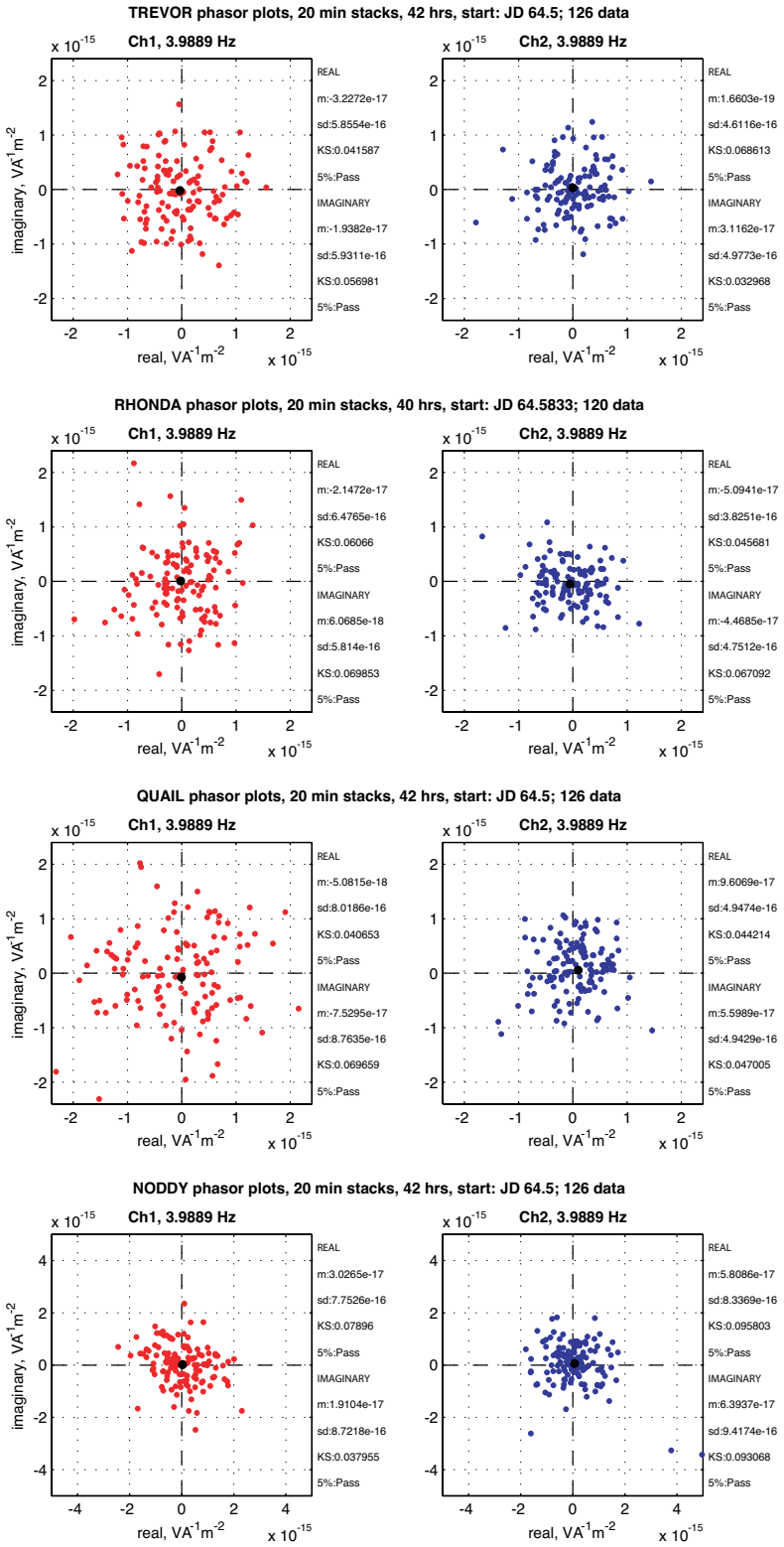

Figure 3.25 Perimeter ELF ambient noise phasor plots. Scale change for NODDY.

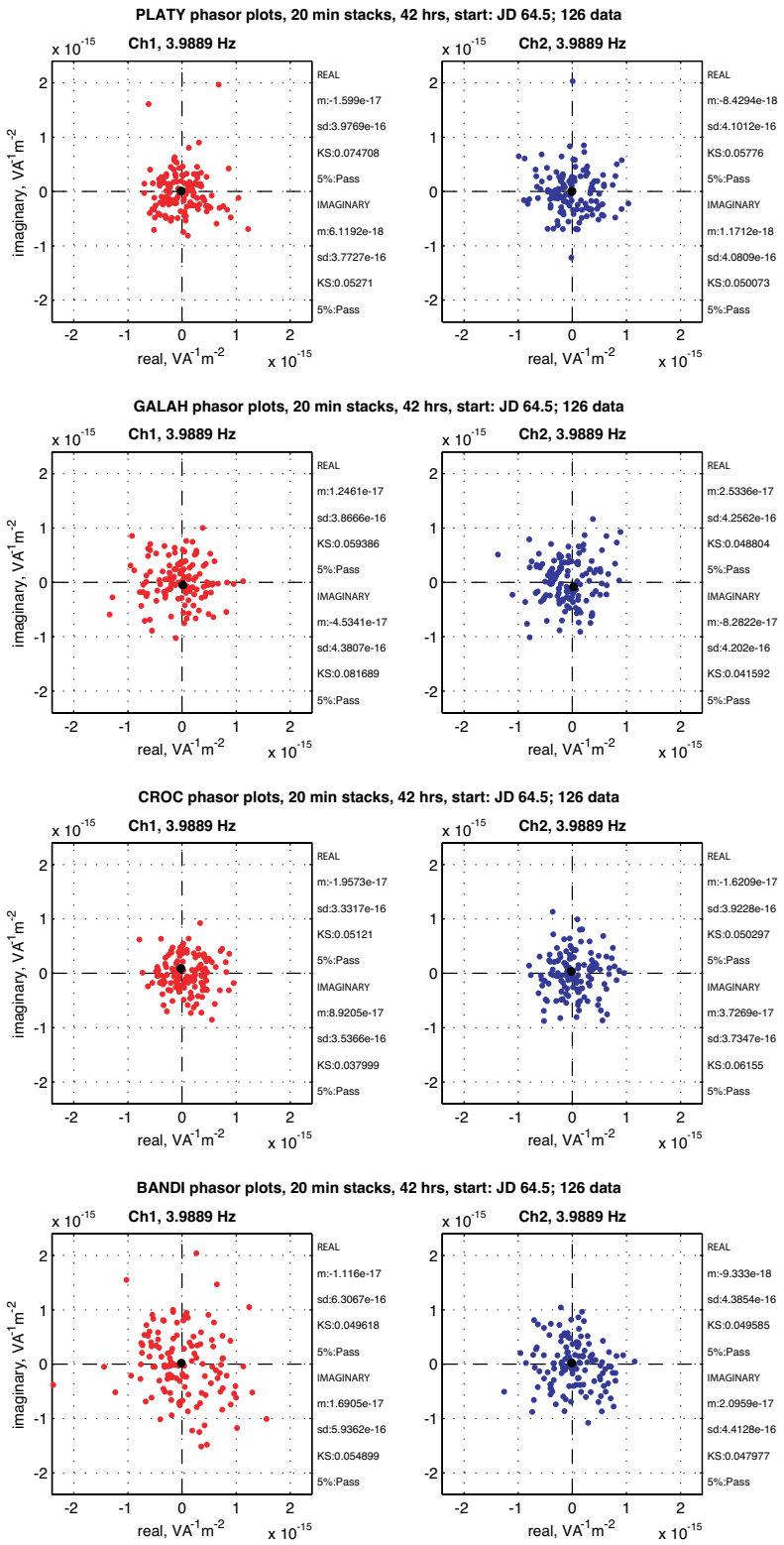

Figure 3.26 Perimeter OBEM ambient noise phasor plots.

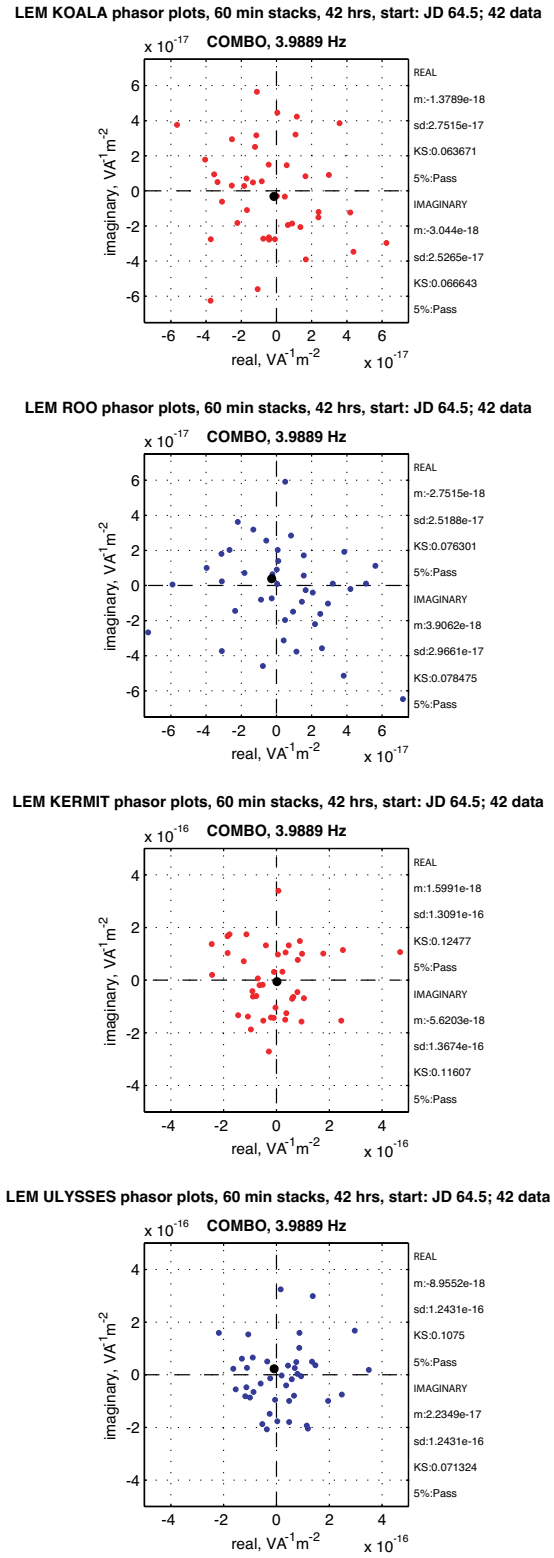

Figure 3.27 LEM combined-channel ambient noise phasor plots. Note change in scale.

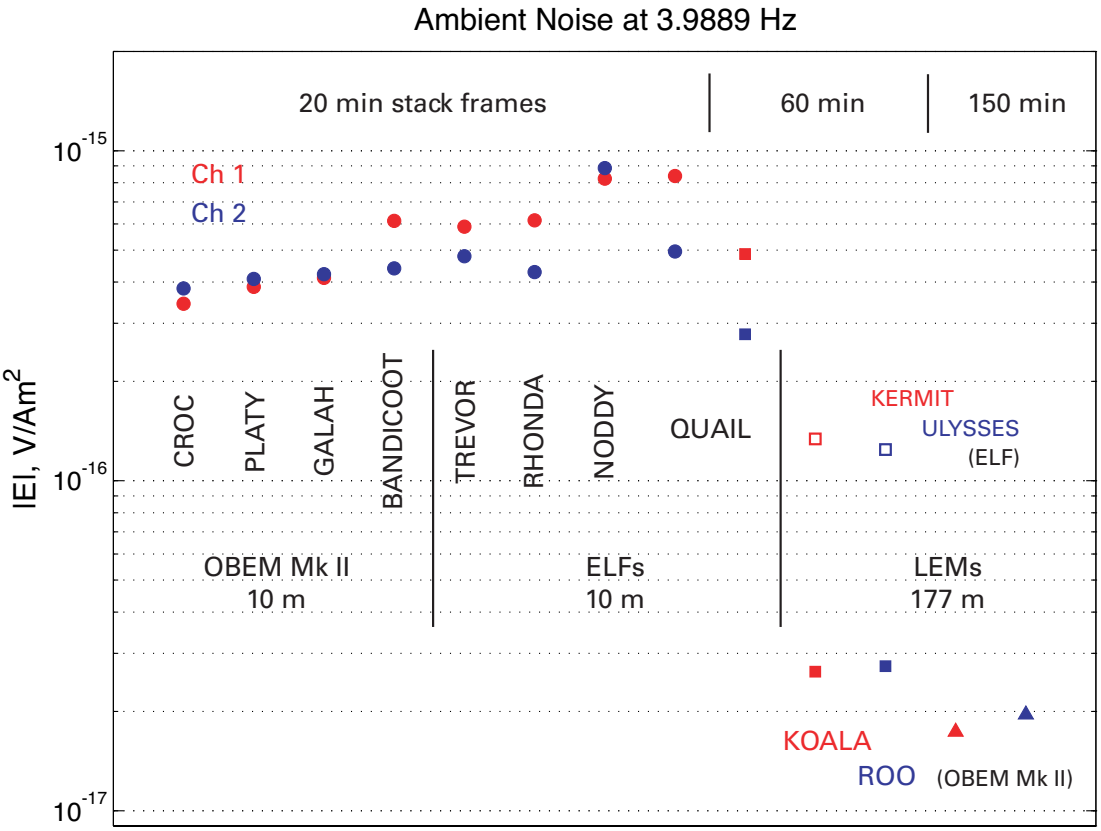

Figure 3.28 The mean ambient noise on each channel for each of the instruments at the stack frame lengths used to process their data.

For the two-component instruments, the greater of the mean s_{N-1} values was used as the noise floor value (Figure 3.28) for both the polarization ellipse data and single-component rotated data.

The ELF LEMs were significantly noisier than the OBEM Mk II LEMs, and so the ELF LEM data were not used in subsequent analysis. ROO was slightly noisier than KOALA, so its s_{N-1} was used to determine the noise level for the LEM polarization ellipse parameters. Respective individual noise levels were used for the single-component LEM data.

		KS Test (5%)	Centeredness	F-Test (95%)
ELF	**RHONDA**	PASS	PASS	FAIL: Ch 2
	QUAIL	PASS	FAIL: Ch 2 Re	PASS
	TREVOR	PASS	PASS	PASS
	NODDY	PASS	PASS	PASS
OBEM Mk II	**PLATYPUS**	PASS	PASS	PASS
	BANDICOOT	PASS	PASS	PASS
	GALAH	PASS	PASS	PASS
	CROC	PASS	FAIL: Ch 1 Im	PASS
LEM (OBEM Mk II)	**KOALA**	PASS	PASS	PASS
	ROO	PASS	PASS	PASS

Table 3.4 Results of statistical tests on ambient noise.

Data were rejected for signal-to-noise ratios below two. Within an order of magnitude of the noise floor, the ratio of noise level to signal level was used to determine the uncertainty.

Because the source field decays exponentially with increasing range, data were inverted in the log domain (chapter 4). Their uncertainties were converted into the log domain, as well. Using the derivative of the $\log_{10}$ function,

$$\frac{\partial\left(\log_{10} x\right)}{\partial x} = \frac{1}{x\ln(10)} \approx \frac{0.4343}{x} \tag{3.6.2}$$

symmetric error bars were generated (*e.g.* for an uncertainty of 10%, $\partial x = 0.1x$ and $\partial\left(\log_{10} x\right) \approx 0.04343$). Because ∂x is non-infinitesimal, this is an approximation: lower error bars are shorter and upper error bars are longer than those of a direct value-by-value conversion in order to make them equivalent on a $\log_{10}$ scale.

3.5.3 Outliers

Obvious outliers were removed manually when encountered. This was necessary for data collected by several different instruments when signal-to-noise ratio grew small. BANDICOOT recorded short (< 5 minute) spikes of noise at irregularly spaced intervals. Significant bursts of noise were also recorded by KOALA; these outliers were also removed manually.

For the statistical noise tests, outliers were removed from BANDICOOT's data, and the data analysis window began two hours later on RHONDA than on the rest of the instruments' data to avoid an anomalously noisy segment.

Finally, strong isolated outliers were removed during data inversion, but only in a few cases – which explains the occasional gap in geometric continuity of the data.

3.6 Processed Data Set

Initially, data were processed at the fundamental frequency (3.9889 Hz), the 3rd harmonic (11.9667 Hz) and, from the OBEMs, the 5th harmonic (19.9445 Hz). Ambient noise was statistically analyzed at these higher harmonic frequencies, as well.

With a sampling rate of 32 Hz, the Nyquist frequency of the ELF instruments was 16 Hz. Energy at the 5th harmonic "folds" back over and is mapped onto the 3rd harmonic during data acquisition. Regardless, the observed instability of the transmission frequency is exacerbated at these higher frequencies, rendering the 3rd and 5th harmonic data from the OBEM Mk II instruments unacceptably uncertain. In addition, phase unwrapping adjustments applied to the data (section 3.4.2.2) are multiplied by the harmonic number, and so phase cancellation occurs more readily at higher harmonics. A weaker source dipole moment at higher harmonics restricted the maximum source-receiver offset of these data to ~8 km at the 3rd harmonic, and

~5 km at the 5th – and these short offsets and higher frequencies are where the navigational uncertainty has an enormous effect (Figure 3.24).

While early attempts were made to model them, the higher harmonic data were eventually dropped from consideration.

Thus, the master data set from the CSEM portion of the APPLE experiment consists of fields measured at 3.9889 Hz from: the perimeter instruments during the large circular tow (Figure 3.30), the combined OBEM Mk II LEMs during the long radial tow (Figure 3.31) and large circular tow (Figure 3.29), and 60 minute stack data measured at QUAIL during the semicircular tow (Figure 3.32).

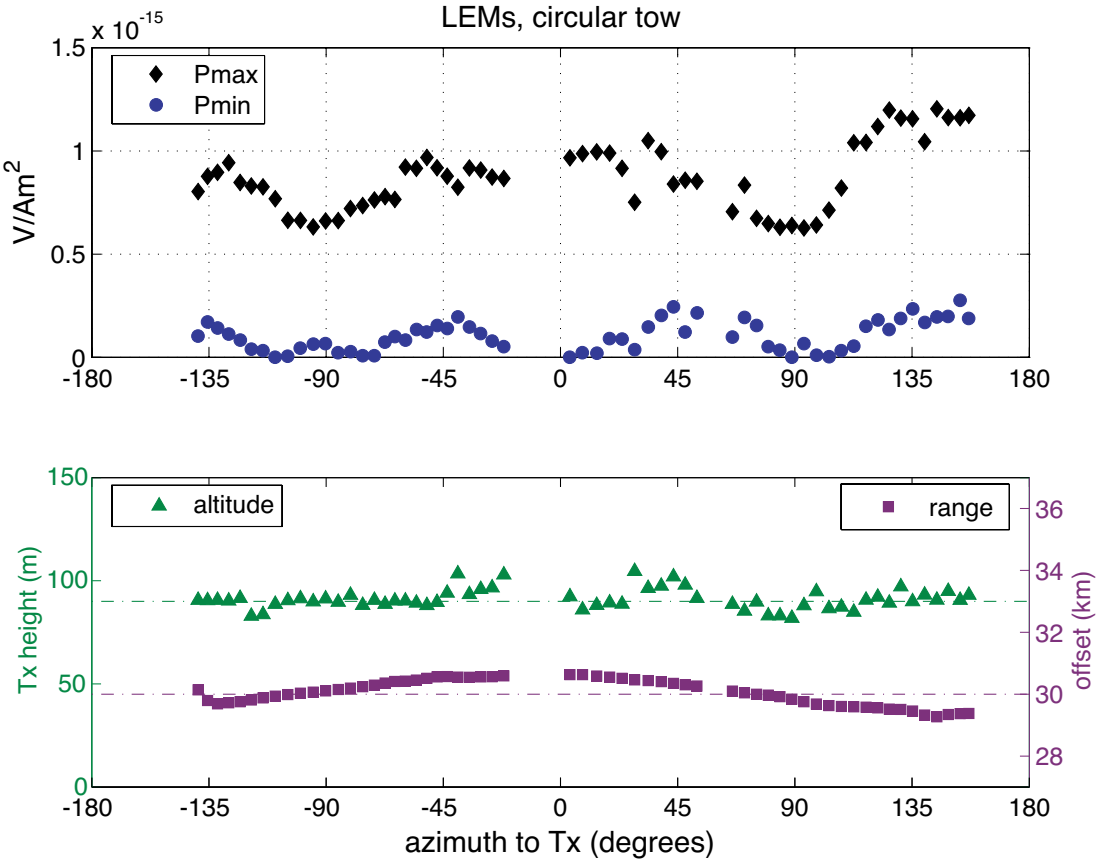

Figure 3.29 Data collected by the LEMs during the azimuthal-mode large circular tow, processed in 60-minute stack frames. (abscissa azimuth is RT Azimuth) The anisotropic pattern observed in the ellipse axes does not correlate with variation in range or Tx altitude.

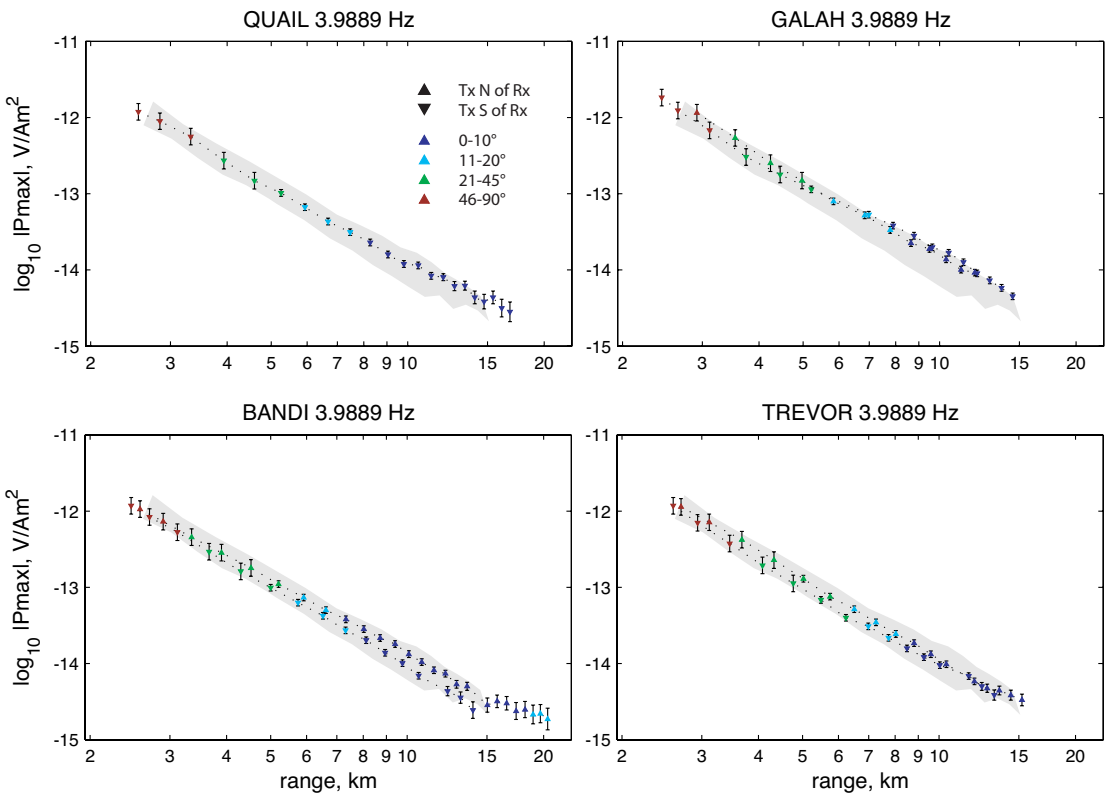

Figure 3.30 The short-offset radial tow P_{MAX} data set from each of the perimeter receivers, recorded during the large circular tow. The grey area indicates the spread in the data across the array, the color of the data point represents its CCAzimuth, with 0° being radial mode and 90° being azimuthal mode. These data were processed using 20-minute stack frames.

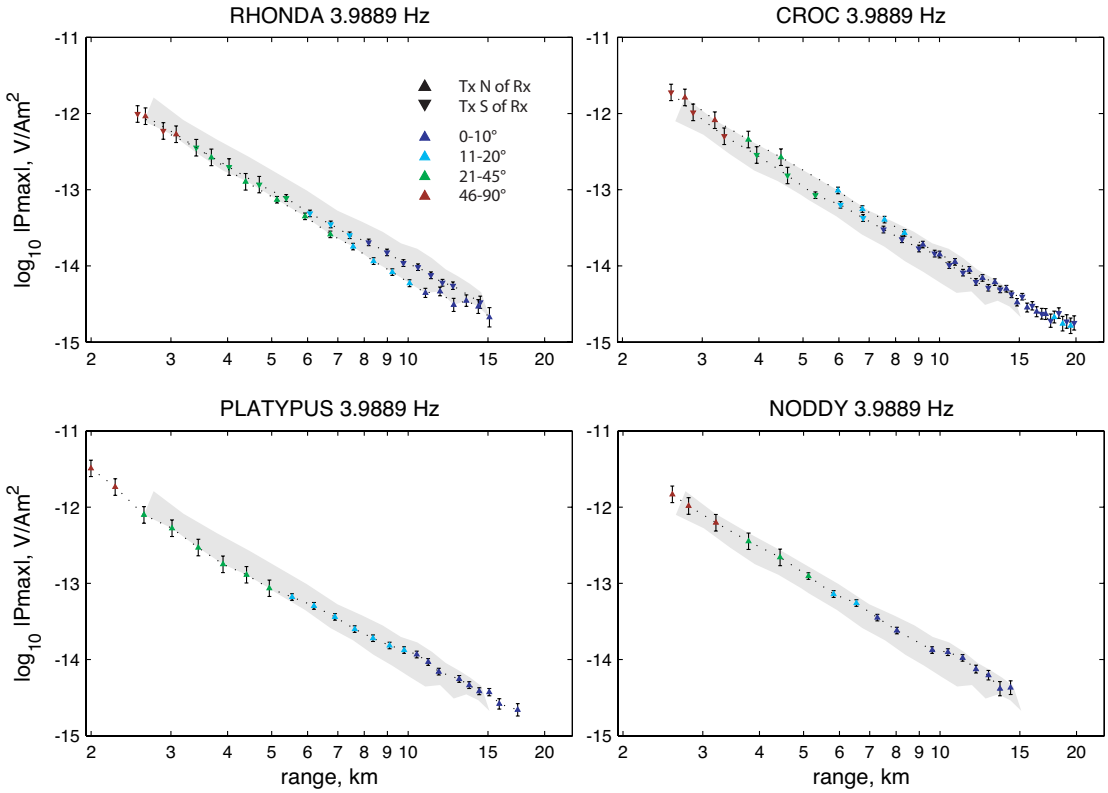

Figure 3.30 (cont.)

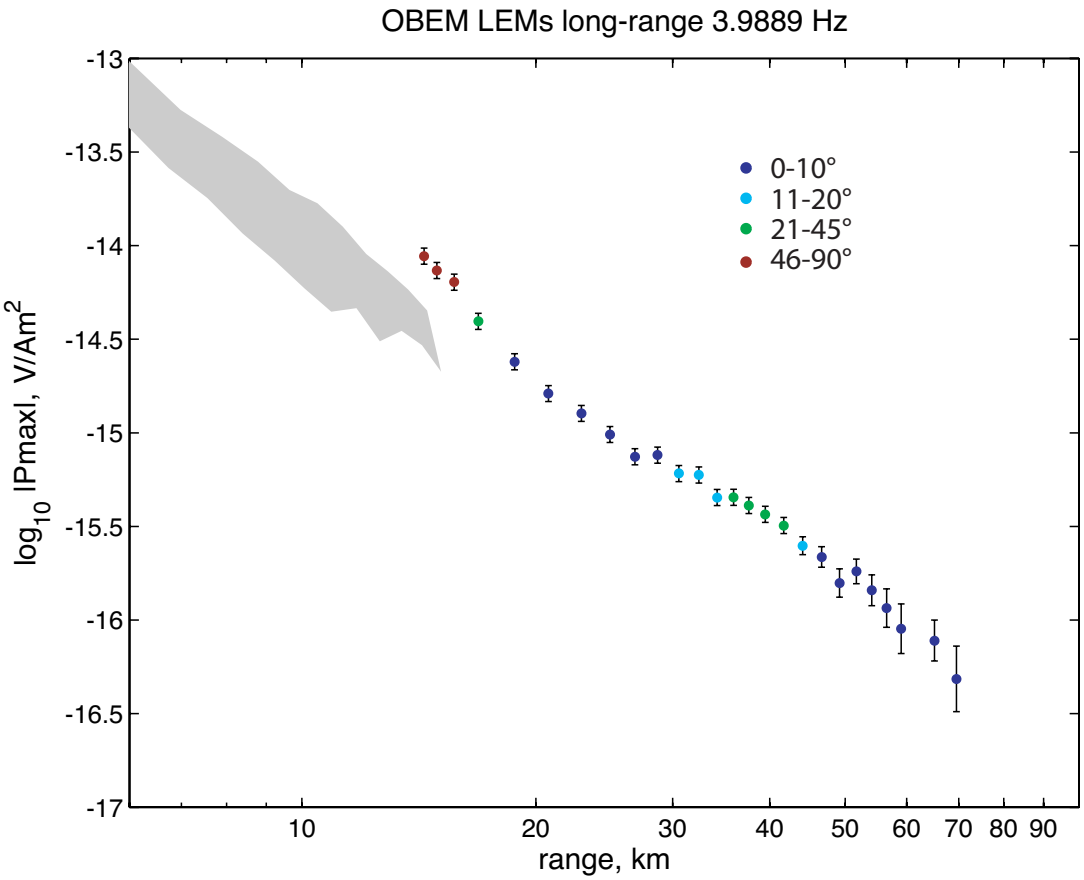

Figure 3.31 Long-offset radial tow P_{MAX} data, recorded by the OBEM Mk II LEMs during the long radial tow of the transmitter. These were processed using 60-minute stack frames, except for the two longest-offset data, which were processed using 150-minute stacks.

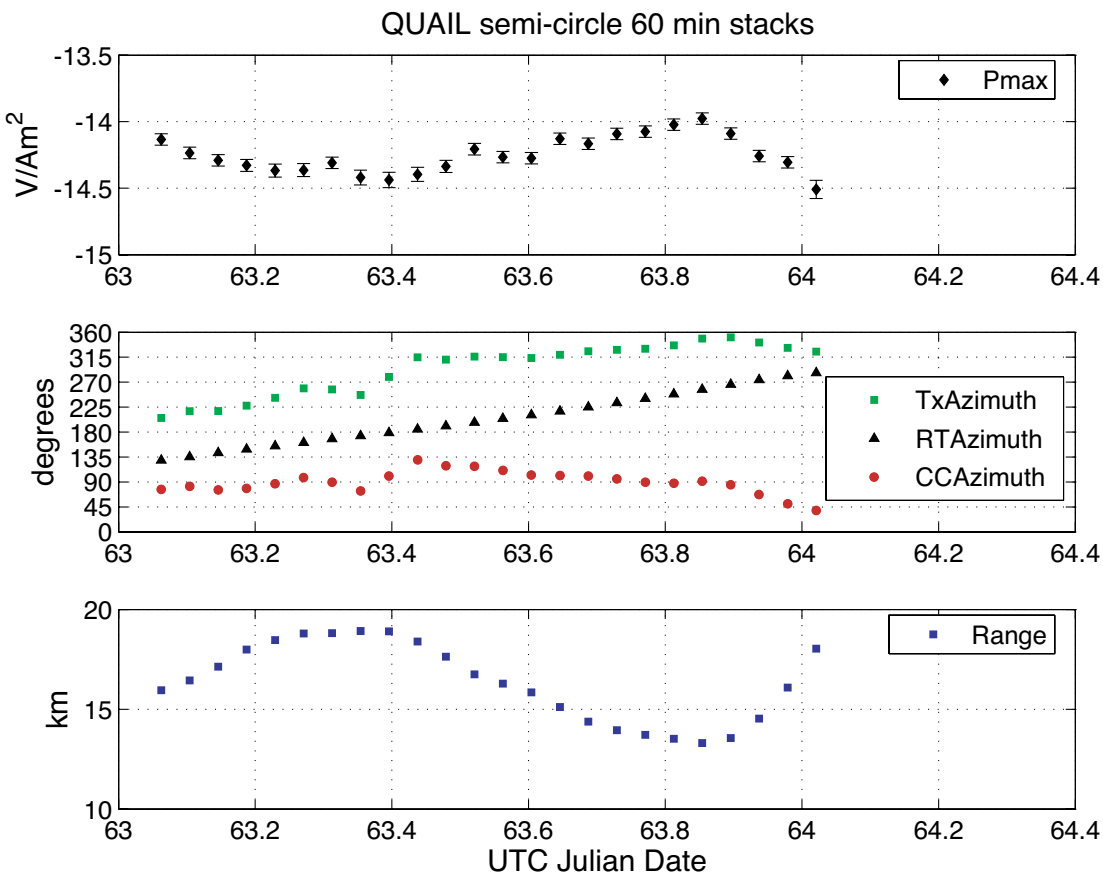

Figure 3.32 P_{MAX} data and navigational parameters from the semicircular tow around ELF QUAIL. 60-minute stack frames were used Note the significant variation in range and CCAzimuth (and the correlated variations in P_{MAX}).

3.7 References

Constable, S., and C. S. Cox (1996), Marine controlled-source electromagnetic sounding 2. The PEGASUS experiment, Journal of Geophysical Research, 101, 5519-5530.

Constable, S. C., A. S. Orange, G. M. Hoversten, and H. F. Morrison (1998), Marine magnetotellurics for petroleum exploration; Part I, A seafloor equipment system, Geophysics, 63, 816-825.

Evans, R. L. (1991), Electrical Resistivity Structure of the East Pacific Rise Near 13° N, Ph.D. thesis, 229 pp, University of Cambridge.

Everett, M. E., and S. Constable (1999), Electric dipole fields over an anisotropic seafloor: theory and application to the structure of 40 Ma Pacific Ocean lithosphere, Geophysical Journal International, 136, 41-56.

Flosadóttir, Á. H., and S. Constable (1996), Marine controlled-source electromagnetic sounding 1. Modeling and experimental design, Journal of Geophysical Research, 101, 5507-5517.

Key, K. W. (2003), Application of Broadband Marine Magnetotelluric Exploration to a 3D Salt Structure and a Fast-Spreading Ridge, 109 pp, University of California, San Diego.

MacGregor, L. M. (1997), Electromagnetic investigation of the Reykjanes Ridge near 58° North, Ph.D. thesis, 264 pp, University of Cambridge.

Webb, S. C., S. C. Constable, C. S. Cox, and T. K. Deaton (1985), A Seafloor Electric Field Instrument, Journal of Geomagnetism and Geoelectricity, 37, 1115-1129.

Chapter 4

Modeling and Inversion

4.1 Introduction

It is apparent from the data collected by the LEMs during the large circular tow (Figure 4.1) that the bulk electrical conductivity of the lithosphere is anisotropic. An increase in P_{MAX} (by a factor of 2) when the transmitter was to the north and south indicates that the more conductive horizontal direction is oriented north/south. This assertion is supported by comparison with both conductive vertical sheets models (Figures 2.13, 2.14) and horizontal conductive rods models [Everett and Constable, 1999]. While it may seem paradoxical that fields diffusing in the conductive direction would be more intense at a given range, the geometry is azimuthal-mode, **E** oscillates parallel to the transmitter, and $|E|$ is thus a function

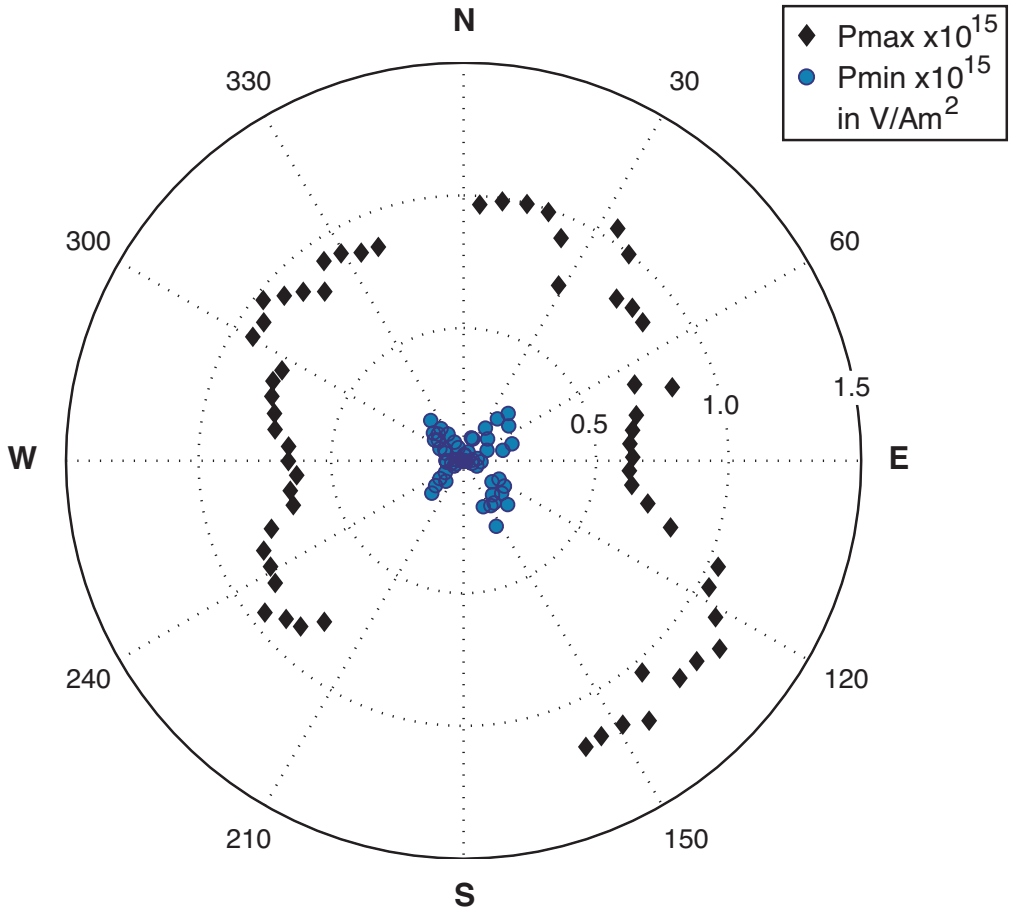

Figure 4.1 P_{MAX} and P_{MIN} data, recorded by the OBEM Mk II LEMs at the center of the large circular tow. This is a polar plot version of Figure 3.29. Symmetric patterns indicate an electrical conductivity anisotropy aligned with the fossil spreading direction

of the more resistive east/west component of σ when the transmitter is to the north or south.

Another indication of anisotropy is the 4-lobed pattern in P_{MIN} vs. RTazimuth (Figure 2.14). Over an isotropic lithosphere, $P_{MIN} = 0$ in the azimuthal mode (Figures 2.10, 2.11).

Anisotropy is present in the lithosphere, but at what depth? Is the crust anisotropic? Is the upper mantle? Individual subsets of the data were inverted to determine resistivity structure at different depths in the lithosphere. Short source-receiver offset data provide constraints on the resistivity structure of the crust, while longer offset data penetrate into the upper mantle. The maximum depth of sensitivity is generally no more than half the source-receiver offset, and typically somewhat less (*e.g.*, section 4.2.2).

This chapter will focus primarily on the geophysical modeling results; geologic interpretation will follow in Chapter 5.

4.2 Short radial tows

Perimeter receivers collected short-offset data during the large circular transmitter tow; ranges were between 2 and 20 km. The source-receiver orientations were approximately radial for $r > \sim 6$ km. At shorter offsets, more azimuthal mode energy was involved.

These data subsets are characterized in one of three different ways (Table 4.1), depending on context: (1) as a two-letter designation indicating the receiver name and the relative location of the transmitter (either North or South); (2) as the azimuth from the center of the large circle to the approximate center of the tow line; or (3) in terms of the geodetic orientation of the tow line.

The working hypothesis for this section is that the crust is the source of the anisotropy observed in the 30 km radius circular tow data (Figure 4.1). If that were true, isotropic inversion of short radial tow data would indicate greater conductivities from the north-south trending tows than from those trending east-west.

Receiver	Transmitter tow line	Azimuth to Tx line from center of large circle	Geodetic orientation of Tx line
PLATY	PS	-168.75	90
	PN	-146.25	-45
RHONDA	RS	-123.75	-45
	RN	-101.25	0
BANDI	BS	-078.75	0
	BN	-056.25	45
QUAIL	QS	-033.75	45
	QN	-011.25	90
GALAH	GN	011.25	90
	GS	033.75	-45
TREVOR	TN	056.25	-45
	TS	078.75	0
CROC	CN	101.25	0
	CS	123.75	45
NODDY	NN	146.25	45
	NS	168.75	90

Table 4.1 Perimeter receiver data collected during the large circular tow are each divided into two subsets; one when the transmitter is north of the receiver (XN) and one when it is south (XS). These segments can be represented either in terms of their geodetic azimuth along the circle (appropriate for determining heterogeneity), or in terms of the principal geodetic orientation of the transmitter-receiver pair (appropriate for determining bulk crustal anisotropy). Segments shaded in grey were not actually towed, these subsets therefore do not exist.

4.2.1 Two-layer models

Marquardt inversions (section 2.5.1) of the short radial tow P_{MAX} data were carried out with three variable parameters **p**: upper subsurface layer resistivity and thickness, and lower halfspace resistivity. Five different starting models were used (Table 4.2), all with 4400 m

Starting Model	ρ_1 (Ωm)	ρ_2 (Ωm)	h_2 (m)
a	1	1000	500
b	3	3000	500
c	10	10^4	500
d	1	1000	100
e	3	3000	100

Table 4.2 Starting models for two-layer 1-D isotropic Marquart inversion of short radial tow data.

water depth and 90 m Tx altitude. This model parameterization was motivated by the assumption that the crust can be approximated electrically as a conductive layer of sediment and fractured basalts over a more resistive basement with lower fluid permeability. Inversions for smooth models (section 4.2.2) support this assumption.

These inversions were run with an earlier version of these data sets; the 4 Hz data were the same as in the final sets presented in Figure 3.30, but with a few 12 and 20 Hz data (with large error bars) added from the OBEM Mk II instruments. These higher harmonic data were not used for any other model studies presented in this dissertation.

Results are plotted in Figure 4.2. Misfits ranged from RMS 0.41 to 1.17. Of the five starting models for each data set, redundant results and models with grossly implausible parameter values were discarded. The inversion routine sometimes had trouble converging on a solution from one or more of the starting models, especially with the data sets BN, TN, CN, and NN; none of the starting models converged on a solution for BS.

These results do not suggest significant crustal anisotropy.

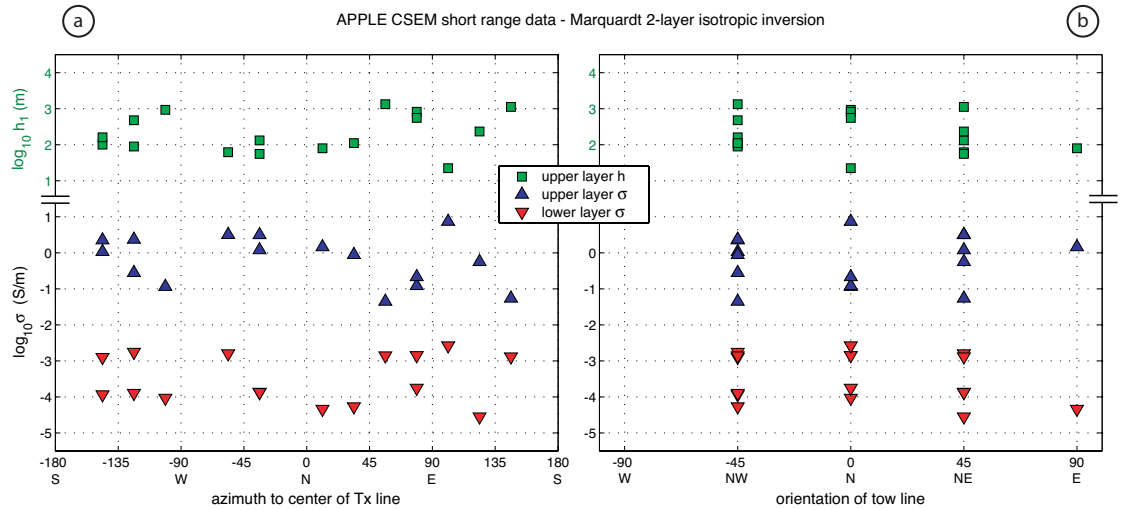

Figure 4.2 Two-layer crustal models from isotropic Marquardt inversion of short range tows (a) plotted vs. azimuth from the center of the large circle to the approximate midpoint of the tow line and (b) plotted vs. the orientation of the tow. No consistent indicator of anisotropy is apparent.

4.2.2 Smooth models

OCCAM inversions (section 2.5.2) of the short radial tow P_{MAX} data were computed to generate smooth isotropic models of subsurface resistivity. Misfit tolerances were:

$$\begin{bmatrix} 1.05 & 1.10 & 1.25 & 1.5 & 2.0 \end{bmatrix} \times \mathrm{RMS}_{MIN}$$

where the minimum misfit RMS_{MIN} for each data set was found by setting the target resistivity to RMS 0.1, letting the code run for 40 iterations, and observing the misfit achieved by that point (). If the inversion could not converge on a solution at the lower misfits, as was sometimes the case, RMS_{MIN} was simply re-set such that 1.05 x RMS_{MIN} was the lowest previously convergent misfit tolerance, and a new set of inversions was run.

FILE	min misfit	1.05x		1.1x		1.25x		1.5x		2x	
PN	0.482	0.506	70	0.530	12	0.603	12	0.723	12	0.964	10,**26**
RS	0.323	0.339	13	0.355	12	0.404	14	0.485	12	0.646	12,**18**
RN	0.8305	0.872	16	0.914	13	1.038	13,**28**	1.246	14	1.661	15
BS	0.258	0.271	15	0.284	15	0.323	12	0.387	12	0.516	12,**14**
BN	0.611	0.642	19	0.672	13	0.764	9,**8**	0.917	8	1.222	8
QS	0.506	0.531	16	0.557	12	0.633	11	0.759	11,**11**	1.012	10
GN	0.39	0.410	19	0.429	17	0.488	15,**11**	0.585	13	0.780	11
GS	0.504	0.529	13	0.554	13	0.630	12,**10**	0.756	10	1.008	8
TN	0.451	0.474	16	0.496	16	0.564	15,**17**	0.677	14	0.902	10
TS	0.359	0.377	13	0.395	13	0.449	13	0.539	14,**29**	0.718	13
CN	0.478	0.502	99	0.526	10	0.598	10,**11**	0.717	9	0.956	8
CS	0.692	0.727	11	0.761	10	0.865	9,**11**	1.038	9	1.384	9
NN	0.614	0.645	9	0.675	10	0.768	9,**24**	0.921	9	1.228	8
LQ3	0.993	1.043	40	1.092	20	1.241	15	1.490	**13**	1.986	10,**8**
LQE6	0.918	0.964	48	1.010	50	1.148	**9**	1.377	*	1.836	*
LQN6	0.915	0.961	50	1.007	21	1.144	**5**	1.373	*	1.830	*
QSE	0.527	0.553	23	0.580	40	0.659	31	0.791	**8**	1.054	7
QSN	0.337	0.354	<u>40</u>	0.371	18	0.421	6	0.506	**4**	0.674	*

Table 4.3 Occam inversion of each data subset minimizing R_1 was run for a suite of misfit tolerances based on the minimum convergent misfit. For each subset at each relative tolerance, the actual RMS misfit is shown in the first column, and the number of iterations required for convergence in the second. Where two iteration numbers are shown, the second indicates minimization of R_2 (second-derivative rougness). Boldface indicates models used for interpretation. Underline indicates non-convergence. A star (*) indicates, for prejudiced inversion, an RMS greater than the initial misfit.

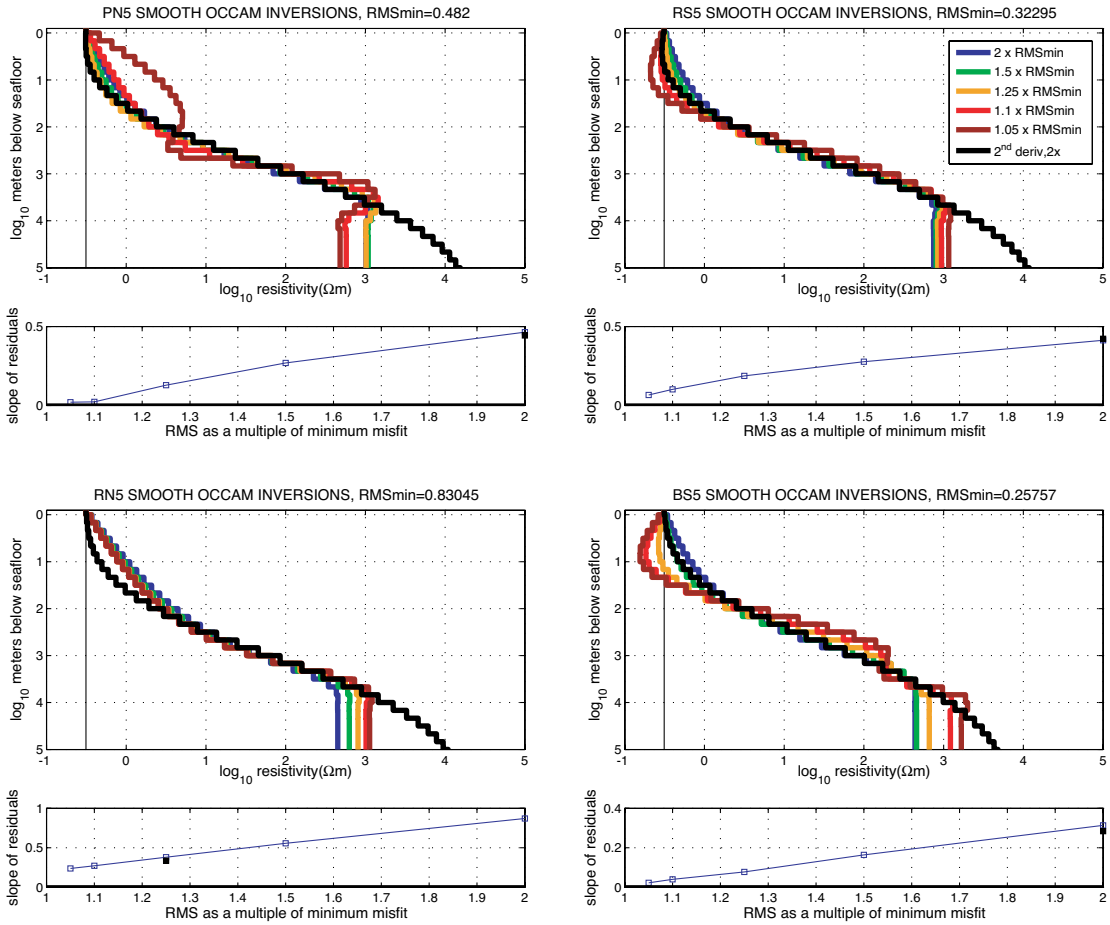

Figure 4.3 Minimum roughness models from Occam inversion of short-range P_{MAX} data collected by the perimeter receivers. Side-by-side plots are from the same tow segment, measured by the instruments at each end. Seawater ρ is indicated by the vertical line; models were constrained to approach this value at the seafloor. Note maximum sensitivity to resistivity structure occurs in the interval 100 m to 4 km below the seafloor. Misfit slope is also presented; the black square corresponds to the 2nd derivative smoothing model.

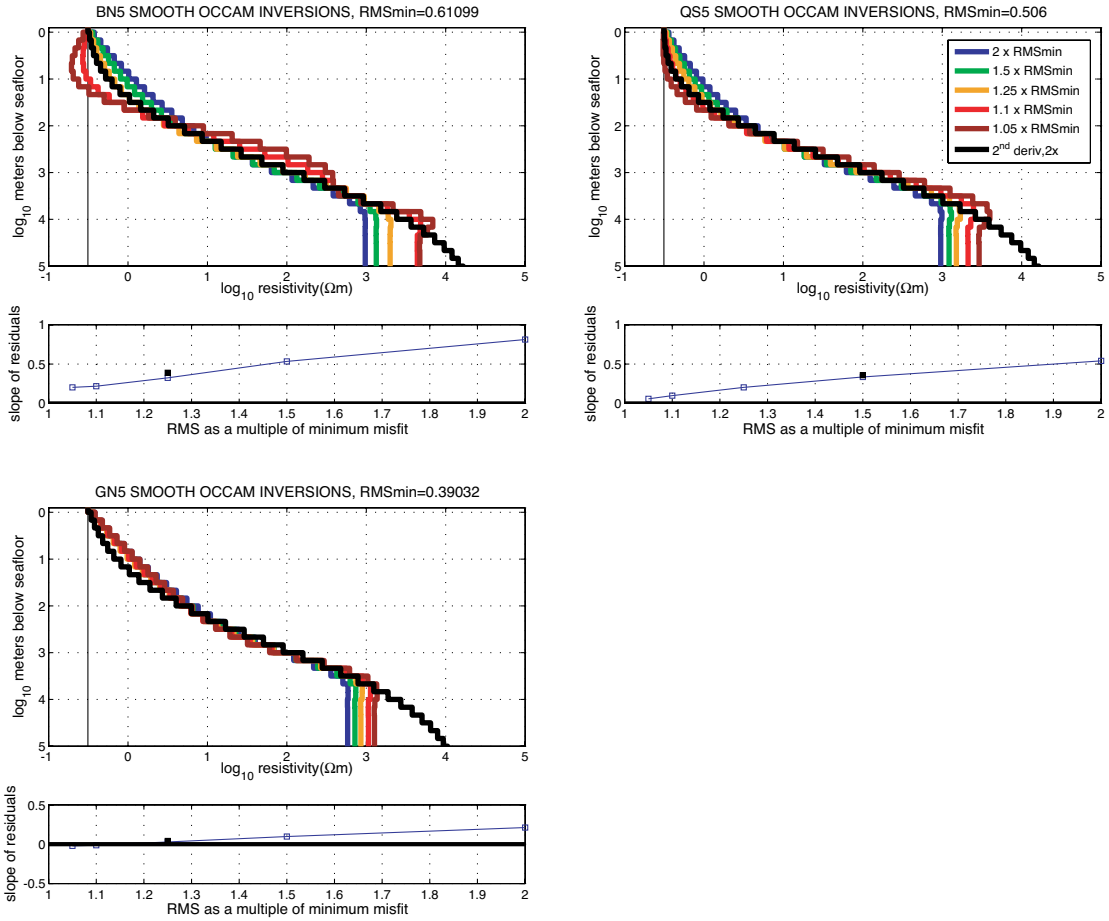

Figure 4.3 (cont.)

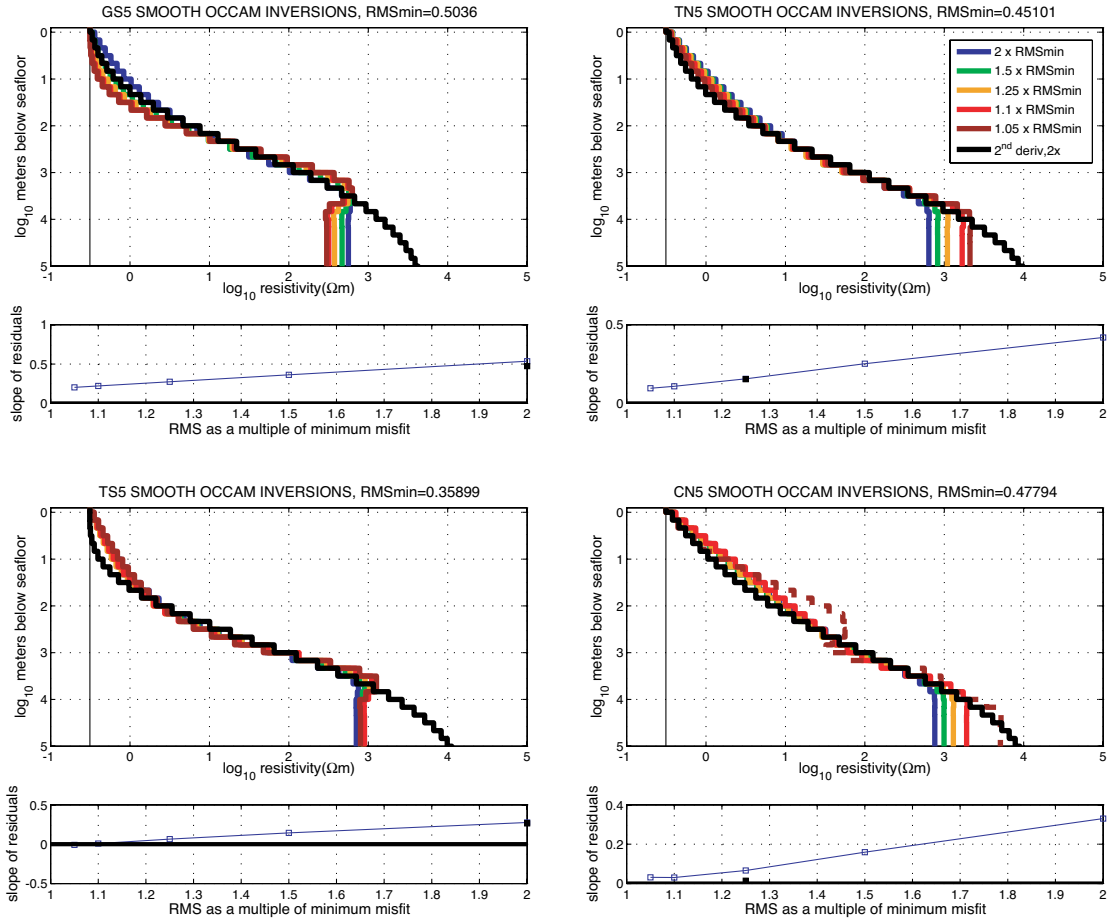

Figure 4.3 (cont.)

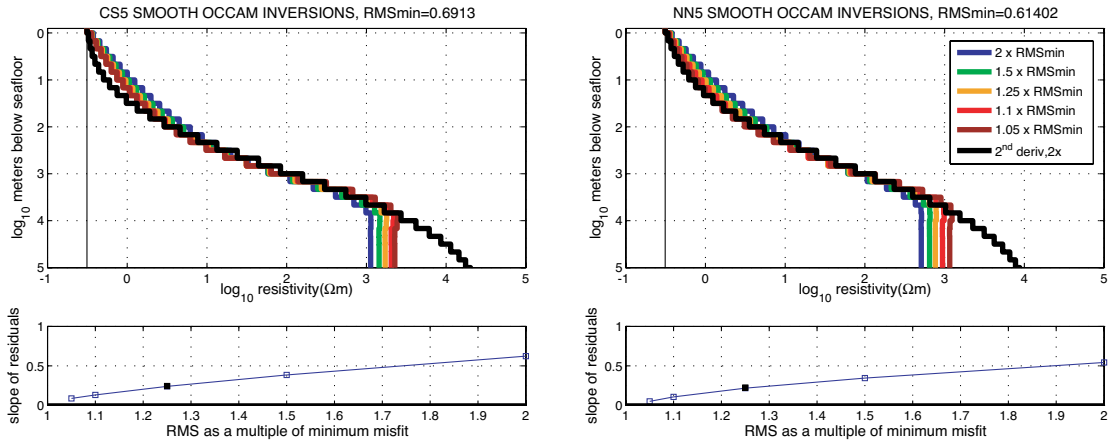

Figure 4.3 (cont.)

For each tow segment / receiver pair, models smooth in the first derivative (minimum R_1) are found at each misfit (Figure 4.3). Second derivative smoothing models required a bit more misfit tolerance to converge. The top subsurface layer was set to be seawater conductivity in all cases; this kept the top 100 m from becoming unrealistically conductive due to over-fitting: the lack of offsets less than ~2 km and large non-gaussian data uncertainty at the shortest ranges (section 3.5.1) prohibited independent sensitivity to the conductivity of the top ~100 m. These large short-offset uncertainties were also the reason behind some of the unusually small RMS values obtained.

The best-fit linear slope of the residuals (vs. log source-receiver offset) is presented for each misfit. A slope of zero means that all the data are being fit equally well. A positive slope means that the model predicts weaker fields at long range, and stronger fields at short range, than in the real data. A slope of zero would nominally be desirable if the uncertainty was of the same nature for all ranges, but that is not the case; and so the predominantly positive residual slopes are accepted as necessary.

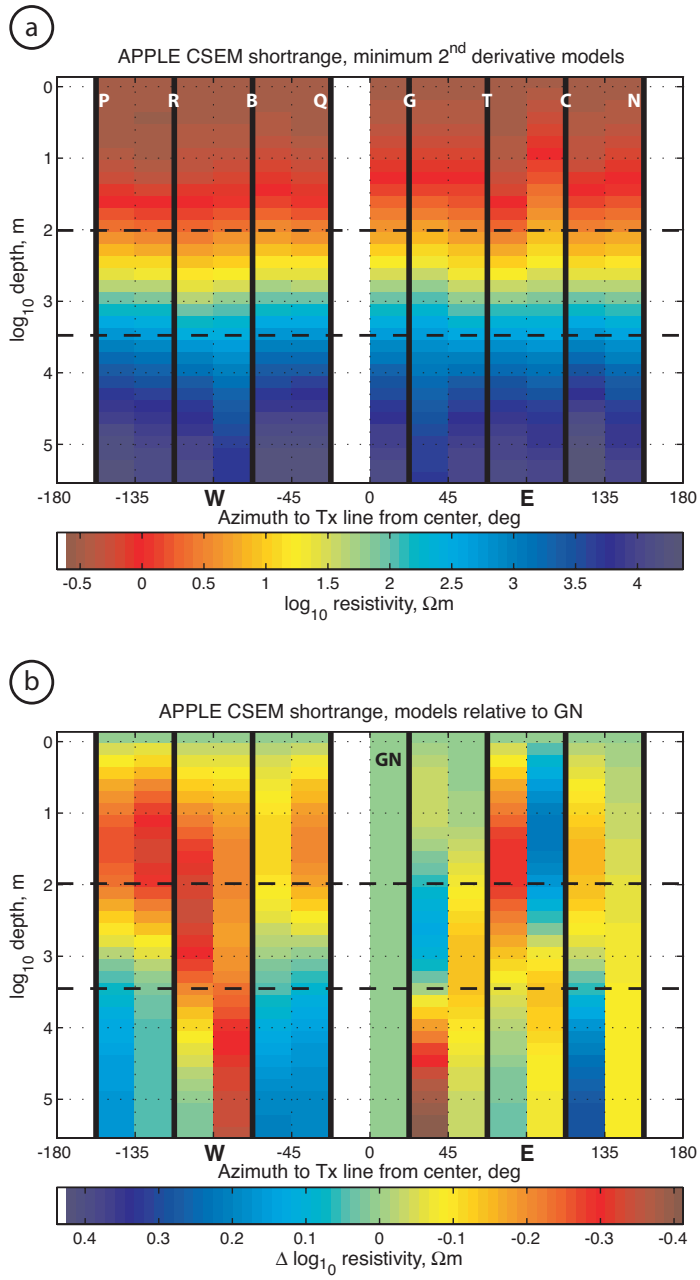

Figure 4.4 (a) A compilation of the preferred (minimum R_2) models, shown in Figure 4.3, from each of the short-range data subsets. Receivers are located at the vertical black lines. Horizontal dashed lines frame the interval of maximum sensitivity. (b) To highlight the variations between models, they are differenced against the lone E-W trending transmitter tow. Warm colors indicate greater conductivity. No indication of anisotropy greater than the local heterogeneities is observed.

It is observed that these models are most tightly constrained between 100 m and ~ 4 km depth. Outside of this depth window, changes in conductivity have little effect on the data fit. This is especially evident when comparing the second derivative model to the first derivative models for a given data set: a large increase in resistivity at depth can be compensated for by a slight increase in conductivity in the top 100 m.

Taking the second derivative smoothing models to be representative of each data subset, they are compared side-by-side (Figure 4.4.a). It is evident that the crustal conductivity around the array is grossly consistent. Comparing the values directly to the lone E-W trending tow path GN (Figure 4.4.b) and focusing on the high sensitivity zone between 100 m and 4 km depth is instructive:

On the west side, the north-south trending tows indicate an increase in σ of up to 0.4 orders of magnitude (equivalent to a linear ratio of 2.5). This would be consistent with paleo-ridge parallel vertical sheets of increased conductivity in the sheeted dyke layer – but there is a problem with this analysis.

On the east side, no anisotropic pattern is apparent whatsoever, and the magnitude of the heterogeneity is as great as the (possibly) anisotropic pattern observed on the west side.

These results do not suggest the presence of significant crustal anisotropy relative to the magnitude of decidedly non-anisotropic heterogeneity observed across the survey site.

4.3 LQ3 composite data set

The long radial tow, as measured by the LEMs, contains source-receiver offsets ranging from 14 km to 70 km. These data provide sensitivity to the lower crust and upper mantle, are predominantly radial-mode geometry, with the transmitter oriented at ~45° to the anisotropic strike.

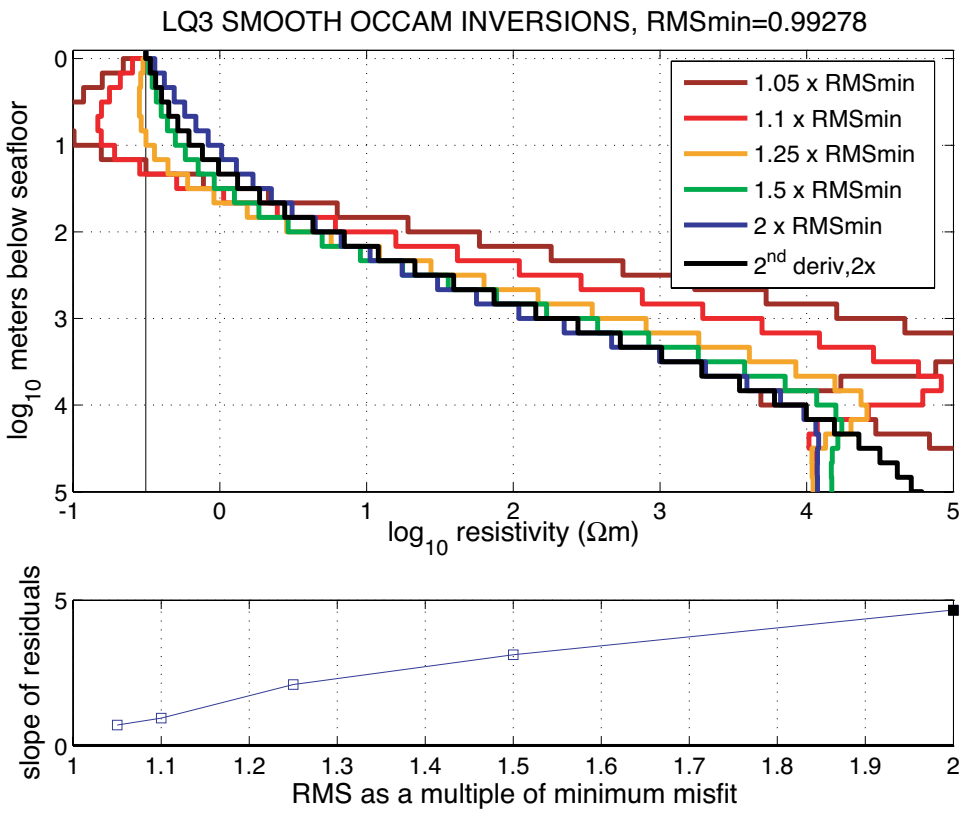

Figure 4.5 Smooth P_{MAX} inversions of composite data set LQ3 for 1-D, isotropic resistivity. The 1.5 x RMS_{MIN} model was chosen as the preferred model for further analysis and interpretation. Larger RMS for LQ3 inversion than for the short-range data inversions (Figure 4.3) may indicate deep anisotropy.

In order to create a data subset that contained the richest mix of source-receiver offsets and geometries while restricting aerial extent to avoid what little heterogeneity may be present, the long radial tow data were combined with: the mostly radial-mode short-offset QS; azimuthal data from the semicircle tow as measured by QUAIL (which lie between 13 and 19 km in offset); and a few azimuthal-mode data measured by the LEMs when the transmitter was tracing the QS path of the 30 km radius circular tow. This subset was dubbed LQ3, "Long-range and Quail", 3rd revision.

4.3.1 P_{MAX} inversion

LQ3 was inverted for smooth models (Figure 4.5) using the method described for short radial tows (section 4.2.2). At lower misfits, the top 20 m are more conductive than seawater, and these models are thus deemed unsuitable for interpretation. The 1.5 x RMS_{MIN} (1.490 RMS) minimum R_1 model is chosen to be the preferred model for further study. Observation of the deep divergence of the minimum R_1 and R_2 models at 2 x RMS_{MIN} indicates a maximum depth of sensitivity of around 20-30 km, well into the upper mantle. The "flattening" of the minimum R_1 models at around 30 km corroborates; when the layer resistivity no longer affects the misfit, $\partial\rho/\partial z \rightarrow 0$.

The misfit slope is again positive. Plotting the misfit vs. source position on a receiver-centered grid (Figure 4.7) aids in visualizing the geometries present. Significantly, the residuals of the semicircular data, which would be sensitive to the upper crustal anisotropy, do not strongly suggest an anisotropic pattern oriented N/S-E/W.

4.3.2 Single-component inversion

In order to exploit the result, shown in section 2.4.2, that the horizontal component of the seafloor **E** parallel to the anisotropic strike is the same as in the isotropic case, the N/S and E/W components of **E** were inverted separately for minimum R_1, prejudiced against deviations from the preferred model described above.

The models at 1.25 x RMS_{MIN} were chosen for interpretation (Figure 4.6); smaller misfits led to spurious oscillations. When LQ3 was decomposed into component amplitudes, several data fell below the noise floor and were removed prior to inversion (Figure 4.7). In addition, data were removed for stack frames where the polarization ellipse orientation

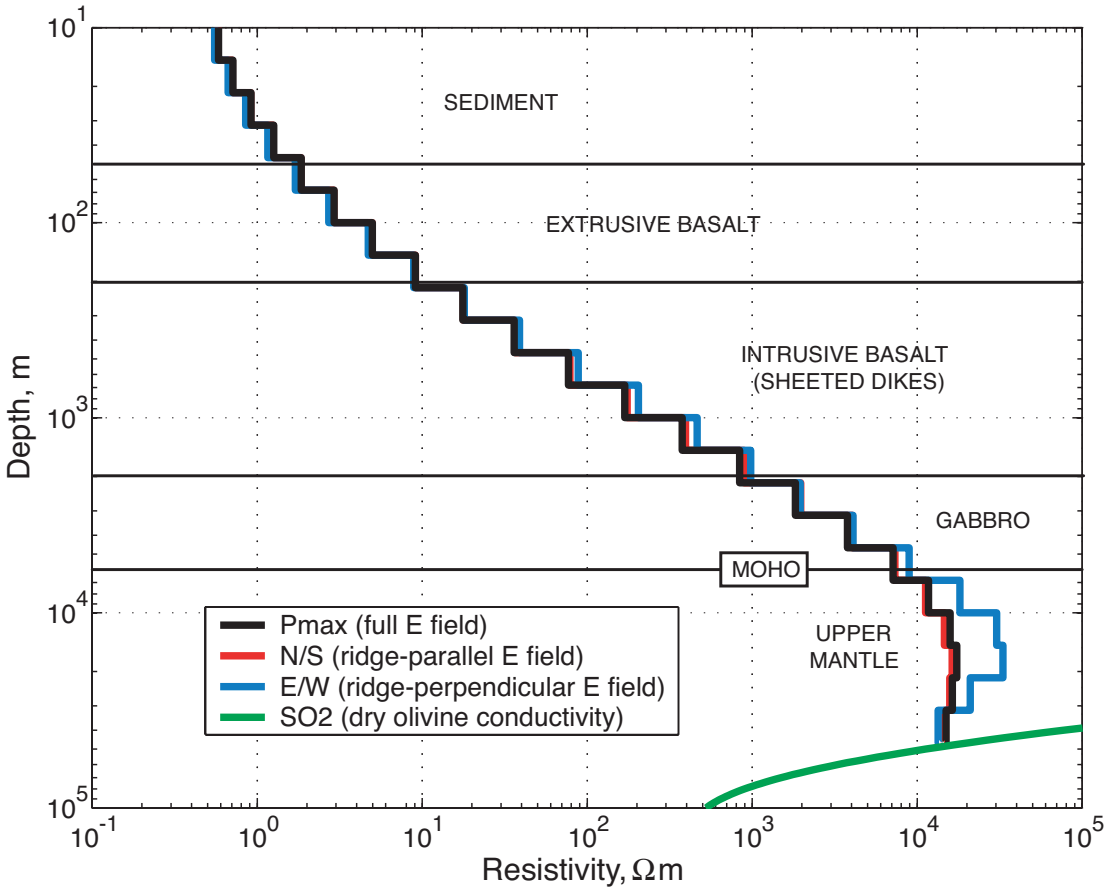

Figure 4.6 Preferred models from inversion of LQ3 and associated single-component data inversions. Typical layer boundaries are indicated for mature Pacific lithosphere, and the dry olivine conductivity was found by combining SO2 (section 1.3.2) with a parameterized halfspace cooling model (section 1.3.1).

straddled the line normal to a particular channel's orientation; phase of the best-fit sinusoid jumps 180° when this "line of polarity" is crossed, leading to phase cancellation within the stack frame.

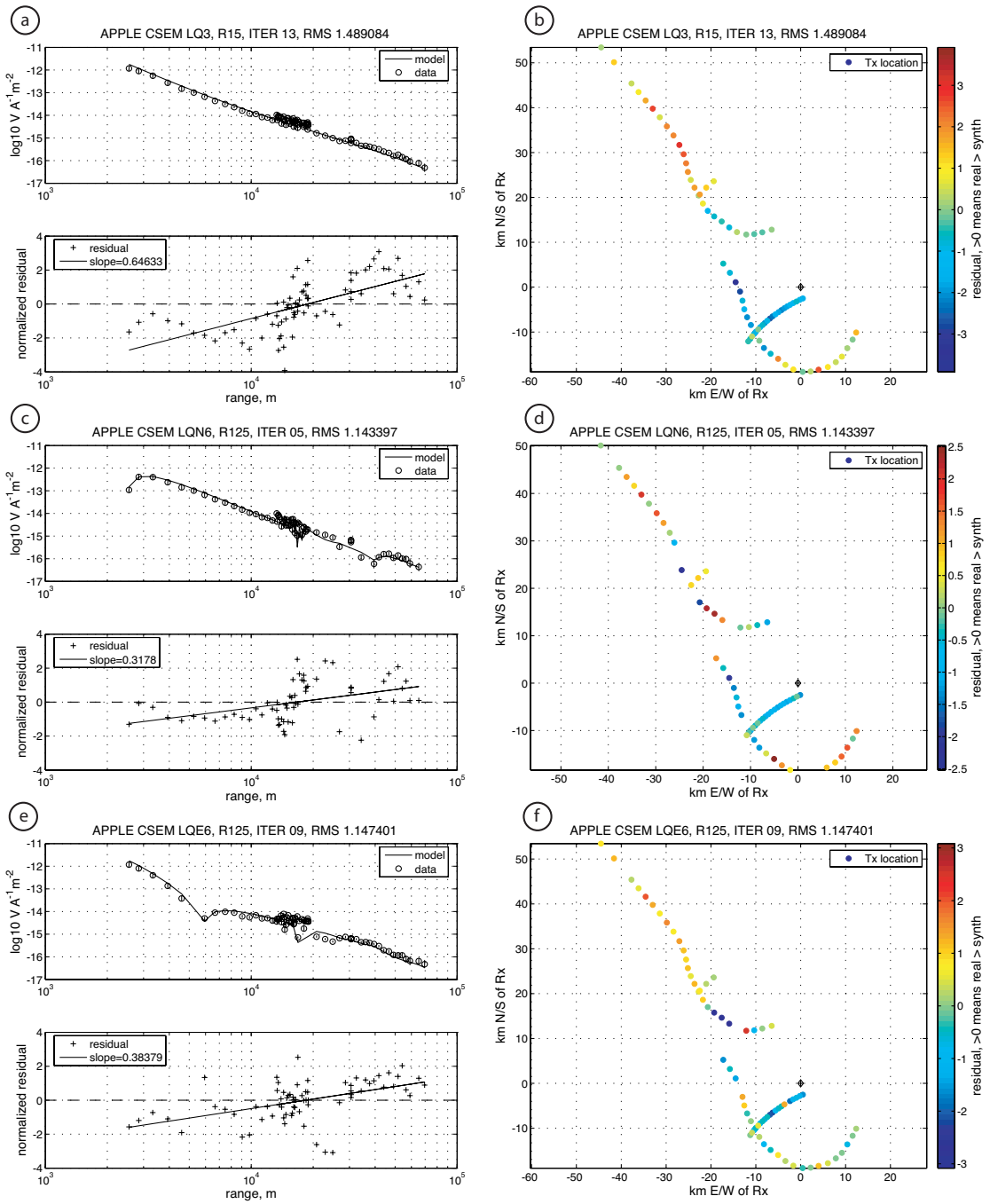

Figure 4.7 Real data, preferred inversion model data, and residuals normalized by uncertainty for (a,b) P_{MAX} data subset LQ3 and associated single-component (c,d) $|E_{N/S}|$ data LQN6 and (e,f) $|E_{E/W}|$ data LQE6.

The N/S data do not require deviation from the P_{MAX} inversion result, suggesting that the anisotropic strike is aligned N/S – that is, $\sigma_{N/S} = \sigma_z = \sigma_{||}$. The E/W data require a slight increase in resistivity (a factor of 1.25) around 1 km depth (in the sheeted dikes), and a more robust increase in resistivity (a factor of 2) from 6-7 km down to 20-30 km (the upper mantle), where the data lose sensitivity. Inspection of Figure 2.13 indicates that, in the case of N/S oriented vertical sheets of increased conductivity, the E/W component will be stronger than in the isotropic case for radial mode geometries when the transmitter is at 45° to the anisotropic strike, leading to the greater model resistivities observed upon E/W component isotropic inversion.

As shown in section 3.3, the orientation of the LEMs is known to $\pm 1°$, while QUAIL is known to $\pm 5°$ at best, adding some systematic uncertainty to the short-range data and, therefore, the resistivity structure between 100 m and 4 km. The hint of crustal anisotropy, therefore, is a bit spurious, while the deep anisotropy is more certain.

Prejudiced single-component inversions of several of the short-range data subsets were carried out; the results as a whole are not consistent with each other, and point towards the conclusions already drawn from section 4.2. The result from QS is shown (Figure 4.8) to examine the contribution these data make to the LQ3 inversion models. The strike of any crustal anisotropy is again N/S, with a split in resistivity indicated below 2 km depth, which would be in the gabbros. This gabbroic split does not appear in the full LQ3 analysis; it is thus likely that it is offset by the semicircular tow data, which lie at the same source-receiver offsets as the more distant part of QS.

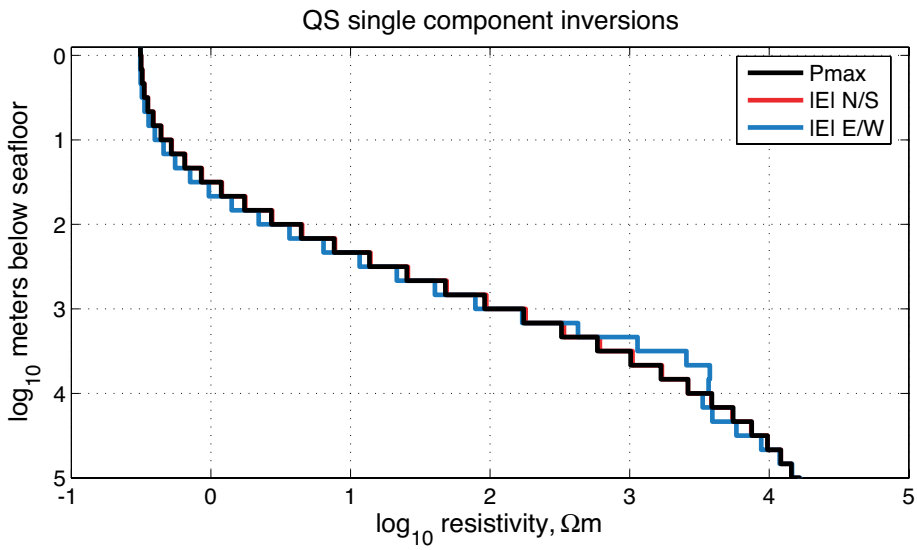

Figure 4.8 Single component inversions of QS, prejudiced against the preferred P_{MAX} inversion model.

4.3.3 Ellipse parameters

The preferred model from LQ3 was constrained by P_{MAX}, but other ellipse parameters are available for interpretation. P_{MIN} and α_N were computed for the subsets used to generate LQ3 and for the large circular tow, as measured at the LEMs (Figure 4.9).

Looking at the large circle data (Figure 4.9.a) (only three of which were used in the inversion), the anisotropic pattern in P_{MAX} is evident, along with the presence of P_{MIN}, which would be zero over an isotropic seafloor. α_N is mostly Tx-parallel.

P_{MAX} and α_N are well fit by the isotropic model for QS (Figure 4.9.b). The anomalous increase in P_{MIN} for ranges > 10 km may indicate the presence of crustal anisotropy; it has already been observed that single-component inversion of these data required a small split in crustal conductivity.

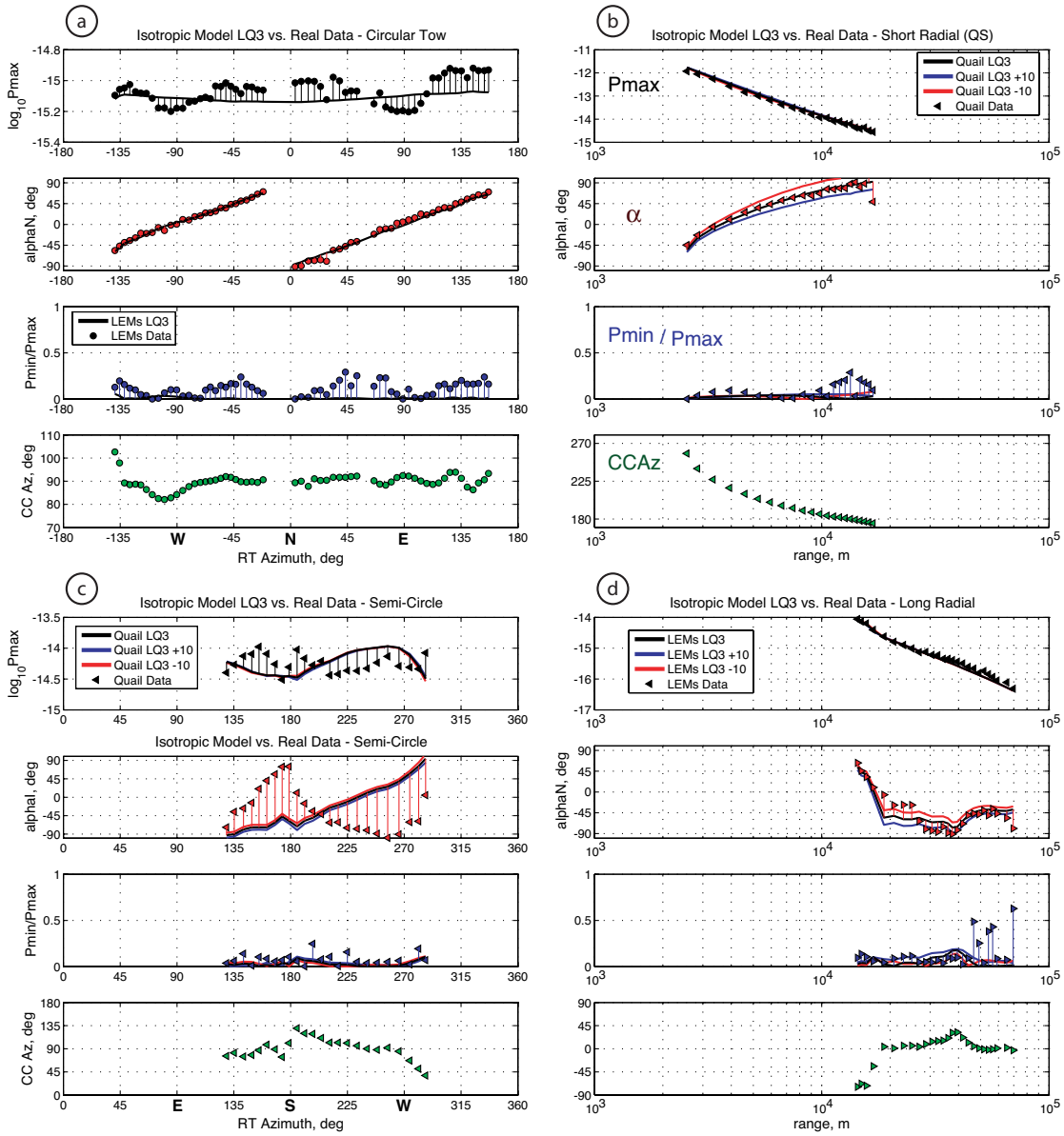

Figure 4.9 P_{MAX} was used to constrain the LQ3 inversion; forward modeling indicates how well it predicts P_{MIN} and α_N. Discrepancies may indicate the presence of anisotropic (or higher-dimensional) conductivity. Tx was rotated $\pm 10°$ to test for effects of navigational uncertainty. α_I (orientation relative to instrument ch 1) is shown for QUAIL for plotting convenience; QUAIL ch 1 was oriented at 140° geodetic (section 3.3.1.2).

A similar result is seen in the long radial tow (Figure 4.9.d). α_N data indicate some anomalous twist, but it was during an unsteady portion of the tow, as the ship was turning during stormy weather. It is observed that a +/- 10° wag of the transmitter can nearly accommodate this twist. P_{MIN} being smaller in magnitude than P_{MAX}, it is possible that the anomalous ellipse eccentricity at the longest ranges was caused by proximity to the noise floor.

P_{MAX} data measured by QUAIL during the semicircular tow (Figure 4.9.c) show a half-order of magnitude variation from the isotropic prediction, as well as an enormous amount of twist, but no anomalous P_{MIN}. These results may indicate some crustal anisotropy, as the offsets involved are far more sensitive to the crust than to the mantle. The unsteady nature of the semicircular tow geometry (up to 45° away from azimuthal mode, with long-period altitude oscillation), however, renders these data unreliable for detailed quantitative analysis.

4.4 Large circular tow

As mentioned in section 4.1, the large circular tow data unambiguously indicate lithospheric anisotropy. Analysis of the other data subsets has placed this anisotropic material at subsurface depths in excess of 6 km, that is, below the crust and in the upper mantle, with a lesser possibility of crustal anisotropy. Modeling and inversion of the large circular tow combined-LEM data subset follows, exploring the effects and possibility of anisotropy at these two depths.

To reduce this data subset further, the observed double-mirror symmetry is exploited to collapse the data into one effective quadrant (Figure 4.10). Geometries where the transmitter is to the north are “folded” down to the south, and west to east. Statistical means and standard deviations were computed linearly within bins of 10° in receiver-to-transmitter azimuth. From

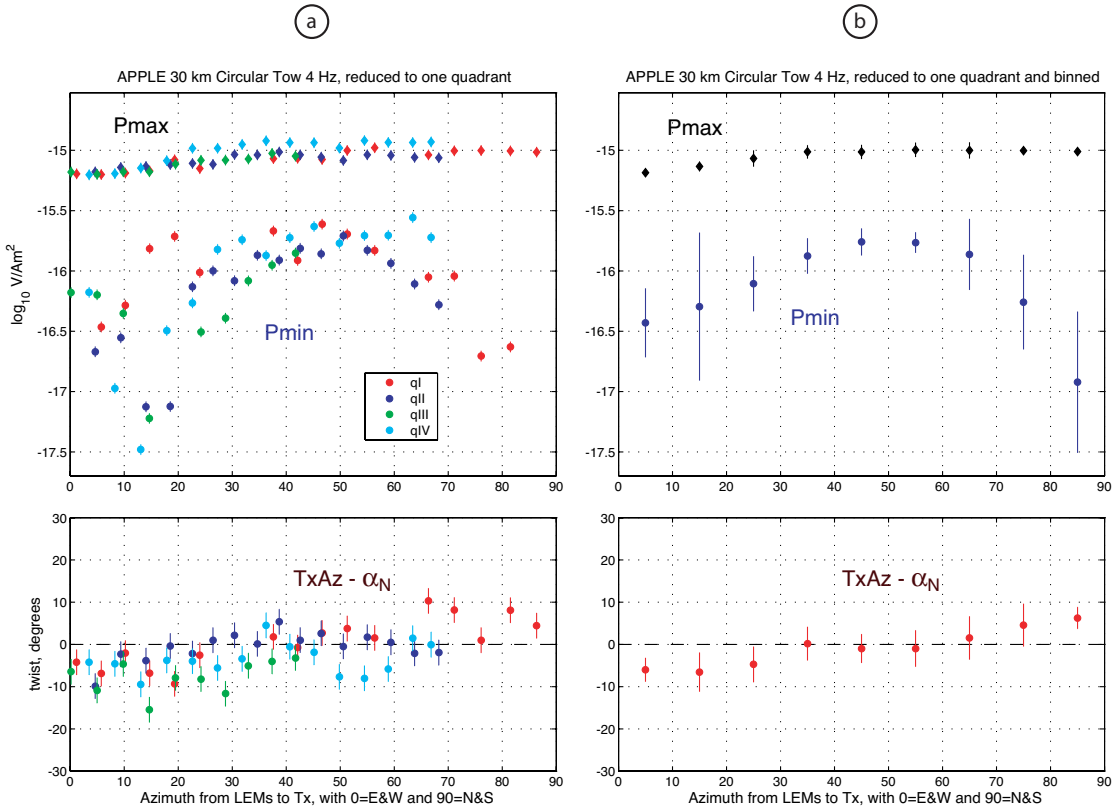

Figure 4.10 The four quadrants are collapsed into one to reduce LEM circular tow data for inversion. Statistical analysis was performed within 10° bins; adjustments made to error bars are not yet shown.

the central limit theorem, standard deviations within each bin are meaningful uncertainty estimates. While minor systematic offsets are present due to variations in range (Figure 3.29), bin standard deviations are the basis for the uncertainties used in subsequent inversion.

For P_{MAX}, bin standard deviations are used, except 10% is applied in the 75° and 85° bins due to the relative paucity of data; for P_{MIN} the maximum was set to be 25% because early inversions were being constrained too loosely (set to 0.5 orders of magnitude at 75° and 85°); twist error bars are without exception the standard deviations. The trend in twist is small, but appears to be reliably non-zero.

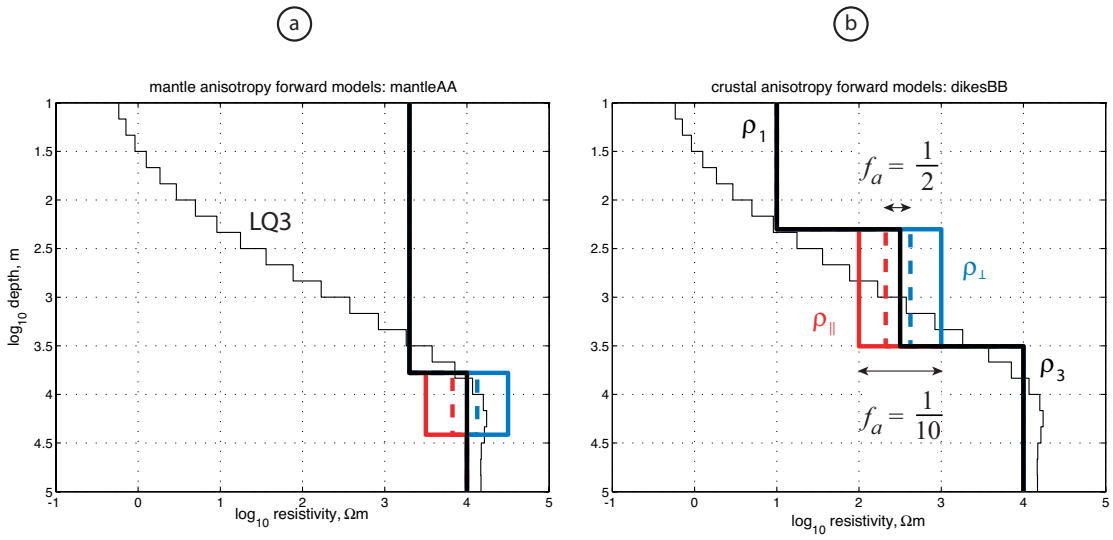

Figure 4.11 Four anisotropic models chosen to resemble the preferred LQ3 inversion result, simulating anisotropic vertical conductive sheet models with linear conductivity ratios of 2 and 10 in (a) the lithospheric upper mantle and (b) the sheeted dike portion of the crust.

4.4.1 Anisotropic forward modeling

Extensive three-layer anisotropic forward modeling (section 2.4.2) studies have been carried out by the author and Mark Everett, both separately and while working together. Several scenarios are explored by Everett, *et al.* [in preparation]. It was learned that, when analyzing the 30-km-radius circular tow data alone, the thickness of the anisotropic layer is poorly constrained, and that nonlinearity generates large changes in the predicted data for relatively minor adjustments in the model conductivities. Data predictions from four models (Figure 4.11) based on the preferred LQ3 P_{MAX} inversion model are included here.

The effect of possible crustal anisotropy on the 30 km radius large circular tow data at 4 Hz is significant (Figure 4.12). These models ("dikesBB") both have three subsurface layers, the middle one anisotropic, with resistivity and thickness parameters:

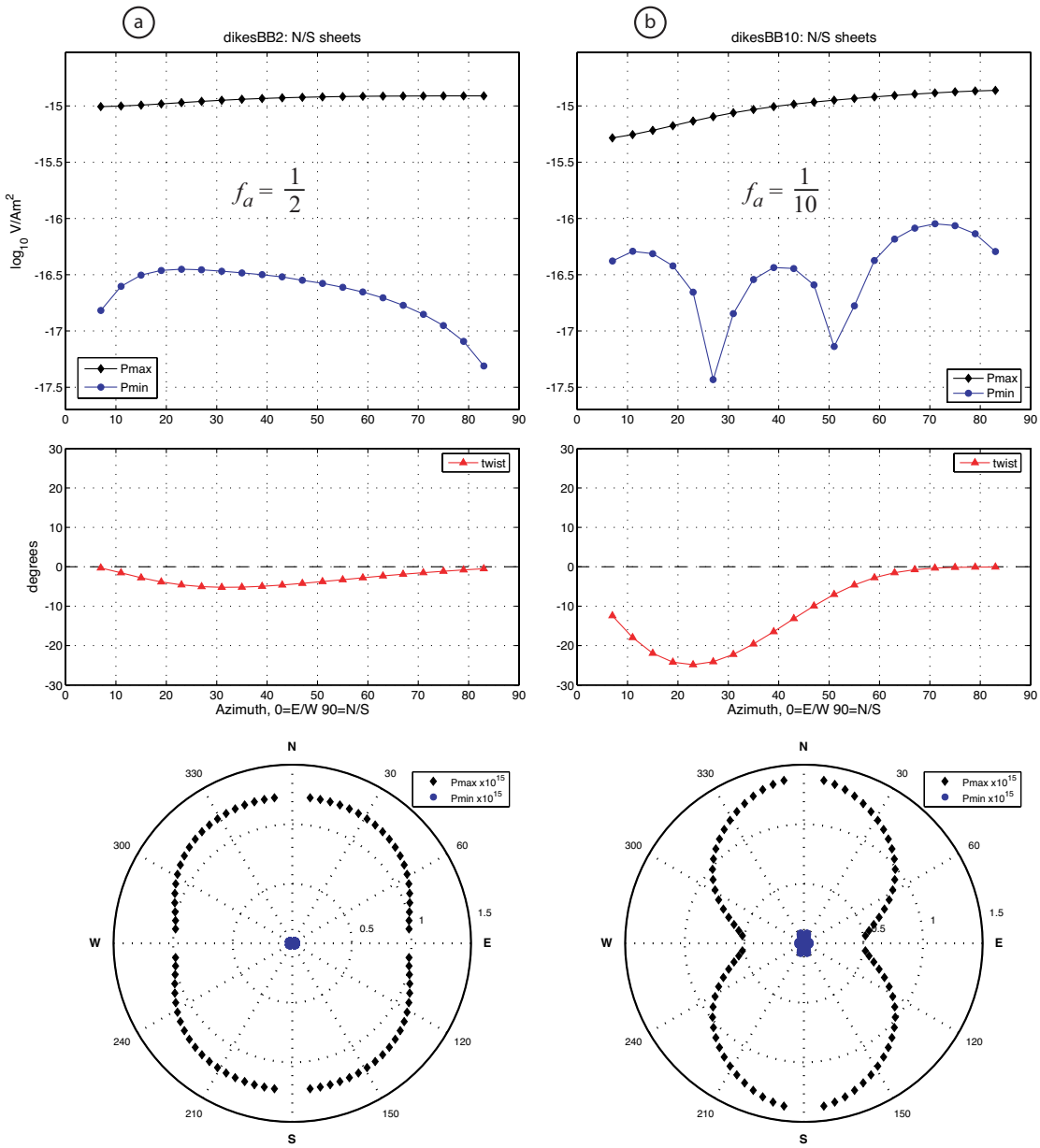

Figure 4.12 Forward computation of conductive vertical sheet anisotropy in the crust (Figure 4.11.b) generates variation in P_{MAX} at the center of the circular tow, but P_{MIN} is smaller than in the observed data.

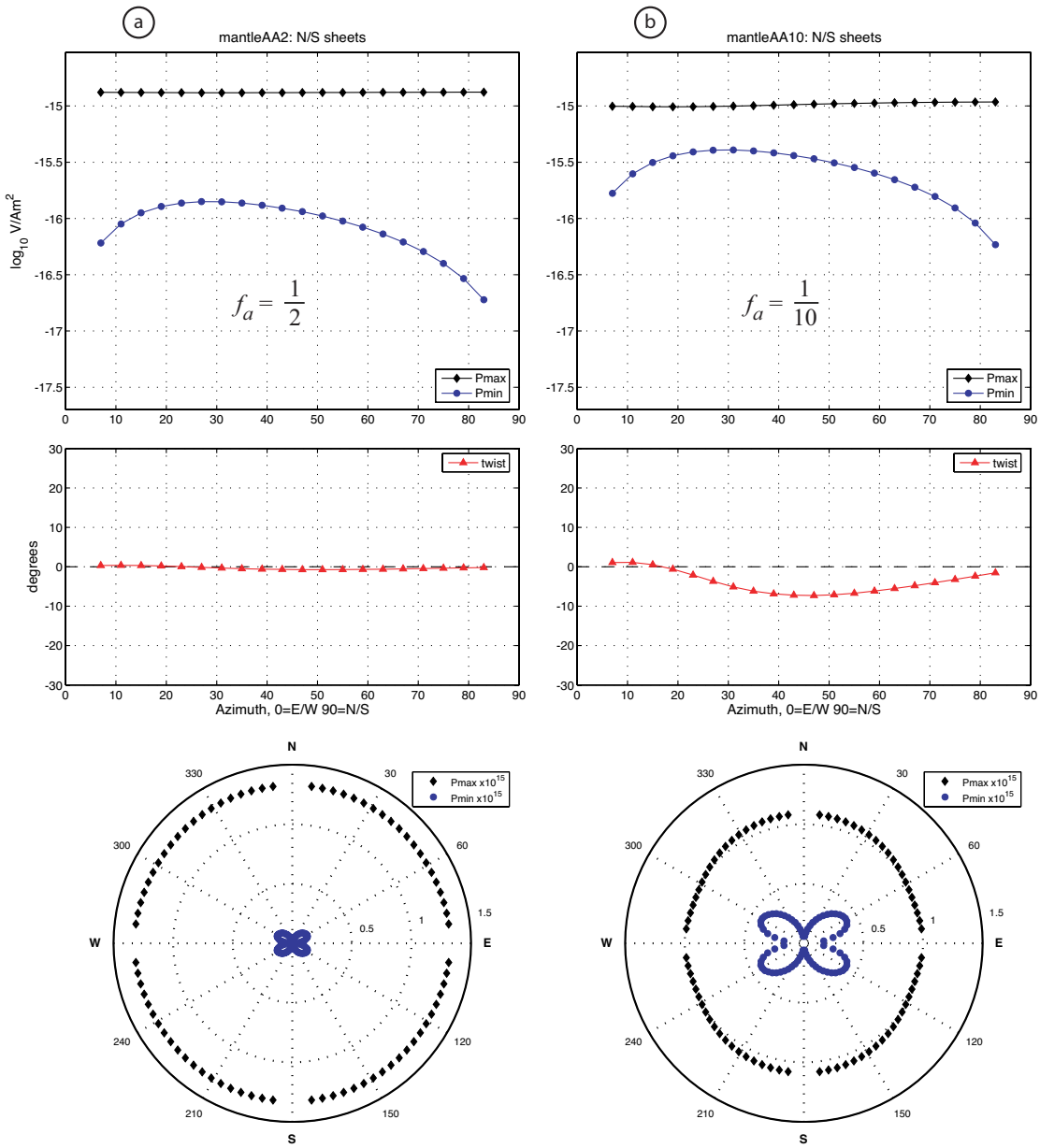

Figure 4.13 Forward computation of conductive vertical sheet anisotropy in the mantle (Figure 4.11.a) generates subtle variation in P_{MAX} at the center of the circular tow, with P_{MIN} values similar to the observed data, and less "twist" than from crustal anisotropy (Figure 4.12).

$$\text{layer 1: } \rho_1 = 10\ \Omega\text{m, dd}_1 = 200\ \text{m}$$
$$\text{layer 2: } \rho_m = 3.16 \times 10^2\ \Omega\text{m, dd}_2 = 3\ \text{km}$$
$$\text{layer 3: } \rho_3 = 10^4\ \Omega\text{m}$$

Tx height over the seafloor is 90 m. Both $f_a = 0.5$ and $f_a = 0.1$ are presented; that is, north-south trending vertical sheets more conductive by factors of 2 and 10 respectively in the approximate depth range of the sheeted dike complex. $f_a = 0.5$ generates the quantity of P_{MAX} and twist variation observed in the real data, but P_{MIN} is too small. $f_a = 0.1$ is clearly incompatible with the real data.

Models with anisotropic upper mantle material below an isotropic crust ("mantleAA") do a better job of recreating the observed P_{MIN} data (Figure 4.13). The model parameters are:

$$\text{layer 1: } \rho_1 = 2 \times 10^3\ \Omega\text{m, dd}_1 = 6\ \text{km}$$
$$\text{layer 2: } \rho_m = 10^4\ \Omega\text{m, dd}_2 = 20\ \text{km}$$
$$\text{layer 3: } \rho_3 = 10^4\ \Omega\text{m}$$

Again $f_a = 0.5$ and $f_a = 0.1$ are presented. Anisotropy in the upper mantle is, at face value, more consistent with the 30-km radius circular tow data than is anisotropy in the crust.

4.4.2 Anisotropic inversion

The Marquardt algorithm was used to invert the reduced large circular tow data subset, with the three-layer anisotropic code as the forward operator. The solution that Marquardt converges on, as has been mentioned, is dependent on the starting model – the modeling and inversion results presented in this chapter provided starting models from which competing hypotheses about the physical nature of the anisotropic conductivity were tested.

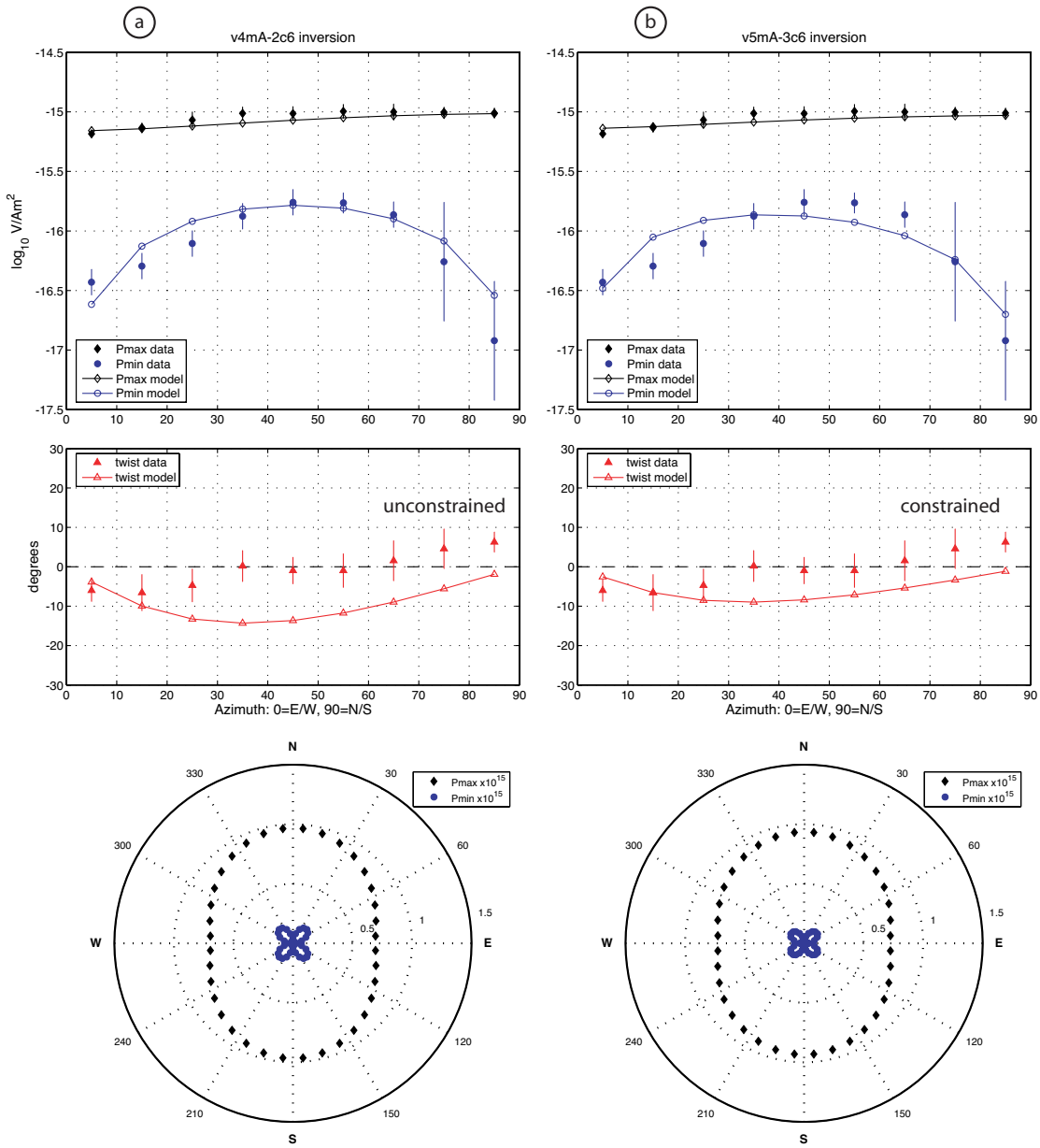

Figure 4.14 Marquardt inversions for conductive vertical-sheet mantle anisotropy (a) constrained by P_{MAN} and P_{MIN} is fit to RMS 0.961, while (b) adding twist as inversion data increases misfit and reduces the anisotropic ratio. Model resistivities and thicknesses are plotted in Figure 4.15. Compare polar plots with Figure 4.1.

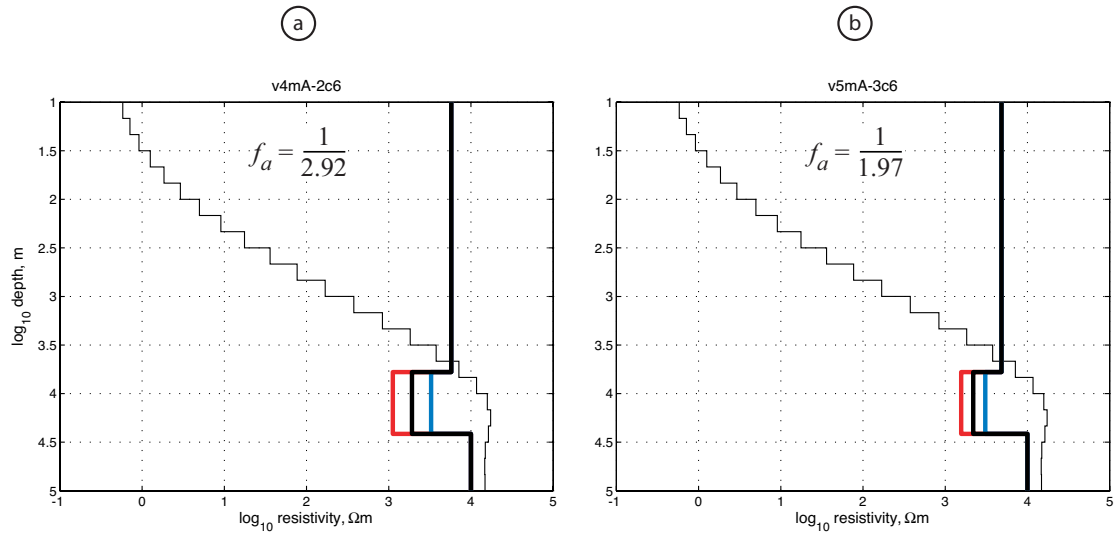

Figure 4.15 Vertical sheet mantle anisotropy models recovered from inversion; data presented in Figure 4.14.

4.4.2.1 Mantle sheets

The principal starting model for these inversions ("mantleA") is shown in Figure 2.14. It is similar to mantleAA10:

$$\text{layer 1: } \rho_1 = 5\times10^3\ \Omega\text{m, dd}_1 = 6\text{ km}$$
$$\text{layer 2: } \rho_m = 3.16\times10^3\ \Omega\text{m, dd}_2 = 20\text{ km}$$
$$\text{layer 3: } \rho_3 = 10^4\ \Omega\text{m}$$

with $f_a = 0.1$ and Tx altitude 100 m. An inversion run from a modified starting model with a more resistive upper mantle layer 2 with $f_a = 0.33$ $\left(\rho_{\|} = 10^4,\quad \rho_{\perp} = 3\times10^4\right)$ resulted in the same minimum misfit models as will be described forthwith.

The variable parameters **p** were: anisotropic layer 2 log resistivities $\log_{10}(\rho_{\|})$ and $\log_{10}(\rho_{\perp})$, along with $\log_{10}(\rho_1)$. The use of log resistivities kept the inversion parameters positive and scaled properly for computation of the Jacobian and application of the ridge regression parameter λ.

Using only P_{MAX} and P_{MIN} as data at first (Figure 4.14.a), the minimum misfit model (Figure 4.15.a) was found to be, after 5 iterations:

$$\begin{aligned} \log_{10}\rho_1 &= 3.761 \pm 0.030 & \rho_1 &= 5763\ \Omega\text{m} \\ \log_{10}\rho_{\|} &= 3.050 \pm 0.057 & \rho_{\|} &= 1121\ \Omega\text{m} \\ \log_{10}\rho_{\perp} &= 3.516 \pm 0.031 & \rho_{\perp} &= 3278\ \Omega\text{m} \end{aligned}$$

with correlation matrix:

$$\begin{matrix} \log_{10}\rho_1 \\ \log_{10}\rho_{\|} \\ \log_{10}\rho_{\perp} \end{matrix} \rightarrow \begin{bmatrix} 1 & & \\ -0.301 & 1 & \\ 0.445 & -0.4399 & 1 \end{bmatrix}$$

and an RMS misfit of 0.961. The correlation between ($\log_{10}$) resistivities is shown to be non-linear. These resistivities are within an order of magnitude of what is expected, but the crust is too resistive as a whole, and the upper mantle too conductive. The linear anisotropic ratio of the mantle is $f_a = 1/2.92$, similar to what was found by single-component inversion in section 4.3.2.

Adding the twist, in degrees, of the polarization ellipse away from transmitter-parallel as an inversion constraint (Figure 4.14.b) yields a similar model (Figure 4.15.b), again after 5 iterations:

$$\begin{aligned} \log_{10}\rho_1 &= 3.685 \pm 0.094 & \rho_1 &= 4839\ \Omega\text{m} \\ \log_{10}\rho_{\|} &= 3.194 \pm 0.060 & \rho_{\|} &= 1562\ \Omega\text{m} \\ \log_{10}\rho_{\perp} &= 3.487 \pm 0.035 & \rho_{\perp} &= 3069\ \Omega\text{m} \end{aligned}$$

with correlation matrix:

$$\begin{bmatrix} 1 & & \\ -0.745 & 1 & \\ 0.123 & 0.399 & 1 \end{bmatrix}$$

The misfit of all the data together was 1.409; the misfit of only P_{MAX} and P_{MIN} was increased slightly to 0.993. The linear anisotropic ratio of the mantle was decreased to $f_a = 1/1.97$, but still in accordance with the single-component inversion result.

Again, the obvious problem with these models is the overly resistive crust and overly conductive mantle relative to the Occam inversions and prior studies of Pacific plate electrical properties. The burden of approximating an exponentially varying crust with a single resistivity appears to be too great, and as a result, the upper mantle is made too conductive as a whole to compensate. The presence of only one source-receiver offset in the data seriously hampers depth resolution, as well.

In an inductive EM sounding, the thickness - conductivity product $T\sigma^{0.5}$ of a layer is, theoretically, the property resolved. An empirical study on the PEGASUS data found $T\sigma^{0.62}$ to be conserved [Constable and Cox, 1996]; a layered-model analysis by the author on several APPLE short-radial tow subsets found $T\sigma^{0.7}$ (this also holds fairly true for the upper layers of the Marquardt inversions of section 4.2.1). For the top 6.8 km of the LQ3 preferred inversion model, $\sum T_i \sigma_i^{0.7} = 189.07 \text{ m} \cdot (\text{S/m})^{0.7}$, yielding an equivalent single-layer resistivity of ~167 Ωm. Inversions were run with the crustal layer properties fixed to $\text{dd}_1 = 6.8$ km, $\rho_1 = 167$ Ωm, but they diverged, with $\rho_\perp$ increasing to non-physical levels (*e.g.* 10^{100}) while $\rho_{||}$ remained in the range 10^3-10^4. Adding $\log_{10}(\text{dd}_2)$ as a variable

parameter did not allow convergence. Nor did allowing ρ_1 to vary once again. This is rather surprising, since it was equivalent in procedure to the inversions that did converge, just with a more conductive crust in the starting model. The parameters oscillated widely for a few iterations before divergence, never fitting the data very well. Twist was not used; the philosophy was to try to simply fit the ellipse axes first.

Another approach taken was to approximate the effect of the missing conductive upper crust as being purely attenuative by scaling the fields by a constant value. This being a frequency-domain sounding, the dominant component of the measured electric field will have propagated along the path of least attenuation – in this case, that path is vertically down through the crust, laterally through the resistive upper mantle, and then vertically up through the crust to the receiver.

To find an appropriate scaling factor, the isotropic code was used to compute the change in field magnitude when the top 6.8 km of the LQ3 preferred inversion model was increased to 5000 (= $10^{3.7}$) Ωm, for source-receiver offsets ranging from 29 and 31 km and CCAzimuths $85° \le \phi \le 95°$. $\log_{10}|E_\phi|$ and $\log_{10}|E_\rho|$ were found to increase by 0.279 and 0.294, respectively, at all of these geometries.

Inversions were run with a modified anisotropic forward code that subtracted these attenuation terms from $\log_{10}|E_\phi|$ and $\log_{10}|E_\rho|$ before they were used to compute the polarization ellipse parameters, but failed to converge. Another attempt with 0.279 applied to both terms also failed to converge.

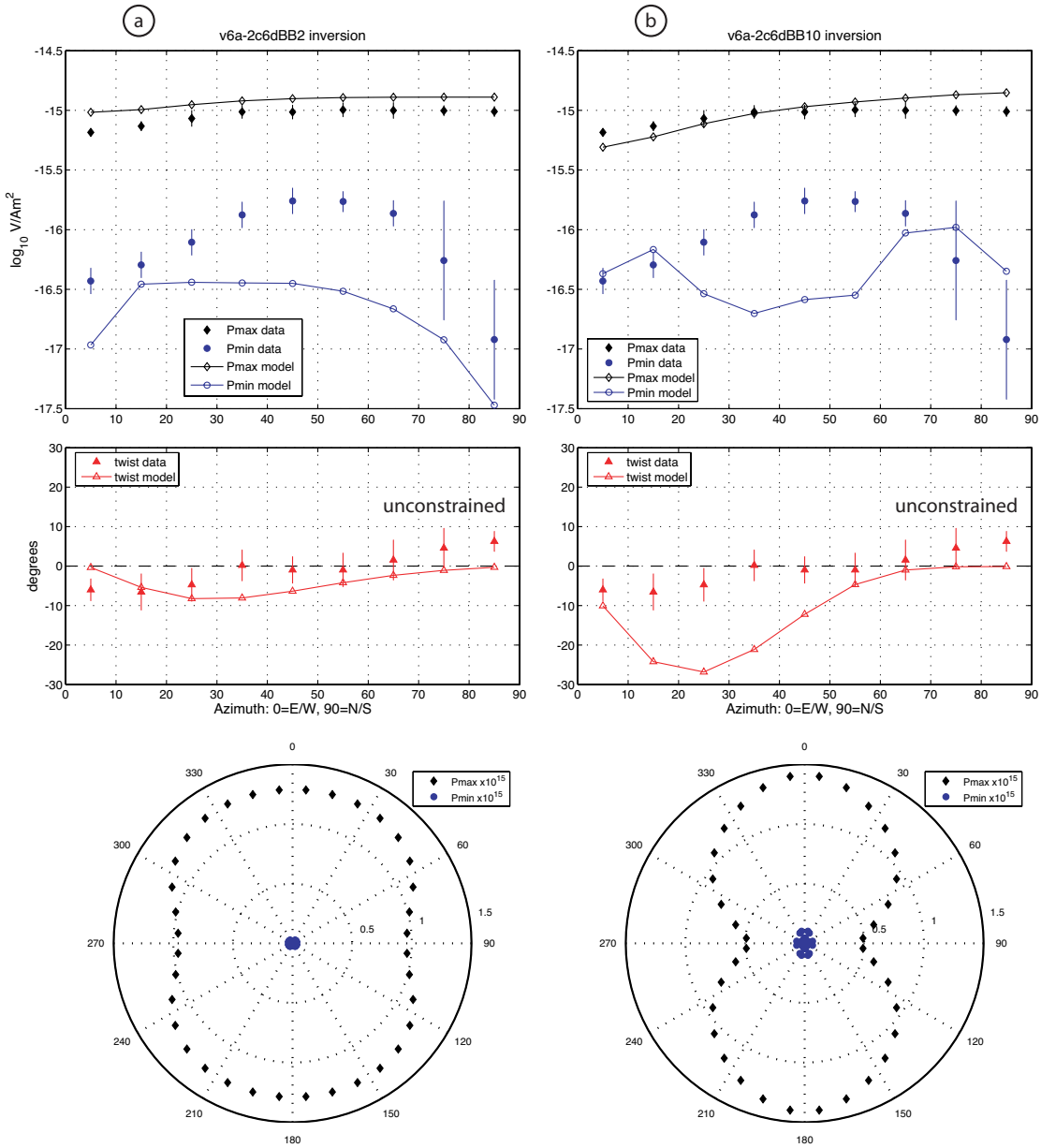

Figure 4.16 Marquardt inversions for conductive vertical-sheet crustal anisotropy were unable to fit the observed P_{MIN} data.

4.4.2.2 Mantle rods

For completeness, a horizontal conductive rods model was used as a starting point for inversion of P_{MAX} and P_{MIN}. This model was the same as mantleA, but with $\rho_\perp$ and $\rho_\parallel$ swapped (yielding $f_a = 10$). The conductive horizontal component was still aligned north/south. After 10 iterations, the inversion converged on an ill-fitting (RMS 1.8) conductive sheets model. This result adds further support to the north-south conductive vertical sheets hypothesis.

4.4.2.3 Crustal sheets

The final hypothesis to be tested with inversion is the possibility that a crustal source of anisotropy (*i.e.* the sheeted dikes) could generate the pattern observed in the large circular tow data. Starting from the dikesBB models (Figure 4.11.b, Figure 4.12), Marquardt was used to try to fit the P_{MAX} and P_{MIN} data. Initially, the top layer (extrusive basalt) conductivity was fixed at 10 Ωm – perhaps a bit too resistive, but not by much – and the anisotropic layer resistivities $\rho_\parallel$ and $\rho_\perp$ were free to vary.

These inversions (dikesBB2, dikesBB10) both converged (4 iterations, 5 iterations) and with reasonable $\rho_\parallel$ and $\rho_\perp$ (in the range 10^2-10^3 Ωm; $f_a = 0.3$, $f_a = 0.1$), but the data misfit is unacceptably large (RMS 4.4, RMS 4.0). (Subsequent inversion from dikesBB2 with ρ_1 a free variable converged on essentially the same model.) The magnitude and pattern of P_{MIN} in particular (Figure 4.16) appears to preclude the possibility of the sheeted dikes being the sole location of anisotropic conductivity in the lithosphere; some degree of mantle anisotropy is required to match the real data.

4.5 References

Constable, S., and C. S. Cox (1996), Marine controlled-source electromagnetic sounding 2. The PEGASUS experiment, Journal of Geophysical Research, 101, 5519-5530.

Everett, M. E., and S. Constable (1999), Electric dipole fields over an anisotropic seafloor: theory and application to the structure of 40 Ma Pacific Ocean lithosphere, Geophysical Journal International, 136, 41-56.

Everett, M. E., S. C. Constable, and J. Behrens (in preparation), The detection of an anisotropic layer in oceanic lithosphere by the seafloor controlled-source electromagnetic method, Geophysical Journal International.

Chapter 5

Discussion and Conclusions

5.1 Discussion

Geophysical modeling and inversion of the CSEM data leads to geologic interpretation. In brief, the data are most compatible with anisotropic models representing north/south (paleo-ridge parallel) trending vertical sheets of increased conductivity in the lithospheric upper mantle. Hydration of mantle peridotites along ridge-parallel normal faults is therefore suspected. In this chapter, inversion results will be interpreted, an estimate of the degree of serpentinization will be made, hydrothermal circulation discussed, and implications of mantle serpentinization explored.

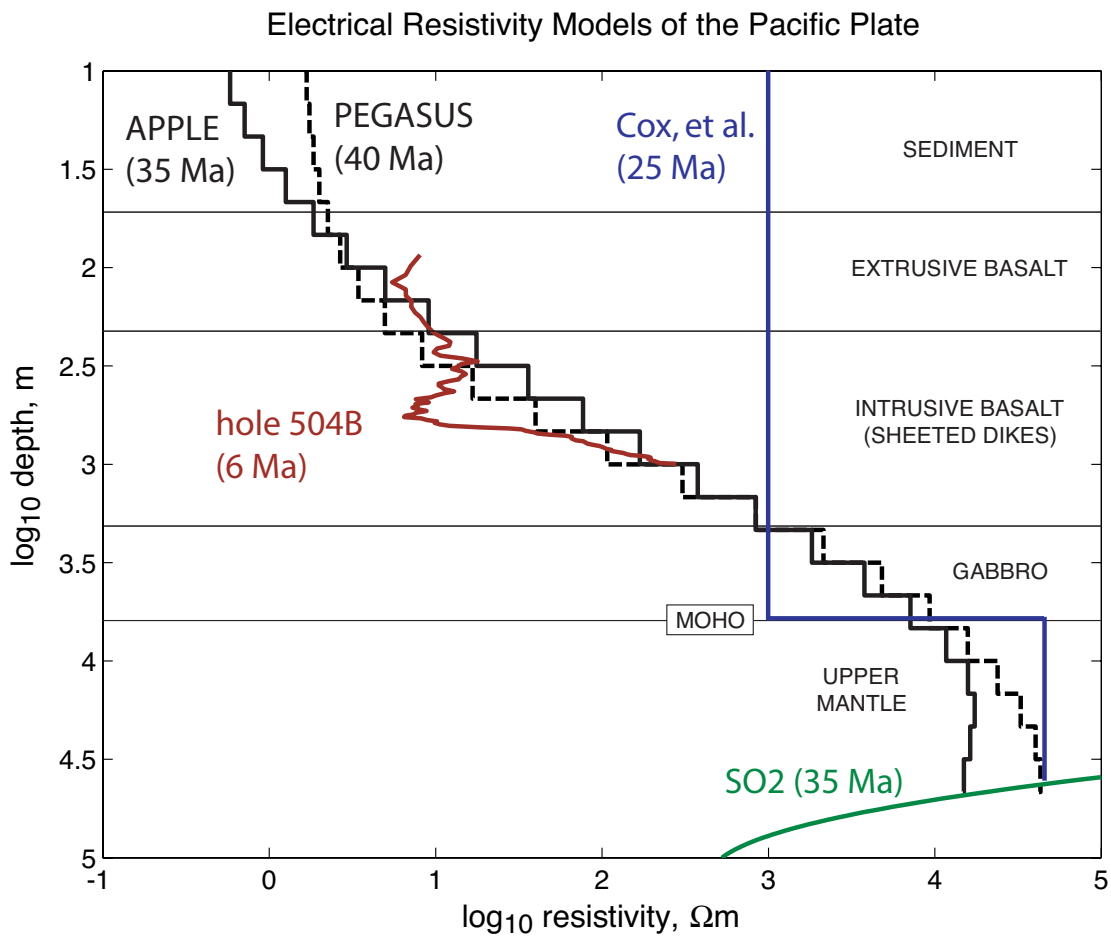

Figure 5.1 Preferred isotropic resistivity model at APPLE (section 4.3.1) is generally consistent with what was observed at the Cox *et al.* site, PEGASUS, and in ODP Hole 504B (section 1.3.2). SO2 is a model of anhydrous olivine conductivity at 35 Ma (section 1.3.2).

5.1.1 Isotropic model

Inversion of P_{MAX} generated an isotropic resistivity model consistent with results from earlier CSEM surveys over Pacific lithosphere (Figure 5.1, section 1.3.2). Shallow conductivities in the APPLE model are influenced by the seawater conductivity inversion prejudice applied to the top sub-seafloor layer. The exponential decrease in conductivity with

increasing depth in the crust is consistent with an exponential decrease in fluid permeability deduced from heat flow measurements [Fisher, 1998].

A deep increase in conductivity (> 30 km depth), while slight, appears to be a robust feature of the APPLE inversions (Figure 4.5). This sort of model oscillation is not all that uncommon and is possibly a result of smoothing the conductivity contrasts across what may in fact be abrupt transitions in the real earth. Removing the deep increase in conductivity does worsen the overall RMS misfit, however, affecting model data at ranges ≥ 30 km. This deep increase occurs at a shallower depth than the SO2 model predicts; if it is real, it may indicate an anomalously steep geotherm, leading to a shallower transition to the aesthenosphere. A regional slow shear-wave anomaly has been observed in the upper mantle beneath the APPLE survey site; one interpretation is the presence of partial melt [G. Laske, personal communication], which would increase bulk conductivity. Laboratory measurements of lherzolite at high temperatures [Duba and Constable, 1993] indicate a slightly higher conductivity than the SO2 model by about a factor of 2, which would also support the legitimacy of this deep conductivity increase.

5.1.2 Anisotropic models

Some evidence exists for anisotropic electrical conductivity in the sheeted dike layer – namely the short-rage P_{MAX} inversions on the west side of the large circle (section 4.2) and the small split in single-component inversion of the LQ3 data set (section 4.3.2). Inversions of short-range data sets all the way around the circle, however, show that non-anisotropic heterogeneity of the same magnitude is present in the top 2-3 km of the crust. There was only one short-range tow in the fossil-spreading-parallel east/west direction, unfortunately, adding uncertainty to this mode of analysis.

Anisotropic forward modeling and inversion further indicates that an anisotropic sheeted dike layer alone is insufficient to explain the variation in the large circular tow data (section 4.4). Some degree of anisotropy could very well exist in the sheeted dikes, contributing to the anisotropic pattern in the large circular tow data, but physically reasonable models are fundamentally unable to reproduce it.

It is unfortunate that the navigational parameters during the semicircular tow were so unsteady, and that the higher harmonic data were rendered too uncertain due to transmitter clock instability; these data could have played a key role in separating the effects of any anisotropic conductivity in the upper crust. The significant twist seen in ellipse orientation during the semicircular tow (Figure 4.9) remains uninterpreted.

Lithostatic pressure seals off most of the permeable space between pores below the extrusive basalts, so any anisotropy that exists in 35 Ma sheeted dikes would most likely be the result of an increased concentration of conductive, isolated pore spaces at the dike boundaries.

The gabbros appear to be isotropic in the LQ3 single component inversion (Figure 4.6). As such, anisotropic gabbro models were not part of the modeling study. Even though the gabbros are penetrated by hydrothermal conduits (sections 1.4, 5.1.3), they are less porous than the overlying basalt, and contain less olivine and iron than mantle peridotites.

Inversion of the large circular tow data with an anisotropic upper mantle was able to fit the data to RMS 1.0, with anisotropic ratio of 2-3, similar to what was found from single component inversion of LQ3. The crust was too resistive, however, leading to an overly conductive upper mantle layer. A few methods were attempted to match the isotropic crustal model resistivity, but were unsuccessful. It is quite possible that running inversions from a wider range of starting models will eventually find a more physically reasonable result.

Evidence is strong from both single component isotropic inversion and ellipse parameter anisotropic inversion that mantle anisotropy corresponding to paleo-ridge parallel vertical conductive sheets is required by the data, starting at the Moho and continuing for several kilometers depth. Single component inversion suggests the anisotropic layer extends to 20-30 km below the seafloor. Allowing anisotropic layer thickness to vary in Marquardt inversion (section 4.4.2.1) reduced it to ~ 10 km, but a corresponding unbounded increase in $\rho_{\perp}$ caused divergence. Several mantle sheets inversions, in fact, diverged due to runaway increases in $\rho_{\perp}$ while $\rho_{\parallel}$ remained around 10^4 Ωm, including many of the attempts to apply conductive crustal layers. This suggests that the conductive N/S direction is well constrained, while the resistive E/W direction is not, and that upper mantle anisotropic ratios may be significantly larger than 2-3. Single-component LQ3 inversion of the E/W data was prejudiced to the P_{MAX} model and constrained to be smooth, so E/W resistivity in Figure 4.6 should be considered the *minimum* mantle resistivity in the fossil spreading direction.

Comparison of the N/S single-component data inversion with the P_{MAX} model in Figure 4.6 indicates that, over anisotropic structure, P_{MAX} mixed-mode inversion will return the most conductive component of the anisotropic conductivity tensor.

The Hashin-Shtrikman conductivity bounds (equation 1.3.2) for a mixture of 10 Ωm serpentinite in peridotite of $\rho \geq 10^6$ Ωm (section 1.3.3) indicates that a minimum of 0.1% serpentinization of the upper mantle by volume is required to reduce bulk resistivity to 10^4 Ωm (Figure 5.2), the inferred resistivity in the N/S and vertical directions. A bulk serpentinite volume proportion near the HS^+ bound, which represents complete interconnection of the conductive phase, is plausible if, as is suspected, serpentinization occurs along continuous ridge-parallel vertical “sheets”.

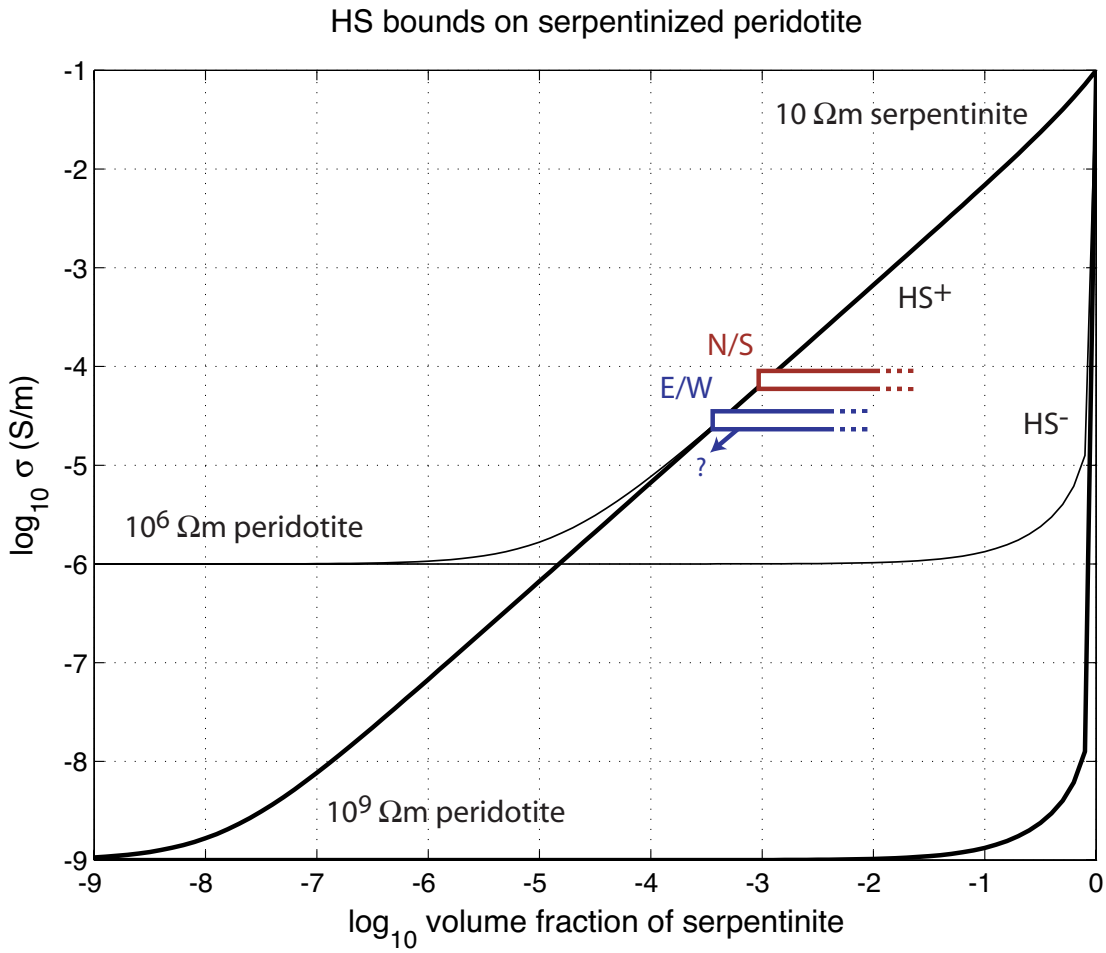

Figure 5.2 Mixing law relationship between serpentinite volume fraction and bulk conductivity of the upper mantle. Large-scale serpentinite interconnection is suspected along N/S vertical sheets, placing the volume fraction near the HS+ bound. True resistivity of the more resistive unaltered peridotite matters little. The plotted E/W resistivity value is a minimum estimate.

5.1.3 Hydrothermal circulation

Hydrothermal circulation is a convective process that serves to cool the lithosphere faster than it would through radiative cooling alone [Haymon, 1989]. Large-scale, predominantly ridge-parallel vertical fractures open in response to ridge-normal tension, and provide conduits

for seawater to be drawn into the crust (section 1.4, and below). Host rocks are altered by interaction with the seawater (sections 1.3.2, 1.3.3, 5.1.4).

The Oman ophiolite, interpreted to have been a fast-spreading ridge segment of full rate ~ 100 mm/yr [Nicolas*, et al.*, 2003], has been mapped and studied in extensive detail. Hydrothermal alteration minerals exist in veins that penetrate through and are aligned with the sheeted dike complex at the ridge axis [Nehlig*, et al.*, 1994]. An extensive system of microcracks (in the mm to sub-mm thickness range), also forming vertical ridge-parallel sheets, provided pathways for seawater to be carried in episodic bursts all the way through the gabbros to the magma chamber, resulting in alteration at very high temperatures (VHT, up to 1000 °C) [Nicolas*, et al.*, 2003]. Serpentinization of olivine is not stable and thus does not occur until temperatures have cooled below ~ 500 °C [O'Hanley, 1996]. Lower-temperature greenschist alteration facies have been mapped throughout the crustal section of the ophiolite – confirming that low temperature (LT; T < 500 °C) veins penetrate the entire crust and are dominantly aligned parallel to the sheeted dike complex [Bosch*, et al.*, 2004]. The ophiolite section was able to cool below 500 °C before obduction, indicating that these LT veins were emplaced *in situ* [Nicolas*, et al.*, 2003].

Studies of sub-Moho peridotites collected from an ODP borehole at Hess Deep [Dilek*, et al.*, 1998; Frueh-Green*, et al.*, 2001] found extensive LT serpentinization (with associated magnetite) of upper mantle peridotites along macroscopic veins, the emplacement of which was enabled by extensional fracturing, rather than faulting. Serpentine alteration of peridotites exceeds 60% in most samples, but rifting of Hess Deep due to westward propagation of the Galapagos Ridge may have allowed the massive penetration of seawater into the peridotites [Fryer, 2002].

Seafloor heat flow measurements away from the intermediate-rate Galapagos Ridge are lower than predicted for conductive cooling, indicating that hydrothermal circulation may continue for as long as 60 to 80 My [Haymon, 1989]. It is possible that the normal faults observed at the seafloor propagate through the Moho into the upper mantle and continue to grow, providing conduits for LT seawater infiltration long after VHT microcracks become sealed by alteration minerals. Analysis of bathymetric and side-scan sonar data at the EPR at 9°N suggests a rapid period of normal fault growth during the first 1 Ma, leveling off at 100 m vertical relief until at least 3 Ma [Crowder and Macdonald, 2000]. Bathymetric relief at APPLE is consistent with ~200 m vertical fault scraps separating blocks on the order 10 km width (figure 1.2), suggesting a slow but positive rate of fault growth away from the spreading center. These growing faults provide paleo-ridge parallel vertical pathways along which water may penetrate the seafloor.

5.1.4 Mantle serpentinization

Hess [1962] proposed that the Moho was a serpentinization front, envisioning the lower crust as hydrated peridotites, with unaltered mantle below. By using seismic studies of the oceanic crust to determine Poisson's ratio values Christensen [1972] determined that the lower crust was composed of gabbros, rather than serpentinite. Research since has supported this conclusion, although, especially in crust formed at the slow-spreading, magma-starved Mid-Atlantic Ridge, significant amounts of serpentinization has been observed in peridotites exposed by amagmatic extensional tectonic processes [Bach*, et al.*, 2004; O'Reilly*, et al.*, 1996; Reston*, et al.*, 2001].

The physical implications of widespread serpentinization in the uppermost mantle beneath the Pacific plate are broad. Volumetric expansion between 25% and 50% takes place

upon serpentinization [Fryer, 2002]. Oceanic serpentinites typically contain 10 to 13 wt% water, consuming an average of 300 kg of water per m^3 [Frueh-Green*, et al.*, 2001]. Serpentinization is exothermic, and in a closed system is capable of raising the rock temperature by ~ 260 °C [Frueh-Green*, et al.*, 2001], perhaps prolonging LT hydrothermal circulation in an example of positive feedback. Serpentinite content as low as 10% greatly weakens the shear strength of peridotite [Escartin*, et al.*, 2001]; this is a potential source of positive feedback between fault growth and serpentinization. Serpentinite dehydration in subducting oceanic plates may generate seismicity [Peacock, 2001] and contributes to partial melting in the overlying mantle wedge [Seno*, et al.*, 2001]. Serpentinization of the upper mantle delays and displaces the acquisition of magnetic anomalies within relative to the crust, skewing anomaly data [Dyment*, et al.*, 1997].

5.2 Conclusions

CSEM data collected at the APPLE survey site, over 35 Ma ultra-fast spreading EPR-generated Northeast Pacific lithosphere, are in agreement with an electrical conductivity model with a conductive upper crust overlying a more resistive upper mantle. Electrical resistivity increases by nearly five orders of magnitude from seawater to upper mantle. This result is consistent with prior induction soundings, borehole resistivities, and laboratory measurements of mafic and ultramafic rocks.

Modeling and inversion of various subsets of the data indicate anisotropic conductivity in the lithosphere, consistent with vertical sheets of increased conductivity, aligned normal to the fossil spreading direction, beginning at the Moho and continuing at least 10 km into the lithospheric upper mantle. The ratio of conductivities is at least 2-3, with perhaps even greater resistivities normal to the conductive sheets.

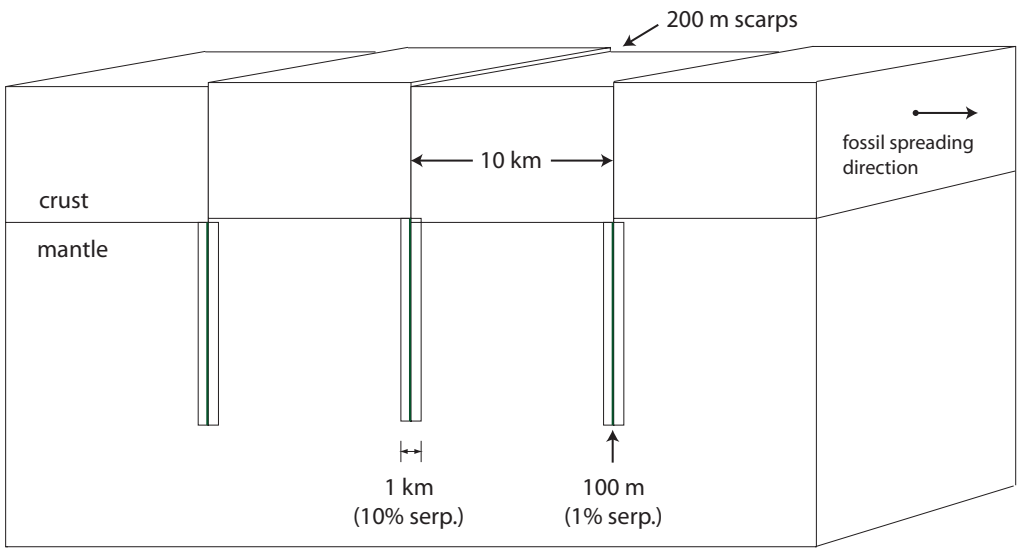

Figure 5.3 Serpentinite in the upper mantle, well-connected along fault zones normal to the fossil spreading direction, is consistent with the preferred anisotropic electrical conductivity model. Width of the serpentinized zones around the faults is related to volumetric serpentinite content (Figure 5.2) and is drawn to scale.

Evidence from ophiolite, seismic, and borehole studies indicates that seawater can penetrate through the entire crust and into the upper mantle, beginning at the ridge axis and continuing perhaps indefinitely. LT hydration of olivine is commonly observed and produces locally high concentrations of electrically conductive magnetite. It is thus proposed that preferential serpentinization of upper mantle peridotites along vertical, paleo-ridge parallel hydrothermal conduits is at least partly responsible for the observed anisotropic bulk conductivity of the lithosphere. Bulk serpentinization of total mantle peridotite must be, at the very least, 0.1% by volume to generate the inferred conductivity – for example, 10 m wide zones of complete, continuous serpentinization along normal faults spaced 10 km apart – and is likely to be somewhat greater (Figure 5.3).

Anisotropic analysis of the PEGASUS CSEM data [Everett and Constable, 1999] found those data to be consistent with an east/west directed horizontal conductive rods model, in contrast to this result from APPLE. The APPLE result is unambiguous, however. PEGASUS source-receiver geometries were rather limited relative to APPLE, and anisotropic interpretation was based on one or two data points near the noise floor, making non-uniqueness especially problematic. The authors of that study were aware of the tenuous nature of their conclusions, and proposed APPLE as a verification experiment. If the difference is indeed real, however, it may be related to fundamental differences in plate formation and/or evolution. The seafloor at APPLE is nearly 1 km shallower (but only 5 Ma younger) with a more hummocky texture – perhaps a result of volumetric increase due to upper mantle serpentinization.

5.3 Future directions

The anisotropic modeling code, while useful in discriminating between the effects of crustal and mantle anisotropy, has notable limitations. Addition of more isotropic layers above the anisotropic layer and/or inclusion of a second anisotropic layer would help refine these results and conclusions. Perhaps these data can be re-analyzed at some point using one of the several finite-element CSEM modeling codes presently under development.

Inversion of long radial tow single-component data may add greater sensitivity to the thickness of the anisotropic upper mantle layer, and help stabilize the inversion. As it is, however, inversions of only 9 source-receiver geometries (the circular tow bins) for 2 or 3 model parameters takes a full 24 hours on a Mac with dual-G5 processors. The model study presented in chapter 4 has narrowed the family of models of interest, however, so the effort of running more time-consuming inversions is now more justifiable.

An assumption made in modeling the diffusion of EM energy through the seafloor was that magnetic permeability is small enough to be treated as the free-space value everywhere. That is often true, but if magnetite is the conductive phase responsible for these observations, perhaps the effect of its significant permeability value should be investigated. Horizontal magnetic field polarization ellipse parameters measured at the center of a circular tow may follow an anisotropic pattern if the permeability effect is great enough; these data would provide additional constraints for the earth model.

Any future CSEM experiments of this sort should be run at multiple frequencies, some lower than the 4 Hz used here. Doing so will increase maximum depth of sensitivity and add depth resolution to the data from a single circular tow. Multiple complete concentric circular tows of different radii would help differentiate between crustal and mantle anisotropy – these were part of the original cruise plan for APPLE, but stormy weather and a late arrival of the R/V Thompson at the onset forced economization.

It is possible that phase data will be non-paradoxical. That is, for the circular tow, phase may be a function of the propagation path, as opposed to the plane of phasor oscillation. Modeling has not been done to investigate anisotropic patterns in the phase data, since absolute phase data was not available, nor was relative phase data between instruments in a straight line from the transmitter. For future experiments of this sort, it is worth investigating.

This experiment should be repeated in different locations to determine how typical these results are. Comparing results from seafloor locations both with and without skewed magnetic anomalies will test the theory that mantle serpentinization affects magnetic anomaly data. Comparing results along a track from spreading center to subduction zone will provide insight about fault growth in the lithosphere and help constrain the volatile content of subducting slabs.

5.4 References

Bach, W., C. Garrido, H. Paulick, J. Harvey, and M. Rosner (2004), Seawater-peridotite interactions: First insights from ODP leg 209, MAR 15°N, Geochemistry, Geophysics, Geosystems, 5.

Bosch, D., M. Jamais, F. Boudier, A. Nicolas, J.-M. Dautria, and P. Agrinier (2004), Deep and high-temperature hydrothermal circulation in the Oman ophiolite - petrological and isotopic evidence, Journal of Petrology, 45, 1181-1208.

Christensen, N. (1972), The abundance of serpentinites in the oceanic crust, Journal of Geology, 80, 709-719.

Crowder, L. K., and K. C. Macdonald (2000), New constraints on the width of the zone of active faulting on the East Pacific Rise 8°30' N - 10°00' N from Sea Beam Bathymetry and SeaMARC II Side-scan Sonar, Marine Geophysical Researches, 21, 513-527.

Dilek, Y., E. Moores, and H. Furnes (1998), Structure of modern oceanic crust and ophiolites and implications for faulting and magmatism at oceanic spreading centers, in Faulting and Magmatism at Mid-Ocean Ridges, edited by W. R. Buck, et al., American Geophysical Union, Washington, D.C.

Duba, A., and S. Constable (1993), The electrical conductivity of lherzolite, Journal of Geophysical Research, 98, 11885-11899.

Dyment, J., J. Arkani-Hamed, and A. Ghods (1997), Contribution of serpentinized ultramafics to marine magnetic anomalies at slow and intermediate spreading centres: insights from the shape of the anomalies, Geophysical Journal International, 129, 691-701.

Escartin, J., G. Hirth, and B. Evans (2001), Strength of slightly serpentinized peridotites: Implications for the tectonics of the oceanic lithosphere, Geology, 29, 1023-1026.

Everett, M. E., and S. Constable (1999), Electric dipole fields over an anisotropic seafloor: theory and application to the structure of 40 Ma Pacific Ocean lithosphere, Geophysical Journal International, 136, 41-56.

Fisher, A. T. (1998), Permeability within basaltic oceanic crust, Reviews of Geophysics, 36, 143-182.

Frueh-Green, G., J. Connolly, A. Plas, D. Kelly, and B. Grobety (2001), Serpentinization of oceanic peridotites: implications for geochemical cycles and biological activity, The Subseafloor Biosphere at Mid-Ocean Ridges, Special Publication, AGU.

Fryer, P. (2002), Recent studies of serpentinite occurrences in the oceans: mantle-ocean interactions in the plate tectonic cycle, Chemie der Erde/Geochemistry, 62, 257-302.

Haymon, R. M. (1989), Hydrothermal processes and products on the Galapagos Rift and East Pacific Rise, in The Eastern Pacific Ocean and Hawaii, edited by E. L. Winterer, et al., Geological Society of North America, Boulder, Colorado.

Hess, H. H. (1962), History of Ocean Basins, in Petrological Studies: A Volume in Honor of A.F. Buddington, edited by A. E. J. Engel, et al., pp. 599-620.

Nehlig, P., T. Juteau, V. Bendel, and J. Cotten (1994), The root zones of oceanic hydrothermal systems: constraints from the Samail ophiolite (Oman), Journal of Geophysical Research, 99, 4703-4713.

Nicolas, A., D. Mainprice, and F. Boudier (2003), High-temperature seawater circulation throughout crust of oceanic ridges: A model derived from the Oman ophiolites, Journal of Geophysical Research, 108, 2371.

O'Hanley, D. S. (1996), Serpentinites: records of tectonic and petrological history, 277 pp., Oxford University Press, Oxford.

O'Reilly, B., F. Hauser, A. W. B. Jacob, and P. Shannon (1996), The lithosphere below the Rockall Trough: wide-angle seismic evidence for extensive serpentinisation, Tectonophysics, 255, 1-23.

Peacock, S. M. (2001), Are the lower planes of double seismic zones cause by serpentine dehydration in subducting oceanic mantle? Geology, 29, 299-302.

Reston, T. J., J. Pennell, A. Stubenrauch, I. Walker, and M. Perez-Gussinye (2001), Detachment faulting, mantle serpentinization, and serpentine-mud volcanism beneath the Porcupine Basin, southwest of Ireland, Geology, 29, 587-590.

Seno, T., D. Zhao, Y. Kobayashi, and M. Nakamura (2001), Dehydration of serpentinized slab mantle: Seismic evidence from southwest Japan, Earth Planets Space, 53, 861-871.